Design, Analysis, and Development of a Tripod Film Cooling Hole Design for Reduced Coolant Usage

Christopher N. LeBlanc

Dissertation submitted to the Faculty of the
Virginia Polytechnic Institute and State University
in partial fulfillment of the requirements for the degree of

Doctor of Philosophy
in
Mechanical Engineering

Srinath V. Ekkad, Chair
Wing F. Ng
Thomas E. Diller
Danesh K. Tafti
Christopher J. Roy

December 4, 2012
Blacksburg, Virginia

Keywords: Heat Transfer, Gas Turbine Cooling, Film Cooling

Design, Analysis, and Development of a Tripod Film Cooling Hole Design for Reduced Coolant Usage

Christopher N. LeBlanc

ABSTRACT

This research has a small portion focused on interior serpentine channels, with the primary focus on improving the effectiveness of the film cooling technique through the use of a new approach to film cooling. This new approach uses a set of three holes sharing the same inlet and diverging from the central hole to form a three-legged, or tripod, design. The tripod design is examined in depth, in terms of geometric variations, through the use of flat plate and cascade rigs, with both transient and steady-state experiments. The flat plate tests provide a simplified setting in which to test the design in comparison to other geometries, and establish a baseline performance in a simple flow field that does not have the complications of surface curvature or mainstream pressure gradients. Cascade tests allow for testing of the design in a more realistic setting with curved surfaces and mainstream pressure gradients, providing important information about the performance of the design on suction and pressure surfaces of airfoils. Additionally, the cascade tests allow for an investigation into the aerodynamic penalties associated with the injection hole designs at various flow rates. Through this procedure the current state of film cooling technology may be improved, with more effective surface coverage achieved with reduced coolant usage, and with reduced performance penalties for the engine as a whole. This research has developed a new film hole design that is manufacturable and durable, and provides a detailed analysis of its performance under a variety of flow conditions. This cooling hole design provides 40% higher cooling effectiveness while using 50% less coolant mass flow. The interior serpentine channel research provides comparisons between correlations and experiments for internal passages with realistic cross sections.

This work received support from the United States Department of Energy (DOE) National Energy Technology Laboratory (NETL) and Rolls-Royce Corporation, Indianapolis.

Acknowledgments

This work was made possible through the support of a great many people over the years, most prominently my advisor Dr. Srinath Ekkad. Without his guidance and support over the past four years I would not have been able to accomplish half of what I have. Thanks are also extended to Mary Anne Alvin of the DOE-NETL for her support of my film cooling research, including oversight, advice and funding, as well as Tony Lambert and Dr. Veera Rajendran of Rolls-Royce for their support of my internal cooling channel research. I would also like to extend thanks to my undergraduate professors, primarily Dr. Sven Esche, Dr. Siva Thangam and Dr. Marehalli Prasad. Without their guidance and instruction during my undergraduate years, I would not be the engineer I am today. I would also like to extend my thanks to the current and former members of the Heat Energy and Fluids Transport Lab (HEFT) for their assistance and support at various times throughout my graduate education: Dr. Pritish Parida, Dr. Santosh Abraham, Dr. Kapil Panchal, Dr. Song Xue, Dr. Justin LaMont, Dr. Colin Reagle, Drew Newman, Jacob Delimont, Sridharan Ramesh, Arnab Roy, Jaideep Pandit, Dorian Blot, Megan Dove and Guarov Agarwal.

I would also like to acknowledge the contributions of my family, without whom I would not be here at all. My father, Leonard LeBlanc, who is still missed; my mother Carol LeBlanc, who has been unwavering in her support; my older sister Jean Gray, who was the first of our family to get an advanced degree; and my younger sister Rebecca LeBlanc, who I don't get to see often enough.

Contents

List of Figures

List of Tables

1. Introduction

This dissertation primarily focuses on the development of a new film cooling injection hole design that enhances the effectiveness of the cooling air, while also reducing the amount of coolant required. Film cooling is generally used in the early stages of the turbine section of a gas turbine engine, where the mainstream gas is at its peak temperature. In addition to film cooling, this dissertation also includes some information about internal coolant passages as a secondary focus. Internal cooling passages are used extensively in the turbine section of a gas turbine engine to help control the heat load on blades and vanes.

A significant drawback to the use of film cooling is that the air used for injection is drawn from the compressor section of the engine, resulting in a performance penalty. There is also an aerodynamic penalty associated with coolant injection, as well as the reduction of the temperature of the working fluid without any associated work generated. These considerations suggest that the minimum amount of coolant possible should be used in order to minimize performance penalties.

There are several key parameters involved in film cooling. The first parameter is the blowing ratio (BR) defined as

$$BR = \frac{(\rho V)_{sg}}{(\rho V)_{\infty}} \tag{1.1}$$

BR is a parameter that represents the ratio of the mass flux of the injected coolant to the mass flux of the mainstream air. The second parameter is the density ratio (DR) defined as

$$DR = \frac{\rho_{sg}}{\rho_{\infty}} = \frac{(RT)_{sg}}{(RT)_{\infty}} \tag{1.2}$$

In a typical gas turbine the DR is in excess of 1.5. The third parameter is the mass flow

rate, defined as

$$\dot{m} = \sum_{i=1}^{n} BR(\rho V)_{\infty} a_i \tag{1.3}$$

In terms of measuring the performance of the film cooling holes, the effectiveness (η) is used

$$\eta = \frac{T_{steady} - T_{\infty}}{T_{sg} - T_{\infty}} \tag{1.4}$$

The parameter η is a non-dimensional temperature that represents how well the coolant film is protecting the surface from the mainstream temperature, with a maximum value of 1 and a minimum value of 0.

The most basic implementation of film cooling uses cylindrical holes aligned with the flow direction to inject a layer of cooler fluid that protects the surface from exposure to the hot mainstream flow. A typical cylindrical hole will have an injection angle between 20° and 45°, with a common angle being 30°. Lower angles of injection improve performance by minimizing the jet momentum perpendicular to the surface, however there are physical limits to how small the injection angle may be due to the blade geometry. Cylindrical injection holes are most effective at BRs less than 1; the fluid jet has a propensity to detach from the surface at higher BRs due to high momentum in the direction perpendicular to the surface.

A more advanced implementation of film cooling uses compound angle holes. A compound angle hole is simply a cylindrical hole that injects at an angle that is not directly aligned with the mainstream flow. This technique allows for better spanwise coverage and is often used on highly concave surfaces, as it allows for an appropriate fluid injection angle when otherwise the geometry would dictate a very large injection angle.

The current state of the art implementation of film cooling uses shaped holes, which are cylindrical holes with the exit flared to a larger size. This spreads the flow out more evenly and reduces the jet momentum, providing more even film coverage and avoiding the issue of

jet detachment seen in previous designs. A typical flare angle is 10° to the sides and forward edge of the hole exit. This type of hole allows for the usage of more coolant to increase the effectiveness of the film.

The design investigated in this research is a combination of the previously discussed designs. The basic concept is to increase the spacing of the holes, and then add two compound angle holes branching from the main hole as close to the plenum as possible. There are many potential variations of the design, with different breakout angles between the main and side holes, different spacing between the center hole of one group and the center hole of the next, and the inclusion of shaping at the hole exits.

The research in this section of the dissertation is experimental in nature, utilizing both a flat plate test rig and a vane cascade test rig. Two different experiment types are conducted; a steady-state experiment that allows for the calculation of film cooling effectiveness (η) and a transient experiment that allows for the calculation of heat transfer coefficient (h/h_0) and heat flux ratio ($\frac{q''}{q''_0}$).

The goal of this section of the dissertation is to develop a new hole design that is manufacturable, increases the film cooling effectiveness, reduces the heat flux ratio and reduces the coolant used to accomplish these tasks.

The secondary focus of this dissertation is the experimental investigation of internal cooling channels in a realistic blade geometry. This includes a leading edge channel with showerhead ejection holes and a three pass serpentine channel with trailing edge ejection. The passages are tested with smooth walls and with varying configurations of rib turbulators. These results are compared with traditional correlations to determine how to modify the modeling software to more accurately represent real world conditions.

The first chapter of this dissertation is the introduction, which provides basic information

about the research and its goals, as well as several key equations used throughout. The second chapter is the literature survey, which provides an overview of historical attempts at improving film cooling. The third chapter provides descriptions of the experimental setups utilized to gather data, while the fourth chapter discusses the data reduction techniques for converting the gathered data into useful parameters. Chapters 5 through 8 discuss the experimental results relating to the tripod hole design, while chapter 9 discusses the results of the internal cooling research. Chapter 10 provides the overall conclusions of the research.

2. Literature Survey

Film cooling is a simple and effective means of providing protection over a surface exposed to high temperature gas streams. In gas turbine applications, film cooling technology has enabled extremely high turbine firing temperatures that have increased engine specific power output. In this technique, relatively cold fluid is drawn from the compressor and ejected on the vulnerable surface through discrete holes and slots. Because this fluid is not producing work in the turbine, excessive use of this fluid results in a penalty on the overall engine performance. Hence, efforts are made to keep coolant usage as low as possible while ensuring sufficient surface protection. A significant amount of work has been done to understand the role of cooling hole geometry (shape, size, spacing, etc) and flow (blowing ratio, density ratio, etc) on film cooling performance in an attempt to establish a safe balance between these two contrasting but vital demands.

Many researchers have studied simple cylindrical hole (CY) film cooling on a flat plate dating back to the 70s. Round holes are undoubtedly the simplest way of cooling a gas turbine component such as an airfoil where slots are not practical. A common consensus coming out of these studies is that of a diminishing return in CY hole performance with BR beyond the 0.5-1.0 range, due to flow separation and mainstream entrainment of the hot gas. The bulk of these film-cooling studies utilized secondary gas-to-mainstream DR close to 1.0. This is far from the DR witnessed in real turbines, where, by virtue of the temperature difference between the secondary gas and the hot mainstream, this number typically exceeds 1.5. Goldstein [1] and Pederson et al. [2] demonstrated with the help of 35° inclined holes on a flat plate that peak effectiveness values move towards higher BR with increasing DR. Figure 2.1 shows the geometries examined in the Goldstein [1] study. Using a similar cooling hole geometry, Sinha et al. [3] came to the conclusion that effectiveness scales well with the

mass flux ratio at low BR while the momentum flux ratio is a better scaling parameter at high BR. Ligrani et al. [4] and Schmidt et al. [5] showed that compound-angle injections provide higher film effectiveness than simple-angle holes due to increased lateral spreading of the jet, particularly at high BR. The latter also found effectiveness improvement is reduced for higher pitch-to-diameter ratio (p/d) of 6.0 as the jets no longer coalesce as they do for p/d=3.0. Figure 2.2 shows the compound angle geometries examined by Schmidt et al. [5]. Leylek and Zerkle [6] recommended a minimum hole length-to-diameter (l/d) ratio of 4.0 to avoid skewed coolant velocity profiles that result in lower effectiveness.

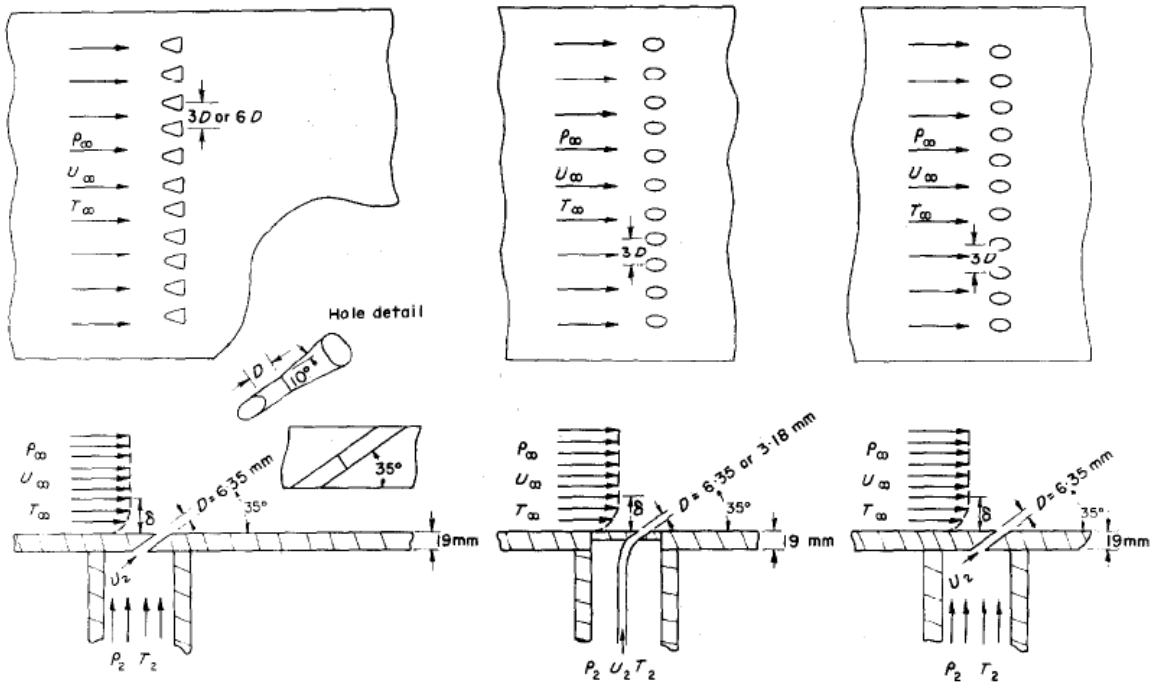

Figure 2.1: EARLY HOLE GEOMETRIES. GOLDSTEIN [1]

Flow visualization and computation studies of jet in a cross-flow show formation of a pair of vortices at high blowing ratios that are detrimental to film cooling. These vortices entrain hot mainstream gas underneath the jet and reduce film coverage. Figure 2.3 from Haven et al. [7] shows a visualization of this effect. In order to mitigate the entrainment effect and prevent jet lift-off, the holes are expanded near the exit, either in the lateral direction

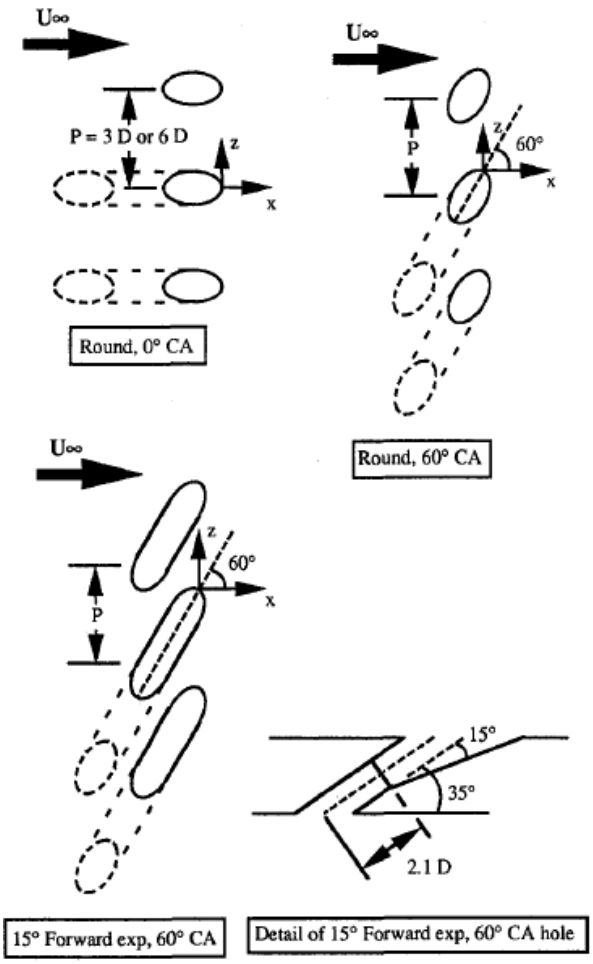

Figure 2.2: COMPOUND ANGLE HOLES. SCHMIDT ET AL. [5]

(fan-shaped), or forward direction (laidback), or both (laidback fan-shaped). Goldstein et al. [1] was perhaps the first to show the benefit of using shaped holes (they used 10° fan-shaped geometry) over simple CY holes. They attributed the increased effectiveness with shaped holes to the reduced mean velocity of the secondary fluid at the exit. Gritsch et al. [8] showed that laidback fan-shaped holes are more effective than the fan-shaped holes and both shapes outperform simple-angle holes by a good margin. Unlike simple-angle holes which show decreasing effectiveness with BR, laidback fan-shaped hole performance improved with BR, in the investigated range of 0.5 to 1.5, due to decreased jet momentum and lateral spreading of the jet.

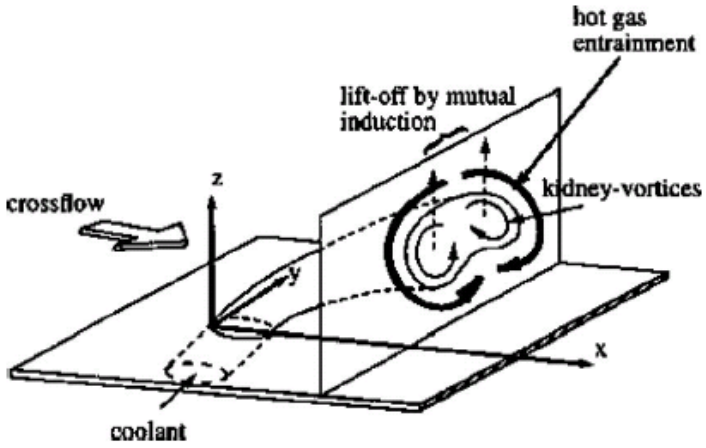

Figure 2.3: DIAGRAM OF JET LIFTOFF. HAVEN ET AL. [7]

There are however limitations to shaped film hole design, mainly because of cost concerns, machining accuracy, and availability of material thickness for shaping, as noted by Bunker [9] in his review of shaped hole film cooling. Many other unique cooling hole designs have been proposed in recent years to overcome the so called kidney vortex and improve film cooling effectiveness. Ideas such as struts within the holes (Shih et al [10]), cusp-shaped holes (Papell [11]), triangular tabs at the hole exit (Zaman and Foss [12]), trenched holes (Bunker [13], Lu et al. [14]), double jet configuration (Kusterer et al. [15]), and dumbbell and bean shaped holes (Liu et al. [16]) have been proposed and studied. Figure 2.4 shows an example of trenched holes, while Fig. 2.5 shows the more complex dumbbell and bean shapes. Many of the proposed designs are shown to be effective in this regard, but the majority of these ideas prove to be difficult to manufacture and/or produce unwanted features such as additional solid surfaces that must be cooled or additional sharp edges that are aerodynamic liabilities.

Another method of enhancing film cooling is embedding the injection holes in a trench, providing a more gradual exit into the mainstream that allows for more spreading of the jet. Some examples of research into embedding injection holes in a trench has been conducted by Baheri et al [17] in 2008, Zuniga and Kapat [18] in 2009, and Lu et al [19] in 2009. The

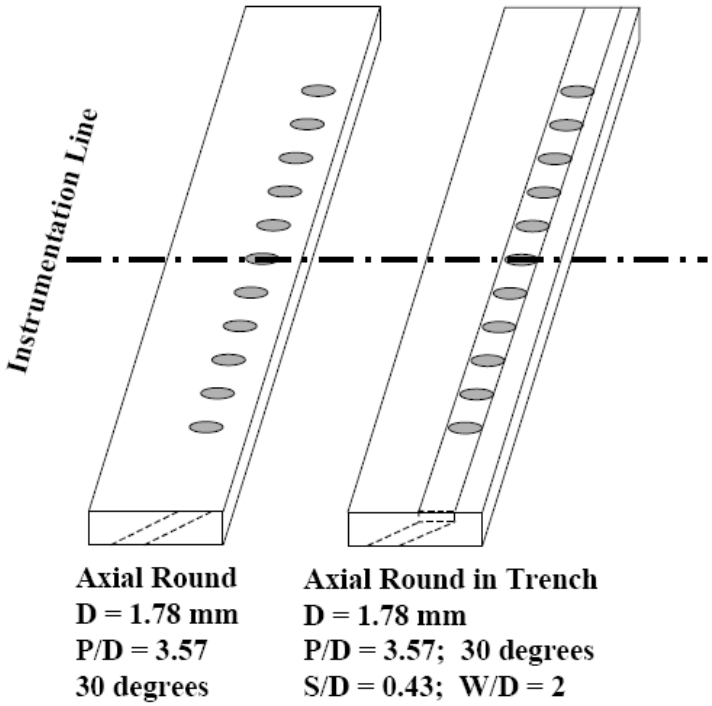

Figure 2.4: TRENCHED HOLES. BUNKER [13]

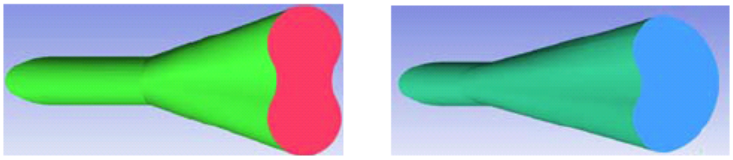

Figure 2.5: DUMBBELL AND BEAN HOLES. LIU ET AL. [16]

general consensus arrived at by the researchers is that entrenching holes is advantageous for cylindrical and compound angle holes, but shows no benefit, and even some detriment, to the effectiveness for shaped holes.

Literature on flat plate experiments is quite extensive, no doubt due to the simplicity of the test arrangement. Experimental data for vane and blade geometries is not as common, and is also dependent upon many factors such as the specific blade profile and injection hole locations. Drost et al [20] performed a study in 1997 that compares flat plate results to cascade airfoil results. Their experiments on the airfoil, which was of unspecified profile, show

somewhat reduced effectiveness on the suction side as compared to the flat plate results. Of interest were their results for the pressure side, which showed a greatly reduced effectiveness as compared to the flat plate tests, which is attributed to both an increased injection angle and very high blowing ratio of slightly under 4, resulting in very pronounced flow separation.

A useful review of the state-of-the-art was published by Bunker [9] in 2005. Bunker notes that the majority of work in film cooling research has been done using flat plate rigs, and that the majority of experimental work on the flat plate rigs has focused on the cylindrical injection hole design. More recent work has started to focus on shaped hole designs and testing on cascade rigs. He concludes with the note that shaped injection holes are the current standard, with benefits such as little variation in effectiveness over a range of blowing ratios, resistance to jet lift-off and low sensitivity to free stream turbulence, and drawbacks such as higher aerodynamic mixing losses.

More extreme hole designs have been proposed and tested, though many of these have manufacturability issues that prevent them from being implemented using currently available technology. Ghorab and Hassan [21] in 2010 proposed and tested a hybrid film hole geometry that exits the plenum at 30° and then has a bend such that the top section of the fan shaped hole exits at 10° to the mainstream flow direction. Figure 2.6 is the geometry as tested. This has the effect of spreading the flow laterally and greatly reducing the vertical momentum, resulting in high effectiveness. The manufacturability of this design is questionable with current technology, as the bend in the injection hole leaves no clear path for drilling the section on the plenum side. A potentially more easily manufactured hole design that was tested on an airfoil by Liu et al [22] is referred to as the console hole. This design utilizes a near circular shape at the inlet that converges in the axial direction and diverges in the lateral direction and results in a wide slot at the exit. This design provides good coverage on both the suction and pressure sides, but does have issues with the manufacturing process.

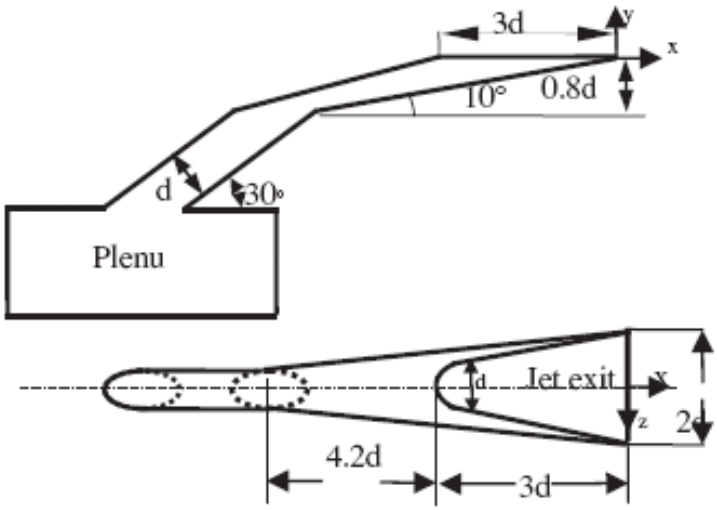

Figure 2.6: BENT HOLES. GHORAB AND HASSAN [21]

The tripod hole design aims to invalidate the central kidney vortex using a much simpler approach. The holes in this design are cylindrical in geometry and therefore easy to manufacture. The 3-hole design can also provide alternate pathways for the secondary fluid to eject should there be plugging of holes due to deposition. The computational fluid dynamics (CFD) study by Heidmann and Ekkad [23] evaluates the detailed flow features associated with the hole design. Various configurations of the tripod hole concept have been tested experimentally by Dhungel et al. [24] that include variations in the side hole ejection location relative to the main hole and side hole-to-main hole diameter ratio. Figure 2.7 shows the tested cases from their study. For this research, configuration 3 is picked from the aforementioned study with two important geometric alterations first, the side hole-to-main hole diameter ratio is increased to 1.0 from 0.5 and lower used in earlier studies, and second, the pitch-to-diameter ratio is increased from 3.0 to 6.0 in order to accommodate the larger diameter of the side hole. These alterations are necessitated by the practical limitations in drilling the smallest hole diameter possible in turbine airfoils with the currently available technology. Additionally, alternative designs that include shaping of the hole exits are investigated, and all of the new designs are compared to cylindrical and shaped hole geometries.

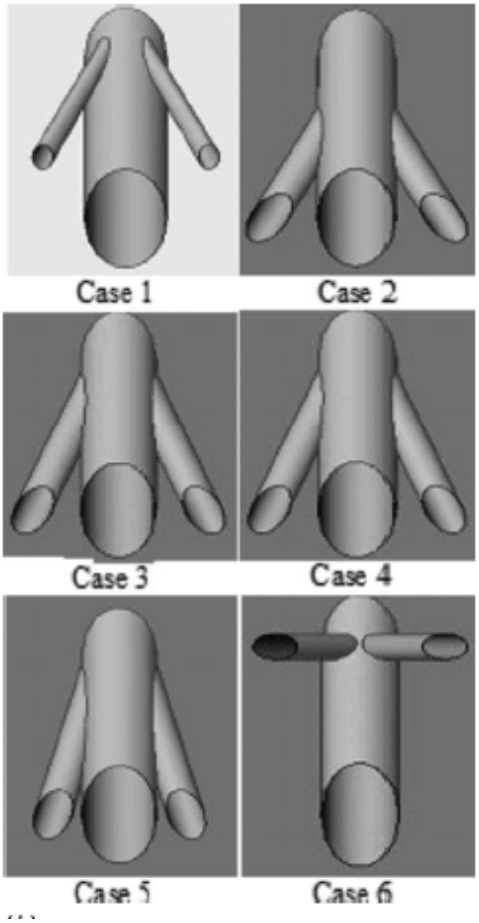

Figure 2.7: ANTIVORTEX HOLE CONCEPT. DHUNGEL ET AL. [24]

Interior passages are cooled by passing bleed air from the compressor through the channels, often with pin fins, ribs/turbulators or impingement schemes to enhance the heat transfer. The use of rib turbulators for heat transfer enhancement is the most common form of enhancement for internal passages. Han [25] showed that the heat transfer inside turbine blade passages is influenced by flow Reynolds number, rib configuration, and channel aspect ratio. The aim was to find optimal values for rib geometry such as rib height, pitch, and angle of with respect to the flow (60°, 90°, etc.). Han [26] provided heat transfer results for square and rectangular channels with different rib turbulator spacings. This study provides a correlation for estimating heat transfer inside rib turbulated channels that is still used by

gas turbine designers to estimate cooling requirements for turbine blades in modern engines. Han et al. [27] studied heat transfer augmentation with a variety of rib turbulator configurations. They showed that there is no significant penalty on pressure drop associated with the use of complex rib formations to enhance heat transfer. Zhang et al. [28] studied partial and fully ribbed walls in triangular channels that represent the leading edge region channel for turbine airfoils. They developed and presented a correlation for predicting heat transfer for triangular channels with ribs. Taslim et al. [29] also studied leading edge channels with more realistic curved surfaces. Ekkad and Han [30] used a transient liquid crystal technique to determine detailed heat transfer coefficients in a ribbed twopass square duct. They varied channel Reynolds numbers and rib geometries, and clearly showed the local enhancement caused by flow separation and reattachment downstream of the ribs, as well as the associated secondary flow induced heat transfer enhancement. Many of the above studies have focused on simplified channel geometries. Han et al. [31] provided an extensive literature survey in their book on various studies that have been performed on ribbed coolant channels. However, little data has been presented for all sides of the channel geometries in the literature which is the secondary focus of this dissertation.

Turbine designers use correlations developed using simplified geometries and apply them to the complex channel geometries of the actual blade. However, there has been little data available to evaluate the validity of the predicted values for the complex channels. Engine tests tend to obfuscate the effects of internal cooling since they are altered by external heat transfer (film cooling, etc.). Poser et al. [32] conducted transient heat transfer experiments in a model of a multi-pass gas turbine blade cooling circuit. The inner surface of the plexiglass model was coated with thermochromic liquid crystals in order to determine the internal heat transfer coefficients. The experiments were conducted with an engine-representative Reynolds number, Mach number and heat flux direction as in a real blade. They evaluated

their method and performed an uncertainty analysis which demonstrated robustness for the investigated geometries. This study is the first to focus on an actual engine type internal cooling configuration and make detailed heat transfer measurements in such channels and compare to standard correlation predictions used by designers.

3. Experimental Setup

Three separate test rigs are used for this research. The first test rig is a flat plate test rig that allows for both transient and steady-state experiments, using IR thermography to capture the surface temperature. The second test rig is a scaled up linear cascade that allows for steady-state experiments using IR thermography to capture the surface temperature. The third test rig is a three pass internal channel test rig that allows for transient experiments using liquid crystal thermography to capture the surface temperature.

3.1 Flat Plate Test Rig

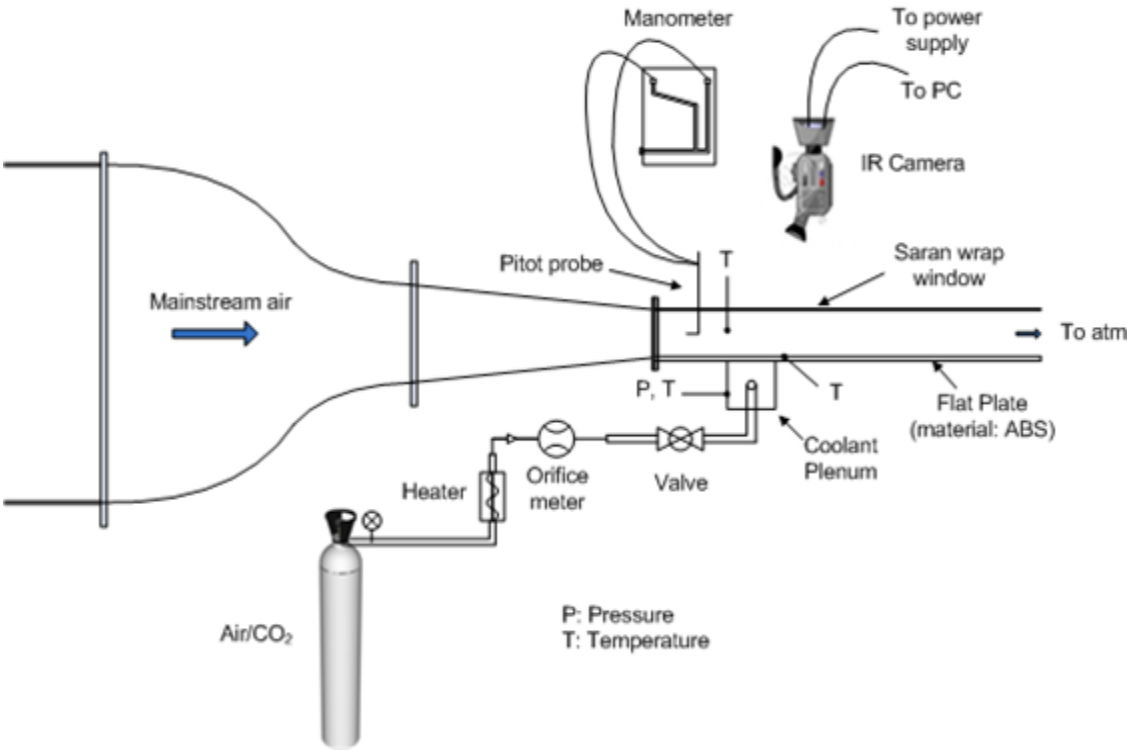

Figure 3.1: SCHEMATIC OF FLAT PLATE TEST RIG

Flat plate models are an ideal test bed for proof-of-concept study. A schematic of the flat

plate test section used in this research is shown in Figure 3.1. Room temperature air travels through two contracting nozzles and a series of two screens before entering the flat plate test-section. The two screens are connected to a high power welder that acts as a DC power supply, allowing the screens to be used as a resistance heater able to supply a fast temperature rise to the mainstream flow. The mainstream velocity and temperature are monitored, respectively, by a Pitot probe and a thermocouple, both located 20-cm downstream of the test section inlet. The velocity of the mainstream is fixed at 7.9m/s. The boundary layer on the base plate is tripped by a 4.7mm diameter wire placed at a distance of 5cm from inlet to ensure turbulent and uniform flow across the width of the test section. The 101.6cm long test section has a constant cross-sectional area of 7.62cm (height) 30.5cm (width). The base plate of the test section is constructed of 2.54cm thick low thermal conductivity ABS material (k=0.187 W/mK). A hollow cavity in the base plate accommodates a mating piece with cooling hole geometry imprinted on it. This replaceable plate was grown in a rapid prototyping machine using a resin similar in thermal properties as the ABS base plate. When sitting flush in the cavity, the holes are at a distance of 30.5cm from the inlet. Underneath the replaceable plate is a plexiglass chamber that acts as a plenum for the secondary fluid, which can be either heated or room temperature. The chamber is significantly large in comparison to the cumulative inlet area of the holes to be safely considered as a plenum (28 cm long by 14 cm wide by 15 cm tall). The secondary fluid pressure and temperature are monitored by three wall pressure taps and a thermocouple in addition to two 36-gage thermocouples placed inside two holes. The secondary flow loop comprises a gas supply tank, an orifice (ORIPAC, Lambda Square Inc.) for flow metering, and a heater. Note that in the steady-state tests the mainstream air is essentially at room temperature while the secondary gas is heated, while in the transient tests the mainstream air is heated and the secondary gas is at room temperature.

3.2 Cascade Test Rig

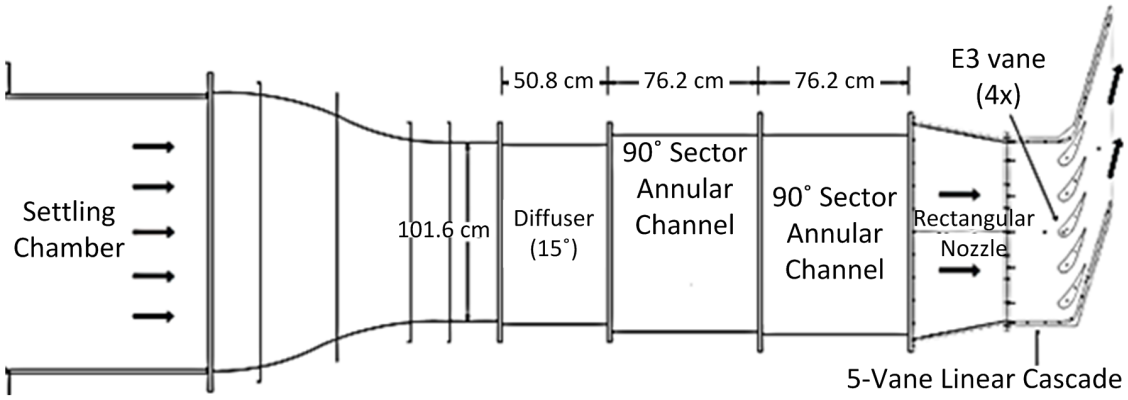

Figure 3.2: SCHEMATIC OF CASCADE TEST RIG

Figure 3.2 shows an open loop flow channel consisting of a blower, an inlet section, a combustor simulator section, a nozzle, and a 5-vane linear cascade. The blower (Cincinnati Fans, 900 CFM max. capacity) is fitted to a 15 hp motor having a maximum speed of 3525 RPM. To obtain the desired flow, the motor is controlled by a Rockwell Automation V-TAC controller. The blower pushes air into the inlet section comprising of a settling chamber, a converging nozzle, and a diffuser. The diffuser is connected to a turbine combustor model consisting of two one-quarter annular channels that can be separated by a plate holding three equally spaced swirlers. Scaled up two times its original size, these swirlers will impart high degree rotation to the passing flow. The swirlers are not used in the experiments presented here, but are available for future testing of more realistic turbulence levels and its effect on film cooling. The linear vane cascade is comprised of five E3 vanes, built from low conductivity ABS resin by Fused Deposition Method (FDM). This method allows complex geometries to be built at fraction of the machining cost. The vanes are scaled up four times their original size to match the size of the upstream combustor geometry. The resultant vane chord, height, pitch, and absolute flow angle are 13.49 cm, 15.24 cm, 17.78 cm, and 73.1°, respectively. The walls of the vane test section are made of clear acrylic material to

permit obstruction-free optical measurements, and with viewing windows cut into the top and bottom plates of the cascade for IR thermography. The maximum flow velocity that can be obtained at the inlet of the vane cascade is 20m/s. The secondary gas is injected through an inlet pipe into the central cavity of the test blade, which is sufficiently large in comparison to the injection holes to act as a plenum. The secondary gas flow is metered through an orifice (ORIPAC, Lambda Square Inc.) and is heated by an inline pipe heater.

3.3 Three Pass Test Rig

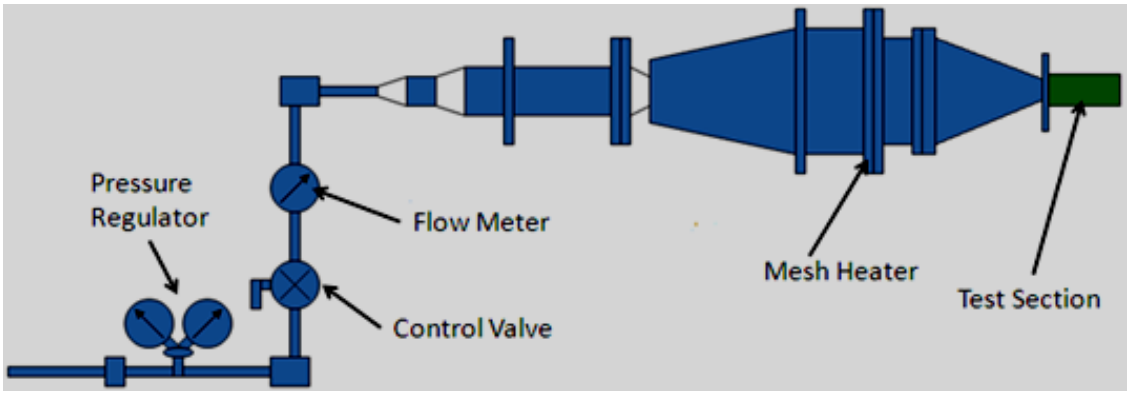

Figure 3.3: SCHEMATIC OF THREE PASS TEST RIG

Figure 3.3 shows the experimental setup used for the three pass experiments. Compressed and metered air enters from a 50 mm round pipe and expands to a 35.56 cm x 15.24 cm plenum. The plenum allows the flow for a uniform velocity before passing through the mesh heater. The length of the plenum is 52 cm before the heater. At the exit of the plenum, a mesh heater constructed of 304-stainless steel woven wire with a wire diameter of 20 microns is placed. A 2 cm spacer separates the mesh heater and the reduction nozzle leading to the test section to complete the test rig. Power is supplied to the mesh heater by a welding machine power source providing low voltage, high amperage DC power. The test section walls are constructed from clear, acrylic, low thermal conductivity material to reduce conduction

losses during the experiment and to allow for visibility of liquid crystal color changes.

3.4 IR Thermography Technique

Wall temperature measurements are obtained with a FLIR ThermaCAM SC 640 camera. The camera has a range of -40-100°C with a 640 x 480 pixel resolution, in a 7.513 μm spectral range, and $\pm$2% or 2°C accuracy. The accuracy was further calibrated using a 36-gage thermocouple and adjusting the emissivity and transmissivity to less than 1.0°C. The test surface is viewed through a stretched polyurethane sheet window on the top plate of the test section. The sheet is thin, on the order of 5 μm, reducing the IR transmissivity to 0.9. Wall thermocouples are placed on the edge of the view area for calibration purposes during all the experiments.

3.5 Liquid Crystal Thermography Technique

The test section material is 0.64 cm thick clear acrylic which is a low conductivity, low thermal diffusivity material that is necessary for the transient liquid crystal technique. A thin layer of thermochromic liquid crystal paint (SPN R25C5W) is applied on the inside wall of test surface. The liquid crystal paint has a color play range between 25°C and 30°C. A thin layer of black paint is applied behind the liquid crystal paint to provide a background for the color changes during the experiments. The liquid crystal paint was calibrated in-situ during the test using a foil thermocouple glued to the target surface. Since the color is calibrated in-situ during each experiment, the issue of lighting, camera placement, and other conditions do not affect the calibration curve. A new calibration curve is generated for each specific test. The color is expressed in Hue and calibrated to the corresponding thermocouple

temperature. A Canon FS2000 color CCD camera capable of capturing images at a frame rate of 30 frames per second and resolution of 1024x768 pixels is used to record the transient response of the liquid crystal color change. The camera stores data locally on an SDHC card and transfers to a PC later through a USB connection.

3.6 Mesh Heater

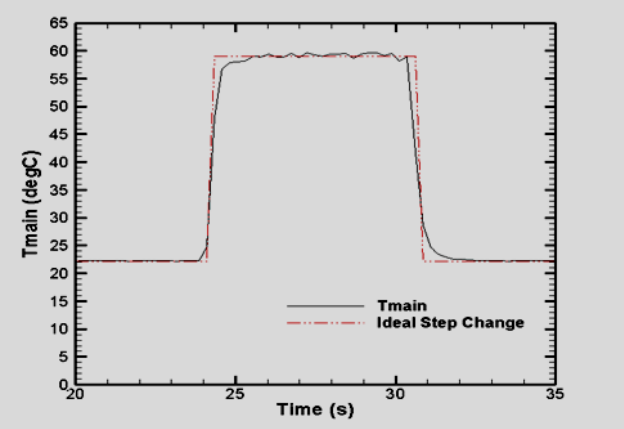

Figure 3.4: MESH HEATER TEMPERATURE RESPONSE

The transient tests are conducted with the use of a mesh heater, which is a fine stainless steel mesh stretched across the mainstream flow and attached to a welder that provides low voltage, high amperage DC power. The mesh heater allows the assumption of a true step change in mainstream temperature during the transient test. The heater reaches steady state temperature in less than 33 milliseconds and therefore a step change in temperature is assumed in the calculations. The heater temperature was measured using an IR camera with a 30 Hz frame rate. After capturing the images, the IR camera images showed that the temperature on the heater was uniform immediately at the first image which is 33 milliseconds after initiation of the heater and remained steady after that. Figure 3.4 shows the temperature response of the mesh heater during an experiment. A true step change

is also shown on the figure. However, the thermocouple has a time constant of 1 second which is larger than the IR camera response and therefore cannot show the instantaneous temperature change. The thermocouple response shows much higher time to capture the heater response due to higher time constant.

4. Experimental and Data Reduction Techniques

The test data consists of temperatures from thermocouples, temperatures from IR thermography and colors from liquid crystal thermography. This data must be processed in order to calculate the useful parameters of η and h. The following sections describe the process used to convert the raw data into η and h values.

4.1 Liquid Crystal Color to Temperature Conversion

The video from the color camera is initially in terms of Red, Green and Blue (RGB) values. The first step in the data processing for the liquid crystal data is to convert the RGB values into Hue, Saturation and Value (HSV) numbers. Using HSV, the color is presented as a single value, independent of the brightness of the image. This reduces the reliance on perfectly even lighting and allows for a simpler lighting setup.

The second step in the data processing for the liquid crystal data is use the thermocouple temperature data to provide a calibration curve that is plotted in terms of temperature vs hue, using the timestamps on the thermocouple data and the known start time and frame rate of the video to align the time between the two data sets. Once this data is plotted as temperature vs hue, a linear curve fit is applied to the plot, which results in a calibration equation.

$$T = x * H + c \tag{4.1}$$

With this equation, every pixel of every frame can then be expressed as a temperature.

4.2 Steady-state Effectiveness

The steady-state film cooling experiments all utilize the IR thermography method, which provides data in the form of temperatures for every pixel of every frame. During these steady-state tests, the mainstream flow is started and allowed to run until initial steady-state is reached. The determination of when the test surface has reached steady-state is made by charting the temperature reported by the surface thermocouple previously used to calibrate the IR camera. Once the thermocouple is reporting an unchanging temperature, the initial temperature is captured and labeled as T_∞. The secondary gas is then started and set to the appropriate flowrate and temperature for the specific test being run. The target temperature difference between the mainstream and secondary gas is 25 °C. The flow rate and temperature data are then monitored until a new steady-state is reached, again determined by the surface thermocouple ceasing to show a change in temperature. Once this new steady-state has been achieved, the final temperature is captured and labeled as T_{steady}. The secondary gas temperature is read from a thermocouple just before the injection point and labeled as T_{sg}. These values are then used to calculate the adiabatic film cooling effectiveness using

$$\eta = \frac{T_{steady} - T_\infty}{T_{sg} - T_\infty} \tag{4.2}$$

These values are the extent of the data available from steady-state experiments, and are useful in comparing the performance of different film cooling injection holes.

4.3 Transient Heat Transfer Coefficient

The three pass experiments utilize the liquid crystal thermography in a transient experiment to calculate the heat transfer coefficient (h) at the surface of the test fixture. The test is a short duration test, no more than 10 seconds for a given run. This, combined with the low thermal conductivity of the acrylic plate, allows the assumption of one dimensional conduction into a semi-infinite solid. The captured temperature data is used in the equation [33]

$$\frac{T(0,t) - T_i}{T_m - T_i} = 1 - exp\left(\frac{h^2 \alpha t}{k^2}\right) erfc\left(\frac{h\sqrt{\alpha t}}{k}\right) \tag{4.3}$$

which is solved iteratively for h to minimize the error between the calculated $T(0,t)$ and the temperature from the recorded data. The data for the three pass experiments is presented using the non-dimensional Nusselt number [34]

$$Nu = \frac{hd_h}{k} \tag{4.4}$$

4.4 Transient Heat Transfer Coefficient and Steady-state Effectiveness

The transient film-cooling tests use a technique that is a hybrid between the steady-state and transient procedures. Temperature data is collected at initial steady-state and final steady-state as before, as well as during the first five seconds of heated mainstream and injected coolant flow. The η values are calculated using Eqn. 4.2 with a heated mainstream flow instead of a heated secondary gas. These calculated η values are then used in a modified

form of Eqn. 4.3

$$\frac{T_{transient} - T_i}{\eta T_{sg} + (1-\eta)T_\infty - T_i} = 1 - exp\left(\frac{h^2 \alpha t}{k^2}\right) erfc\left(\frac{h\sqrt{\alpha t}}{k}\right) \tag{4.5}$$

This modified equation takes into account the difference in the mainstream temperature that is created by injecting a coolant fluid. Equation 4.5 is then solved iteratively for h to minimize the error between the calculated $T(0,t)$ and the temperature from the recorded data, using the same algorithm as before. To best represent the data, the values of h have been normalized with h_0, which is the heat transfer coefficient without film cooling present. This may be calculated by first using the Colburn analogy for turbulent flow [34]

$$Nu_x = 0.0296 Re_x^{0.8} Pr^{1/3} \tag{4.6}$$

to find the Nusselt number, and then solving for h_0

$$h_0 = \frac{Nu_x k}{x} \tag{4.7}$$

4.5 Heat Flux Ratio

The heat flux ratio [31] is a measure of the heat load on the surface of the test plate, and is defined by

$$\frac{q''}{q''_0} = \frac{h}{h_0}\left(1 - \frac{\eta}{\phi}\right) \tag{4.8}$$

where ϕ is defined as

$$\phi = \frac{T_g - T_w}{T_g - T_c} \tag{4.9}$$

which is the overall cooling effectiveness of the engine and ranges from 0.5 to 0.7.

5. Initial Exploration of the Tripod Hole

Initial testing of the tripod hole concept to determine viability for further testing is presented in this chapter. These tests were conducted on the flat plate test rig previously described, using the steady-state IR technique with room temperature mainstream flow and heated secondary flow. Results are presented in the form of adiabatic wall effectiveness.

5.1 Hole Geometries

Initial exploration of the tripod hole concept focused on a comparison between three geometries, as shown in Fig. 5.1. The first geometry is a simple CY hole of diameter 6.35 mm and axis inclined at 30° from the surface in the streamwise direction. The hole length-to-diameter ratio (l/d) is 7.5 and the pitch-to-diameter ratio (p/d) is 3. There are a total of 13 holes on the plate. The second geometry is a 3-hole unit in which the main or the central hole is identical to the first geometry but has an additional CY hole on either side that branch out at 15° angle and connected together at the inlet such that the metering area at the entrance of the secondary flow is circular. All three holes are inclined at 30° angle from the surface. The l/d ratio of the center and the side holes is 7.5 and 7.7, respectively. The p/d ratio between the main holes is 6d, between the center and the side hole is 1.75d, and between the side holes of the adjacent tripod unit is 2.5d. There are a total of 7 sets of tripod holes on the plate. The design is akin to removing alternate holes in the CY design and adding two angled holes to each of the remaining holes. The third geometry shares the same hole characteristics as the second, with the holes ending in a trench recessed into the surface of the plate. In order to maintain the same geometry, this necessitated a thicker test plate. Because of the ease with which complex geometries can be built in quick time at a fraction

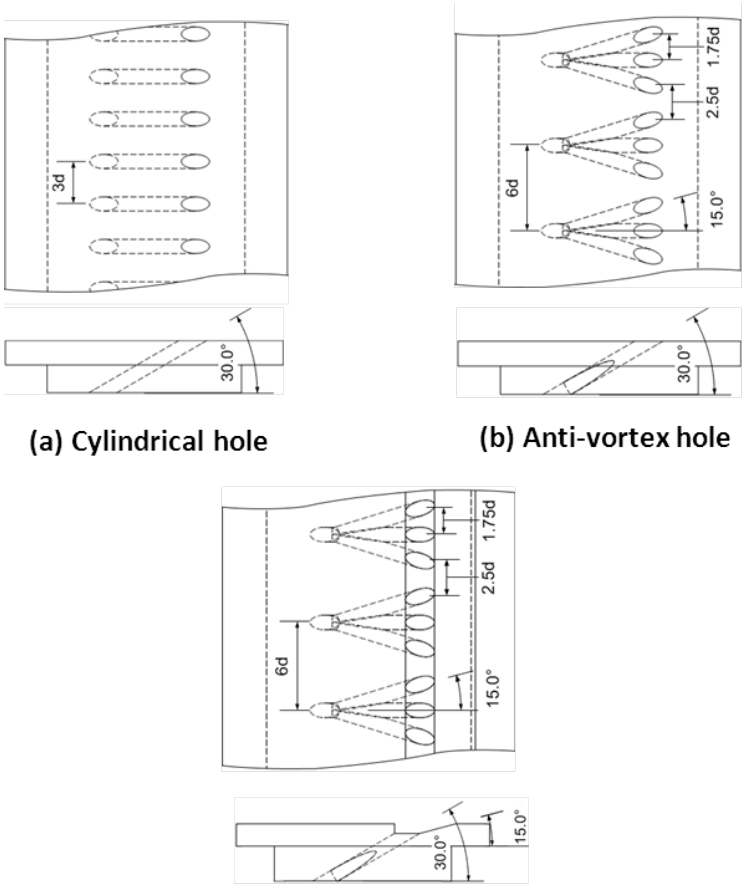

Figure 5.1: INITIAL HOLE GEOMETRIES

of the machining cost, the geometries were grown with the rapid prototyping technique.

5.2 Test Conditions

As shown in Table 5.1, there are a total of 25 experiments performed to study the effects of blowing (BR) and density ratio (DR) on adiabatic film-cooling effectiveness. BR is defined as

$$BR = \frac{(\rho V)_{sg}}{(\rho V)_{\infty}} \tag{5.1}$$

where V_{∞} is the mainstream air velocity at the test section inlet averaged over the entire span. The mass flow rate for a given blowing ratio is given by:

$$\dot{m} = \sum_{i=1}^{n} BR(\rho V)_{\infty} a_i \tag{5.2}$$

and DR is found by applying the ideal gas law

$$DR = \frac{\rho_{sg}}{\rho_{\infty}} = \frac{(RT)_{sg}}{(RT)_{\infty}} \tag{5.3}$$

5.3 Computational Method

Computational grids were created for two geometries. Figure 5.2 highlights the grid quality near the hole intersection region for the AV hole geometry. Both AV and CY grids encompassed one complete set of holes with the boundary located at a plane midway between adjacent center holes. Symmetry boundary conditions were applied at both of these planes and the k- turbulence model was utilized. Inflow boundary conditions were prescribed at

Table 5.1: SUMMARY OF INITIAL EXPERIMENTAL CONDITIONS

Exp	Hole	BR	DR	I	$\dot{m}(kg/s)$
1	CY	0.5	0.95	0.263	0.0019
2	CY	1.0	0.95	1.052	0.0038
3	CY	1.5	0.95	2.368	0.0057
4	CY	2.0	0.95	4.210	0.0076
5	CY	0.5	1.45	0.172	0.0019
6	CY	1.0	1.45	0.689	0.0038
7	CY	1.5	1.45	1.551	0.0057
8	TR15	1.0	0.95	1.052	0.0021
9	TR15	1.5	0.95	2.368	0.0032
10	TR15	2.0	0.95	4.210	0.0041
11	TR15	3.0	0.95	9.473	0.0062
12	TR15	4.0	0.95	16.84	0.0082
13	TR15	1.0	1.45	0.689	0.0021
14	TR15	1.5	1.45	1.551	0.0032
15	TR15	2.0	1.45	2.758	0.0041
16	TR15	3.0	1.45	6.206	0.0062
17	TR15-Tr	1.0	0.95	1.052	0.0021
18	TR15-Tr	1.5	0.95	2.368	0.0032
19	TR15-Tr	2.0	0.95	4.210	0.0041
20	TR15-Tr	3.0	0.95	9.473	0.0062
21	TR15-Tr	4.0	0.95	16.84	0.0082
22	TR15-Tr	1.0	1.45	0.689	0.0021
23	TR15-Tr	1.5	1.45	1.551	0.0032
24	TR15-Tr	2.0	1.45	2.758	0.0041
25	TR15-Tr	3.0	1.45	6.206	0.0062

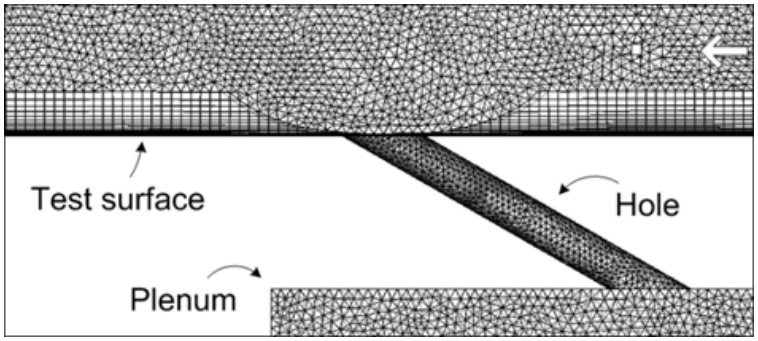

Figure 5.2: COMPUTATIONAL GRID (SIDE VIEW)

the freestream and plenum inlet locations. The mainstream velocity was set at 7.9 m/s to match the experimental conditions on the test rig and the plenum inlet velocity was varied to create the desired blowing ratios. The free-stream inlet is 20-hole diameters upstream of the main hole leading edge. Blowing ratios of 0.5 and 1.5 were used for the cylindrical hole geometry, while blowing ratios of 1.0 and 3.0 were used for the anti-vortex geometry. The temperature difference between the mainstream and the plenum was set to 25°C to provide for the effectiveness calculation while maintaining similar density between the mainstream and coolant. The exit pressure was set to atmospheric pressure at the exit location 40-hole diameters downstream. Calculations were performed with adiabatic wall conditions to complement the experimental case, which did not use a heated wall. No slip boundary conditions were used at all wall surfaces. A grid independence study was undertaken for the AV and CY hole geometries. For the AV hole case, four grids were examined; these grids contained 142,753, 341,416, 1,552,551 and 5,689,479 computational cells. The two largest grids gave similar results, so the decision was made to use the 1,552,551 cell grid. This grid maintains a y+ value of less than 1.25 within 10 diameters of the hole exit. For the CY hole case, three grids were examined; these grids contained 63,134, 505,074 and 1,487,818 computation cells. The two largest grids gave similar results, with the 1,487,818 cell grid reaching convergence more quickly and therefore, being the grid chosen. This grid maintains a y+ value of less than 1.5 within 10 diameters of the hole exit. The computations were performed using the ANSYS-CFX code, and the convergence criterion was set to RMS residuals of 1e-4. Convergence was achieved in 8 hours or fewer for each case. We did not compare our wall temperature predictions from CFD with our experiments as we could not refine our grid to match the experiments.

5.4 Experimental Uncertainty

Uncertainties were estimated based on the procedure described by Coleman and Steele [35]. The mainstream velocity was kept constant within ±1.3%. Uncertainties in setting the blowing ratio was ±3%. Based on an accuracy of ±0.5°C for the thermocouple measurement and an accuracy of ±1°C for IR measurement, the uncertainty in adiabatic effectiveness amounted to ±5% for η=0.5 and ±10.0%for η=0.15.

5.5 Film Cooling Effectiveness Measurement

5.5.1 Effects of hole geometry

Figure 5.3 shows the film effectiveness contours for the three geometries at selected BRs and constant DR of 0.95. Each plot covers a downstream distance of approximately 34d starting from the hole leading edge. Figure 5.3a shows the effectiveness measured downstream of a row of cylindrical holes. Well-defined peaks downstream of the hole centerline and valleys in between are observed close to the holes, especially at low BRs. The lateral variations smear out at large distances downstream owing to diminished jet strength. As BR is increased, the peaks grow smaller and smaller, and at the highest BR, there are no discernible peaks and valleys. The presence of low effectiveness spots (dark blue color) at BR=2.0 is in fact an evidence of jet detaching from the surface and then reattaching downstream. The observations are in line with those observed in previous studies.

Figure 5.3b is a similar plot for the tripod holes with three units shown in each plot. The rationale behind using a 3-hole geometry is twofold one is to expand the exit area with the intention of lowering the jet momentum and thereby delay lift-off, much like that of a shaped

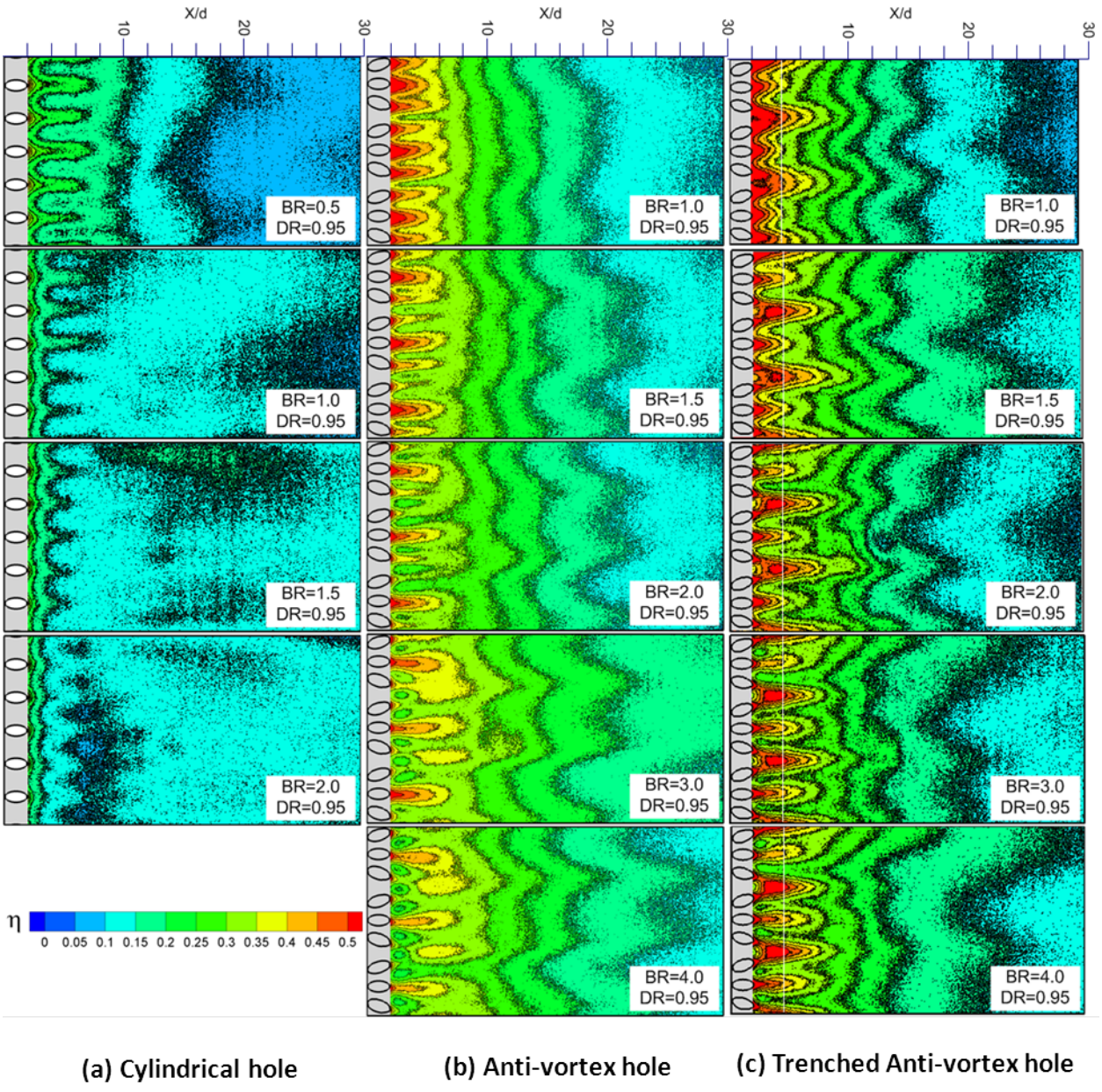

Figure 5.3: ADIABATIC FILM COOLING EFFECTIVENESS DISTRIBUTION FOR THE THREE GEOMETRIES DR=0.95

hole concept, and second, to create identical vortices from the side holes to invalidate the main kidney vortex and thereby reduce vortex- induced entrainment effect. The dramatic improvement in effectiveness in the immediate vicinity of the tripod holes confirms the working of this theory even with minor modifications in hole size and spacing. It is interesting to note that at moderate to high BRs, the side hole traces are fainter in comparison to that of the main hole despite all having the same cross-sectional flow area. The jets merge downstream still maintaining good coverage for a significant distance. At high BRs of 3.0 and 4.0, regions of high effectiveness (colored yellow) appear between tripod units not seen in smaller BRs. This is believed to be an outcome of high momentum jets from the side holes of adjacent tripod unit forming secondary counteracting anti-vortex pairs. The BR at which these secondary tripod pairs start to develop is a function of the divergence angle and the spacing between the side holes. It is conjectured that a slightly larger divergence angle (say, 20°) and/or a shorter p/d value (say, 5d) between the main holes would advance this phenomenon to a smaller value of BR.

Figure 5.3c is a similar plot for the trenched tripod holes with three units shown in each plot. The rationale behind the trench is to allow for an intermediate change in the flow angle instead of the abrupt change as seen in traditional designs. Compared to the standard tripod design, there is an increase in effectiveness in the region of the trench itself and similar performance downstream of the trench region. There are regions of higher effectiveness between the adjacent tripod units due to the interactions of the side jets inside the trenches, and these are not limited to high BR cases like the standard tripod design.

Figure 5.4 shows the laterally-averaged film effectiveness results for the three geometries at equal blowing ratios for two different density ratios. It is clear that the tripod geometries outperform the baseline CY geometry at all blowing ratios. For low BR cases, the trenched tripod geometry has similar performance to the tripod geometry; however as the BR reaches

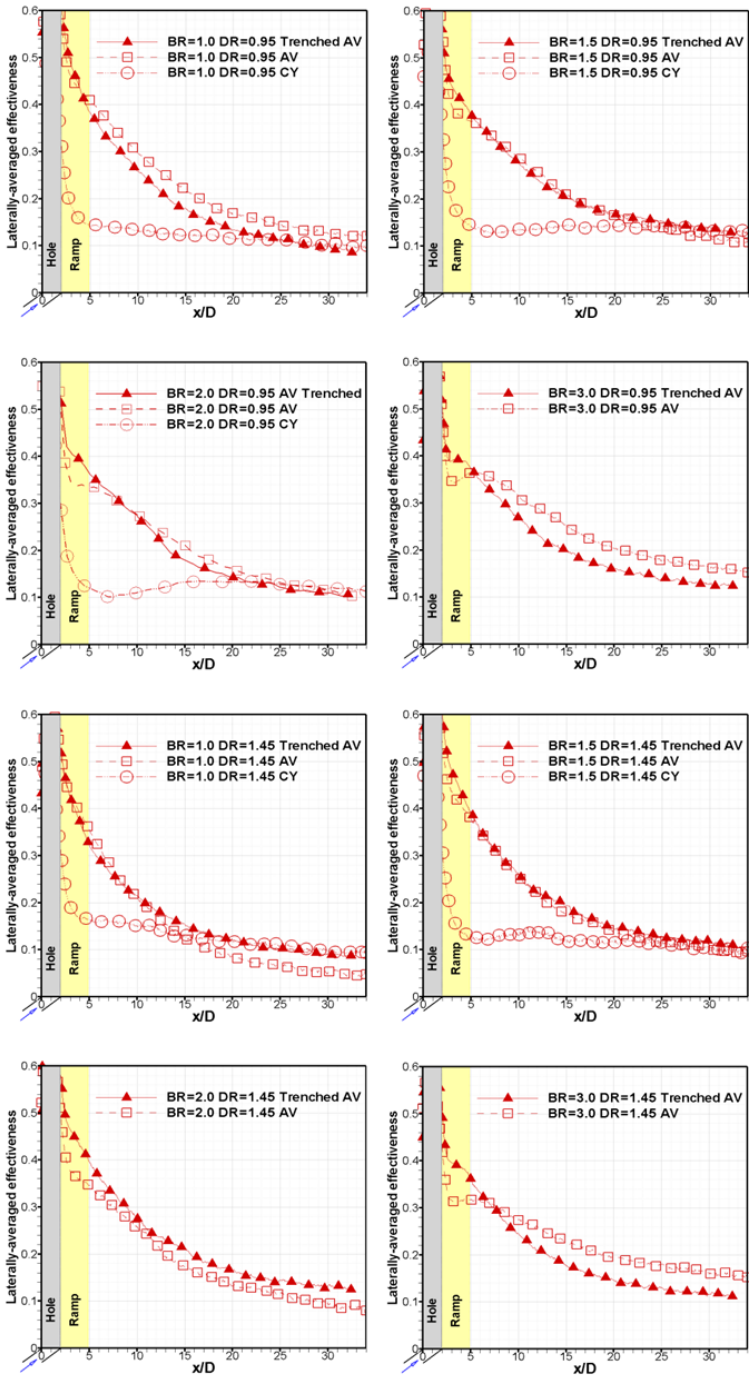

Figure 5.4: COMPARISON OF THREE HOLE GEOMETRIES OPERATING AT SAME BR AND DR

2.0 and 3.0 there is a clear advantage to the trenched tripod geometry in the trench region itself, with behavior beyond the trench being similar for both the tripod and trenched tripod cases at BR 2.0. At BR 3.0 there is a clear downstream advantage for the tripod case. The tripod and trenched tripod cases are both superior to the CY case at all BR and DR combinations studied.

Figure 5.5 shows the laterally-averaged film effectiveness results for the three geometries at similar mass flow rates. The data shows, that for higher mass flows, the benefits of the tripod geometries are substantial, mostly due to the lack of a liftoff effect as seen in the CY cases. The consistency in effectiveness between mass flow rates for the tripod cases lessens the burden on designers to provide the optimal coolant flow, while also increasing the effectiveness of the coolant that is supplied. More importantly, more cooling is effected on the surface with less coolant mass flows. Also, there is a very limited effect of blowing ratio for the tripod cases indicating that the cooling flow can be maintained at the lowest possible blowing ratios without affecting cooling performance.

Figure 5.6 shows secondary flow vectors from the CY and tripod hole cases at four planes normal to the surface. The BR values in the tripod hole cases are twice that of the CY hole cases shown to simulate same overall mass flow rate through each hole. The DR value used is 0.95 in all the cases. The well known kidney vortex pair can be seen developing downstream of the CY hole, particularly at BR=1.5, where the jet is strong enough to maintain the vortex shape well beyond a distance of 10d. The up-wash motion seen at the center of the kidney vortex is responsible for the lift-off phenomenon that plagues CY holes at high BR. It is quite clear that the main jet from the AV hole remains closer to the surface than the CY jet even at BR=3.0 (see x=1d plane). The down-wash motion of the side vortices help keep the main jets attached to the surface besides drastically reducing the size and strength of the detrimental kidney vortex of the main jet. However, the strong up-wash motion of the same

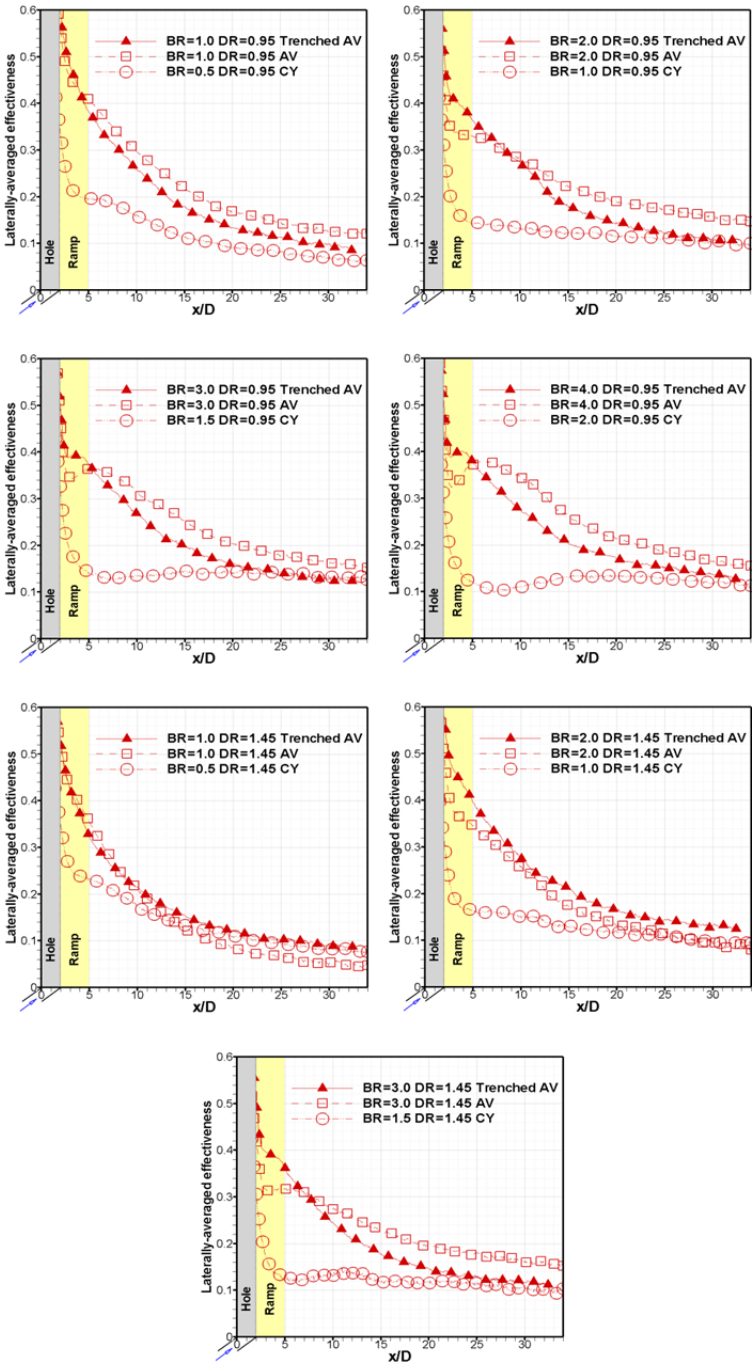

Figure 5.5: COMPARISON OF THREE HOLE GEOMETRIES OPERATING AT SAME $\dot{m}$ AND DR

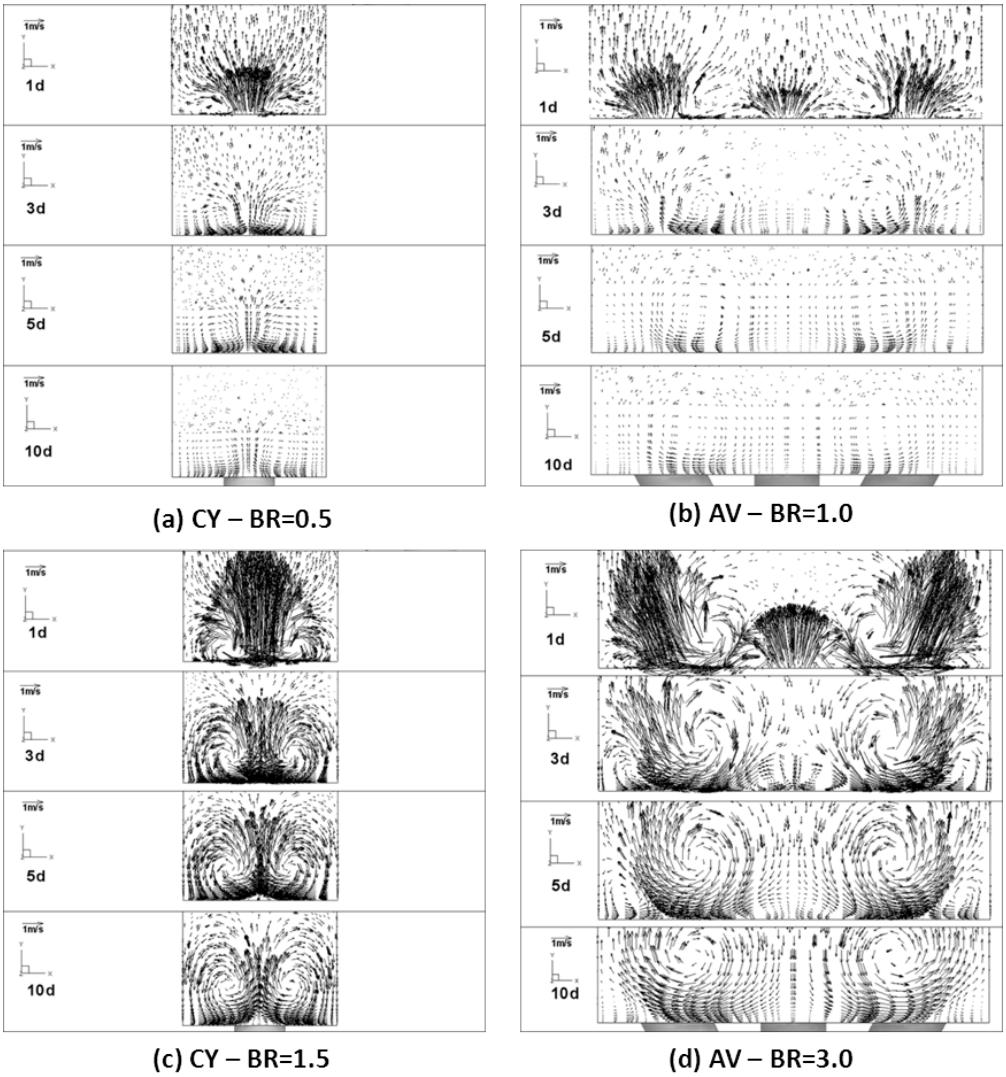

Figure 5.6: CFD FLOW VISUALIZATION – CY AND TRIPOD HOLES

side vortices can push some of the side jets into the mainstream, particularly at high BR. This, together with the fact that stronger jets are issued from side holes may explain why in Fig. 5.3b the traces from the side holes at BR=2.0 and above are weaker in comparison to the main trace.

5.5.2 Effects of blowing ratio

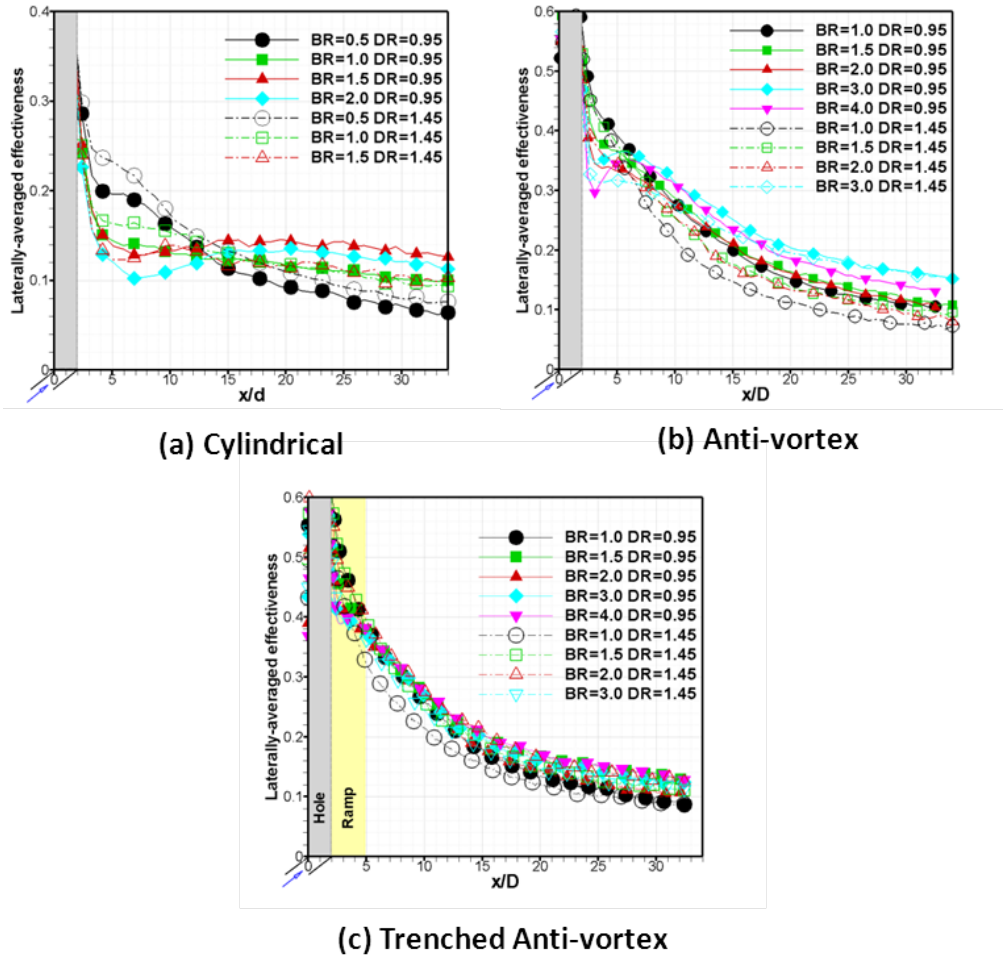

Figure 5.7: EFFECT OF BR AND DR FOR EACH GEOMETRY

A better understanding of the film cooling phenomena can be obtained by cross plotting some

of the data to show the influence of BR. Figure 5.7 shows laterally-averaged effectiveness distributions at three different downstream positions for the two hole geometries. With cylindrical holes, the general trend near the holes is that of decreasing effectiveness with BR. The decline in film cooling effectiveness with increasing blowing is attributed to the penetration of the secondary fluid jets into the mainstream. Further downstream (x/d=20), the trend is different altogether. The secondary gas at low BR does not have adequate momentum to travel far downstream, thus producing low effectiveness magnitudes. The improved effectiveness at high BR is due to detached jets bending back and reattaching on the surface. At still higher BR, complete reattachment of the jet may not be possible, leading to a drop in effectiveness once again, as is evident in the case of BR=2.0.

Since for a given BR, relatively smaller mass flow supply is required with tripod holes, two additional BRs of 3.0 and 4.0 have been tested; the mass flow at BR=4.0 being nearly equal to that of BR=2.0 with CY holes. Close to the hole, the trend is identical to the corresponding cylindrical hole case, i.e., effectiveness decreases with increasing BR. The improvement at high BRs is suspected to have come from the fringes of the high effectiveness secondary zones that develop when the neighboring tripod side holes interact, as reattachment is unlikely at such a short distance. Farther downstream, a slowly rising effectiveness is an indicator of the jet reattachment phenomenon gaining strength with increasing BR, besides the positive contribution from the high effectiveness secondary zones. The utility of tripod holes can be gauged by the fact that for any given BR, the effectiveness level with tripod holes at a far downstream distance is almost at par with the effectiveness level of CY holes at the nearest hole distance

5.5.3 Effects of density ratio

To determine the effect of DR variation on film cooling, some tests were performed using CO_2 as the secondary gas. A combination of molecular weight and temperature difference between CO_2 and mainstream air produced a density ratio of 1.45 for this study. The performance of CO_2 vis--vis air is also plotted in Fig. 5.7 at various BRs for the CY hole case. In the near hole range, the heavier gas shows higher effectiveness at all BR except at BR=1.5 where the level is about the same. Farther downstream, the heavier gas provides better cooling effectiveness at BR=0.5, is similar with the lighter gas at BR=1.0, and provides poorer cooling than the lighter gas at BR=1.5. The improved showing by the heavier gas near the holes is because of the propensity of the heavier jet to stay attached to the surface that keeps the jets from lifting off and mixing with the mainstream air. For the tripod holes in Fig. 5.7b, in the near hole region, the intermediate BRs of 1.5 and 2.0 display high film effectiveness with the heavier gas. At BR=3.0, the heavier gas is not as effective as the lighter gas as seen from the low effectiveness values in that region. Farther downstream, the heavier gas fares poorly in comparison to the lighter fluid irrespective of BR. The very low momentum flux ratio (see Table 5.1 for tripod holes) is probably the reason why BR=1.0 and DR=1.45 case displays the lowest effectiveness of all tripod hole cases studied. The relatively low momentum flux ratio helps the heavier fluid to stay closer to the surface and provide protection in the near vicinity of the holes but is unable to sustain that coverage for a longer distance downstream. As a consequence, the performance drops dramatically away from the holes. BR higher than 3.0 could not be tested using CO_2 because of unavailability of a tank big enough to supply gas throughout the entire steady-state experiment.

Generally, momentum flux ratio (I) and not BR is considered as a better scaling parameter

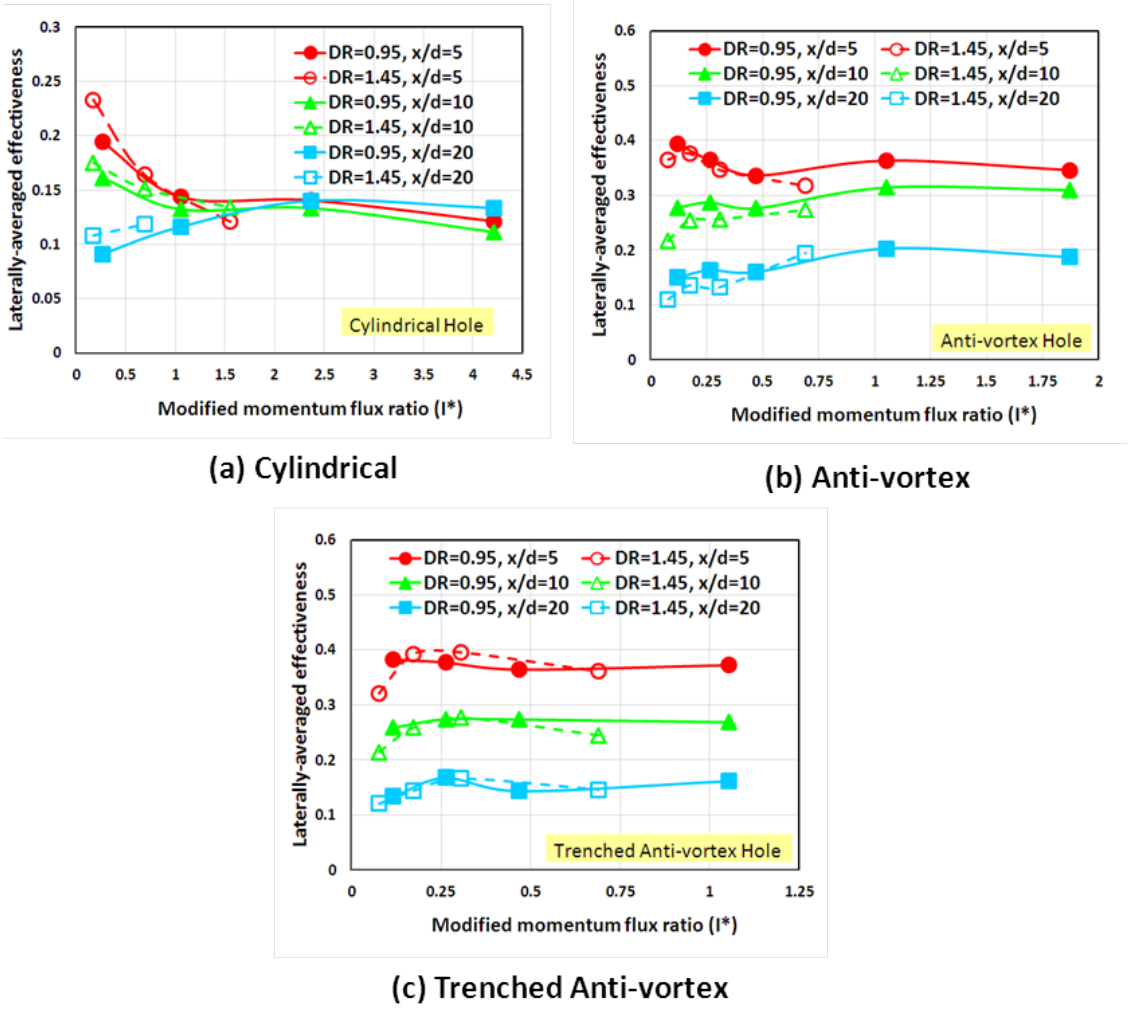

Figure 5.8: OVERALL EFFECTIVENESS AS A FUNCTION OF MODIFIED MOMENTUM FLUX RATIO

for secondary gases of different densities operating in the high BR regime.

$$I = \frac{BR^2}{DR} \tag{5.4}$$

A further generalization is possible by introducing a parameter AR (exit-to-inlet hole area ratio) to account for the different hole shape at the exit. This parameter

$$I^* = \frac{BR^2}{DR * AR^2} \tag{5.5}$$

defined as the momentum flux ratio normalized by the exit-to-inlet hole area ratio squared, appears to correlate well effectiveness maxima for shaped holes with that of the cylindrical holes [1]. Since AV holes work on a similar principle of expanded exit, it is worthwhile to draw a plot of effectiveness as a function of I^*. For the tripod holes, the value of AR is 3.0 whereas for the CY holes, it is 1.0. As seen in Fig. 5.8a for the case of CY holes, the two different fluids are seen to correlate well at the three downstream positions considered. The effect of coolant density is to alter the mainstream velocity at the same blowing ratio. Effectiveness drops off rapidly at higher blowing ratios for the CY holes. Figure 5.8b is the corresponding plot with tripod holes. Figure 5.8c is the corresponding plot with trenched tripod holes. The trend for density ratio is similar with all the results on almost single line with increasing I*. It is to be noted that close to the holes (x/d=5) the maximum film cooling effectiveness in Fig. 5.8 appears to occur at a value of around 0.1, which is similar to the value obtained in Fig. 5.7, suggesting the usefulness of this parameter in predicting the jet lift-off. The values in Fig. 5.8 show little variation other than a small dropoff at very low values of I^*.

5.6 Conclusions

The key feature of this study is the use of a heavier gas with tripod hole configuration. The tripod holes in this study are different from the earlier studies in the sense that all three holes are of the same size and that called for increased spacing between the tripod units. Some of the main highlights from the study are presented below:

1. Tripod hole design significantly increases film cooling effectiveness immediately downstream of the holes compared to the CY hole design and with only half the mass flow supply (for a given BR). This increase is brought about by the combination of vortex cancellation effect and smaller mean velocity of the exiting secondary jet.

2. For the cylindrical holes, BR=2 would be maximum but if if the same flow rate was employed for the tripod holes, The blowing ratio would be BR=4. The high mass flow rate cases indicate no reduction in film effectiveness at high BR for tripod holes.

3. At sufficiently high BRs of 3.0 and 4.0, regions of high effectiveness appear between tripod units, believed to be a consequence of adjacent side holes forming a secondary counteracting vortex pair that deter mainstream entrainment.

4. As a consequence of this, larger BRs show better film cooling performance than the smaller BRs in the region downstream (x/d¿5). Closer to the holes (x/d¡5), however, the effectiveness trend follows that of a typical cylindrical hole, i.e, effectiveness falls with increasing BR.

5. The use of CO_2 as a secondary gas gives higher effectiveness close to the holes but performs poorly downstream when compared to air. This is observed to be true for all three types of holes.

6. It is shown that the three different geometries and two different fluids could be correlated by introducing the exit-to-inlet area of the hole geometry and by considering momentum flux ratio as the key scaling parameter in the high BR regime.

7. Finally, with the tripod hole design, it is possible to incorporate a smaller number of hole inlets on the internal side and have a large number of coolant exits on the gas side and still manage to use close to 50% less coolant and provide higher cooling effectiveness.

6. Tripod Holes in a Vane Cascade

The flat plate testing proved that the concept of the tripod hole was viable for further testing. The next step in the investigation is to test the performance of the new design on the pressure and suction sides of a realistic vane geometry. These tests were conducted on the cascade test rig previously described, using the steady-state IR technique with room temperature mainstream flow and heated secondary flow. Results are presented in the form of adiabatic wall effectiveness.

6.1 Airfoil Geometry

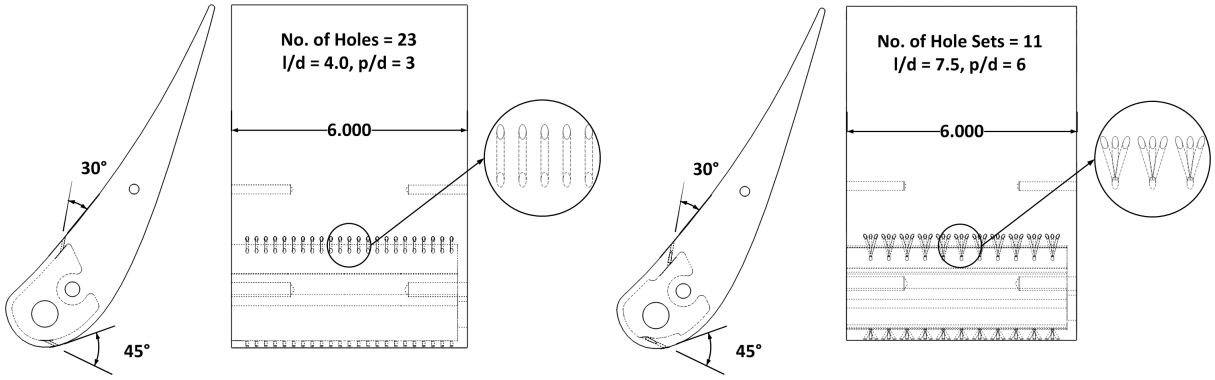

(a) VANE WITH CY HOLES (b) VANE WITH TRIPOD HOLES

Figure 6.1: VANE GEOMETRIES

The two hole geometries used in the experiments are shown in Fig. 6.1. The hole exits are located 3.2 cm from the true leading edge of the airfoil on the pressure surface. The first geometry is a simple CY hole of diameter 2 mm and axis inclined at 30° from the surface in the streamwise direction on the pressure side and inclined at 45° from the surface in the streamwise direction on the suction side. The hole length-to-diameter ratio (l/d) is 4.0 and the pitch-to-diameter ratio (p/d) is 3. There are total 23 holes on the vane. The

second geometry is a 3-hole unit in which the main or the central hole is identical to the first geometry but has an additional CY hole on either side that branch out at 15° angle and connected together at the inlet such that the metering area at the entrance of the secondary flow is circular. All three holes are inclined at 30° angle in the flow direction from the surface on the pressure side and inclined at 45° angle in the flow direction from the surface on the suction side. The l/d ratio of the center and the side holes is 7.5 and 7.7, respectively. The p/d ratio between the main holes is 6d, between the center and the side hole is 1.75d, and between the side holes of the adjacent tripod units is 2.5d. There are total 11 sets of tripod holes on the vane. The design is akin to removing alternate holes in the CY design and adding two angled holes to each of the remaining holes. The vanes are fabricated using the FDM method with ABS material.

6.2 Conduction Effect

Due to the blade geometry, secondary conduction through the wall from the plenum side to the mainstream side has a significant effect. A correction factor to allow for comparison to adiabatic surface conditions was developed using a conjugate CFD model representative of the actual geometry. Two cases were compared for each blowing ratio and geometry, one using the properties of ABS plastic, and one with near-perfect insulated surface. The temperature difference between the two cases was then used to calculate an effectiveness correction factor. This correction factor is the temperature difference between the two cases divided by the difference in temperature between the mainstream and coolant inlets.

$$\eta_{corr} = \frac{T_{plastic} - T_{ins}}{T_{sg} - T_{main}} \tag{6.1}$$

The greatest amount of correction is required in the region between and just upstream and immediately downstream of the hole exits, where the adiabatic cooling effectiveness is typically zero. The required correction is very small far downstream of the fluid injection location. Once applied to the data, this correction factor results in a reduced effectiveness compared to the raw experimental data, especially in the region around the holes. Figure 6.2a shows an example temperature correction contour for the cylindrical hole BR=1.0 case, while Fig. 6.2b and 6.2c show the effectiveness results pre- and post-correction for the cylindrical hole BR=1.0 case. Similar analysis was done for the all tested cases to determine the correction factors.

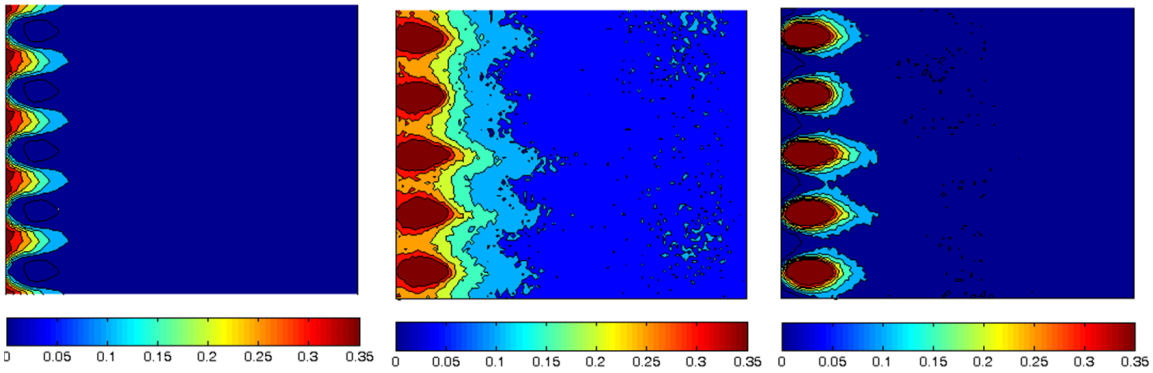

(a) CONTOUR (b) PRE-CORRECTION (c) POST-CORRECTION

Figure 6.2: CYLINDRICAL HOLE SAMPLE CONDUCTION CORRECTION

6.3 Test Conditions

As shown in Table 6.1, a total of 28 experiments were performed to study the effects of blowing (BR) and density ratio (DR) on adiabatic film-cooling effectiveness. From Table 6.1, it is important to observe that the tripod holes use 50% less coolant than the cylindrical holes for the same blowing ratio due to reduced number of inlet points for the tripod holes. The metering location for the holes is the inlet side of the holes which is the same in area

Table 6.1: SUMMARY OF CASCADE EXPERIMENTAL CONDITIONS

Exp	Side	Hole	BR	DR	I	$\dot{m}(kg/s)$
1	Suction	CY	0.5	0.95	0.263	0.001
2	Suction	CY	1.0	0.95	1.052	0.002
3	Suction	CY	1.5	0.95	2.368	0.003
4	Suction	CY	2.0	0.95	4.210	0.004
5	Suction	CY	0.5	1.45	0.172	0.001
6	Suction	CY	1.0	1.45	0.689	0.002
7	Suction	CY	1.5	1.45	1.551	0.003
8	Suction	CY	2.0	1.45	2.759	0.004
9	Suction	TR15	1.0	0.95	1.053	0.001
10	Suction	TR15	2.0	0.95	4.211	0.002
11	Suction	TR15	3.0	0.95	9.474	0.003
12	Suction	TR15	4.0	0.95	16.84	0.004
13	Suction	TR15	1.0	1.45	0.689	0.001
14	Suction	TR15	2.0	1.45	2.759	0.002
15	Suction	TR15	3.0	1.45	6.207	0.003
16	Suction	TR15	4.0	1.45	11.034	0.004
17	Pressure	CY	0.5	0.95	0.263	0.001
18	Pressure	CY	1.0	0.95	1.053	0.002
19	Pressure	CY	1.5	0.95	2.368	0.003
20	Pressure	CY	2.0	0.95	4.211	0.004
21	Pressure	CY	0.5	0.95	0.172	0.001
22	Pressure	CY	1.0	1.45	0.690	0.002
23	Pressure	CY	1.5	1.45	1.552	0.003
24	Pressure	CY	2.0	1.45	2.759	0.004
25	Pressure	TR15	1.0	0.95	1.053	0.001
26	Pressure	TR15	2.0	0.95	4.211	0.002
27	Pressure	TR15	3.0	0.95	9.474	0.003
28	Pressure	TR15	4.0	0.95	16.84	0.004

per hole for both geometries. For both geometries to push same mass flow, the tripod holes will operate at double the blowing ratio of the CY holes.

The blowing ratio is defined as ratio of the coolant to mainstream mass flux at the hole inlet.

$$BR = \frac{(\rho V)_{sg}}{(\rho V)_{\infty}} \tag{6.2}$$

where V_{∞} is the mainstream air velocity at the test section inlet averaged over the entire span. The mass flow rate for a given blowing ratio is given by:

$$\dot{m} = \sum_{i=1}^{n} BR(\rho V)_{\infty} a_i \tag{6.3}$$

and DR is found by applying the ideal gas law

$$DR = \frac{\rho_{sg}}{\rho_{\infty}} = \frac{(RT)_{sg}}{(RT)_{\infty}} \tag{6.4}$$

6.4 Experimental Uncertainty

Uncertainties were estimated based on the procedure described by Coleman and Steele [35]. The mainstream velocity was kept constant within ±1.3%. Uncertainties in setting the blowing ratios were ±3%. Uncertainties in the correction factor are estimated to be ±2.5%. Based on accuracy of ±0.5°C for thermocouple measurements and accuracy of ±1°C for IR measurements, the uncertainty in effectiveness amounted to ±5.0% for η=0.5 and ±10.0% for η=0.15.

6.5 Flow Characterization

A solid vane instrumented with pressure taps was used in the central vane location and measurements were taken to determine the pressure distribution and velocity profile on both the vane surface and the spanwise velocity profile upstream of the cascade. These measurements are necessary to characterize the oncoming flow towards the cascade and also to determine the vane loading.

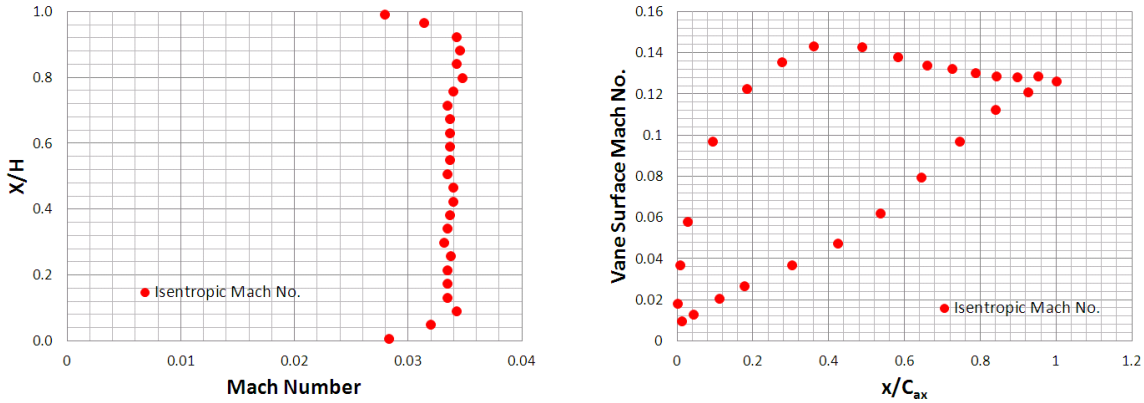

(a) SPANWISE INLET MACH PROFILE (b) BLADE SURFACE MACH PROFILE

Figure 6.3: FLOW CHARACTERIZATION

Figure 6.3a shows the spanwise velocity profile and Fig. 6.3b shows the vane surface velocity profile for the cascade. As shown in the figures, the flow is smooth over the vane with no detachment, and the spanwise flow is steady throughout the central region of the vane where the data is to be collected. The spanwise velocity measurement was made 0.5 axial chords upstream of the cascade inlet. The inlet velocity is fairly uniform entering the cascade at a Mach number of 0.035. The estimated boundary layer thickness at this point was 6-mm. From Figure 6, it is clear that the flow accelerates more rapidly along the suction surface compared to the pressure side. However, after reaching the maximum Mach number of 0.15 near the throat, the flow decelerates on the suction surface to an exit Mach number of 0.13.

6.6 Results

The cooling effectiveness measurements were made on the suction and pressure surfaces independently. For film cooling on the suction surface, the pressure side holes were sealed and no cooling flow was purges through and vice versa. A lateral average over a width of 15 hole diameters was taken for the cylindrical injection holes, while a width of 12 hole diameters was used for the anti-vortex holes.

6.6.1 Suction surface

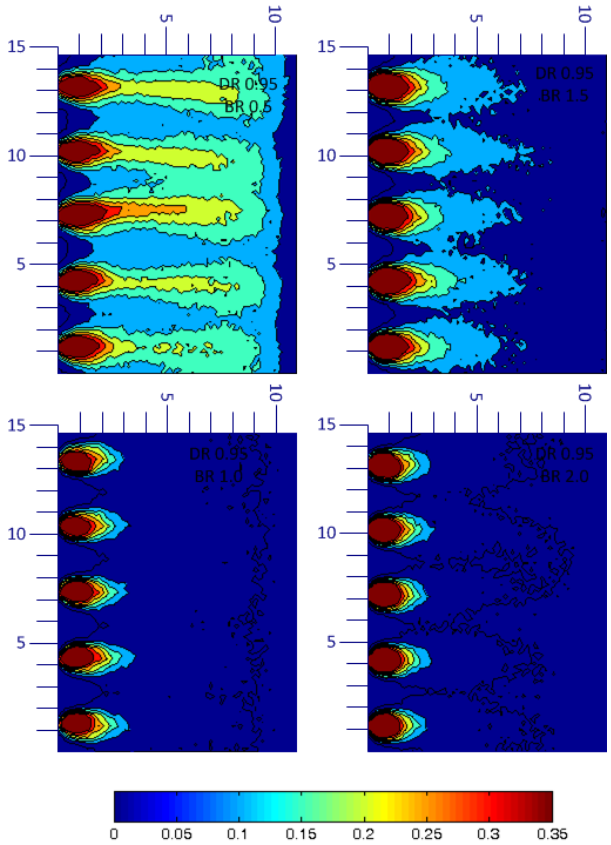

Figure 6.4: CORRECTED EFFECTIVENESS FOR CY SUCTION SIDE WITH AIR INJECTION

Figure 6.4 shows the conduction corrected effectiveness contours for the suction side cylindrical holes with air as the coolant gas. Due to the curvature of the blade and the low pressure of the mainstream flow, the jet lift-off effect seen in flat plate experiments above BR=1.0 is more pronounced. This results in the highest effectiveness being achieved at low blowing ratios, as well as very limited effectiveness beyond 10 hole diameters downstream.

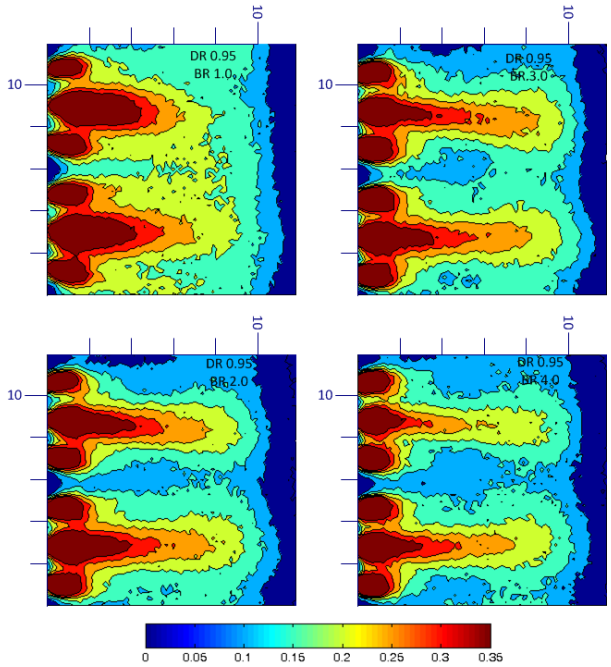

Figure 6.5: CORRECTED EFFECTIVENESS FOR TRIPOD SUCTION SIDE WITH AIR INJECTION

Figure 6.5 shows the conduction corrected effectiveness contour for the suction side tripod holes with air as the coolant gas. The data shows highest effectiveness at the lowest blowing ratio of BR=1.0, though the drop in effectiveness as the blowing ratio increases is less severe than that seen in the cylindrical holes case. The tripod holes spread the coolant using lesser total mass of coolant than the cylindrical holes and providing equivalent or higher coverage.

Figure 6.6 shows the laterally averaged effectiveness of all conduction-corrected cases for the cylindrical hole, suction side geometry with both coolant densities. The data shows that

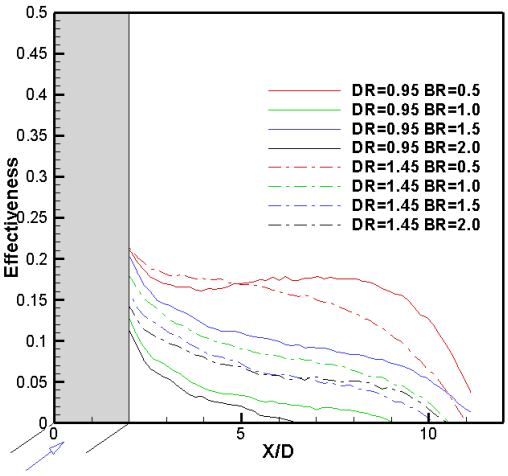

Figure 6.6: LATERALLY AVERAGED EFFECTIVENESS CY SUCTION SIDE

the lowest blowing ratio cases have the highest coolant effectiveness with steadily dropping levels of coolant coverage, with the exception of the DR=0.95 BR=0.5 case, which has low enough momentum for the coolant jet to re-attach after initial separation. Higher density coolant provides a moderate increase in effectiveness.

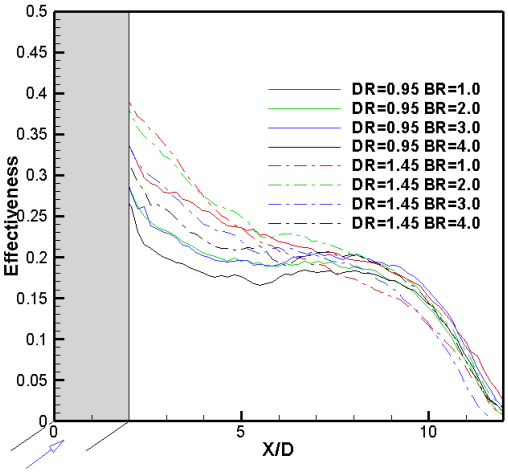

Figure 6.7: LATERALLY AVERAGED EFFECTIVENESS TRIPOD SUCTION SIDE

Figure 6.7 shows the laterally averaged effectiveness of all conduction-corrected cases for the

tripod hole, suction side geometry. Higher density coolant shows an enhancement near the hole exit, but rapidly converges to similar results to the lower density coolant cases. The tripod holes also show less variation between blowing ratios than the cylindrical holes, with the lower blowing ratios showing superior effectiveness to the higher blowing ratio cases. It should be noted that the difference in effectiveness between the different blowing ratios is less severe than that seen in the cylindrical cases.

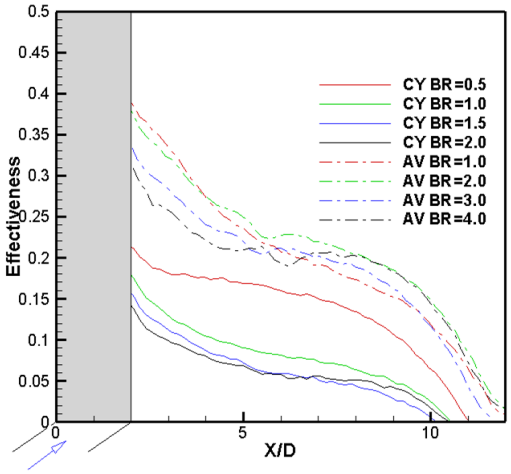

Figure 6.8: LATERALLY AVERAGED EFFECTIVENESS SUCTION SIDE WITH CO_2 INJECTION

Figure 6.8 shows a comparison of the laterally averaged effectiveness of all conduction corrected cases for cylindrical and anti-vortex holes with CO_2 as the coolant. The data shows that the tripod geometry provides significantly higher cooling effectiveness at all blowing ratios, with a more consistent level of coverage between cases. This trend is due to many factors of the tripod geometry, including lower fluid velocity at the exit and more spreading of the fluid across the surface. The highest effectiveness is achieved with the tripod geometry at BR=2.0. It should be noted that for a given mass flow, the tripod geometry will have double the blowing ratio of the cylindrical geometry due to the reduced number of inlets to the hole set. More importantly, the tripod hole provides longer coverage axially using lesser coolant mass.

6.6.2 Pressure side

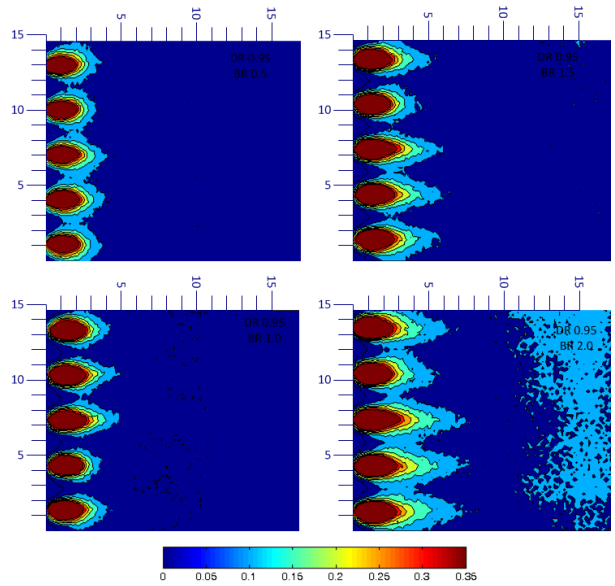

Figure 6.9: CORRECTED EFFECTIVENESS FOR CY PRESSURE SIDE WITH AIR INJECTION

Figure 6.9 shows the conduction corrected effectiveness contours for the pressure side cylindrical holes with air as the coolant gas. Due to the curvature of the blade and the higher pressure region of injection, the jet lift-off effect seen in flat-plate experiments above BR=1.0 are mitigated. Higher blowing ratios therefore are showing an increase in effectiveness. As can be seen from the contours of film effectiveness, coolant from the holes is largely entrained along the hole direction with limited effect beyond a few diameters downstream. Very little cooling is observed downstream due to rapid dissipation of the coolant jet effect. For a high blowing ratio of 2.0, we see a region of slightly higher effectiveness downstream due to jet lift-off at the hole and reattachment downstream.

Figure 6.10 shows the conduction corrected effectiveness contours for the pressure side tripod holes with air as the coolant gas. There is some asymmetry to these results, with the flow being biased more towards the angled holes, as opposed to the flow being biased towards

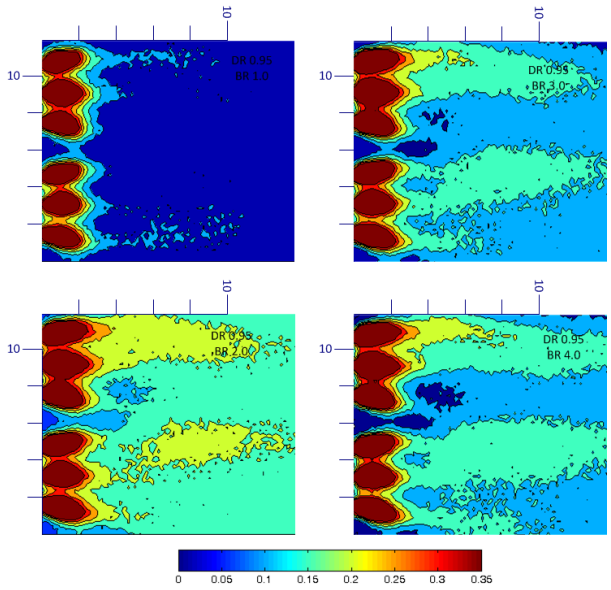

Figure 6.10: CORRECTED EFFECTIVENESS FOR TRIPOD PRESSURE SIDE WITH AIR INJECTION

the central hole as in the suction side data. This effect can be explained by the angled hole exits being more resistant to adverse pressure gradients than the hole directly aligned with the flow. The contours again show a mitigation of the lift-off effect, with the highest effectiveness being shown at the BR=2.0 case, and with BR=3.0 and BR=4.0 cases having greater effectiveness than the BR=1.0 case. The tripod hole spreads the coolant using lesser total mass of coolant than the cylindrical holes and providing equivalent or higher coverage. The impact of the geometry change on the cooling effectiveness distributions is not as significant on the pressure side as seen on the suction surface.

Figure 6.11 shows the laterally averaged effectiveness of all conduction-corrected cases for the cylindrical hole, pressure side geometry. The data shows an initial rapid drop in effectiveness downstream of the hole exit followed by a period of more constant values. The lowest blowing ratio cases have lower effectiveness than the highest blowing ratio cases with highest effectiveness at BR=2.0. Higher density coolant has a moderate enhancing effect at the lowest blowing ratios, and no change in effectiveness is seen at the highest blowing ratios.

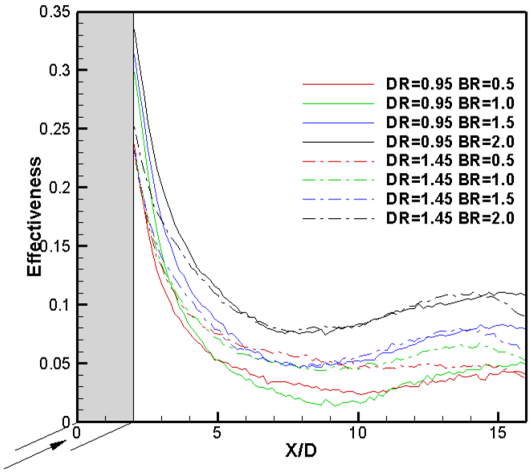

Figure 6.11: LATERALLY AVERAGED EFFECTIVENESS CY PRESSURE SIDE

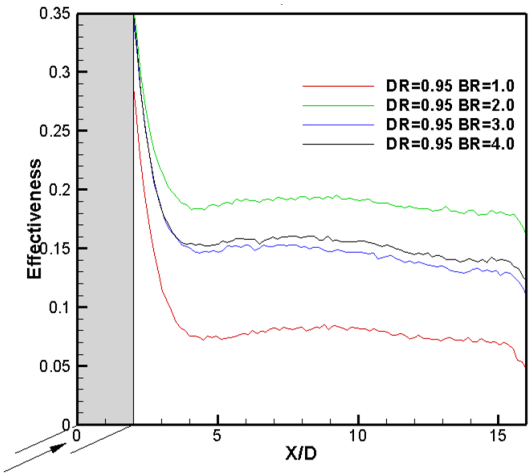

Figure 6.12: LATERALLY AVERAGED EFFECTIVENESS TRIPOD PRESSURE SIDE

Figure 6.12 shows the laterally averaged effectiveness of all conduction-corrected cases for the tripod hole, pressure side geometry with only air injection. The data shows an initial rapid drop in effectiveness downstream of the hole exit followed by a region of near-constant effectiveness. The lowest blowing ratio case shows the least effectiveness, with a peak effectiveness shown at BR=2.0 and a drop-off in effectiveness at higher blowing ratios. This dropoff for the highest blowing ratios is likely due to the thicker layer of coolant mixing more with the higher pressure flow.

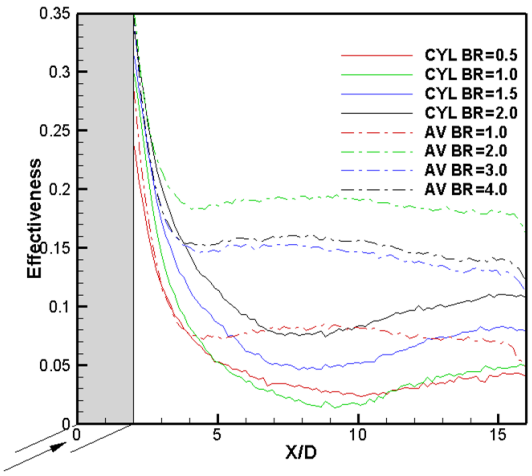

Figure 6.13: LATERALLY AVERAGED EFFECTIVENESS PRESSURE SIDE WITH AIR INJECTION

Figure 6.13 shows a comparison of the laterally averaged effectiveness of all conduction-corrected cases for cylindrical and tripod geometry with air as the coolant on the pressure side. The data shows enhanced levels of effectiveness for the lowest all blowing ratios for both geometries. The highest blowing ratio cases for the cylindrical hole geometry show an advantage over the lowest blowing ratio case for the tripod geometry. Jet lift-off and reattachment are indicated by a low effectiveness value followed by a higher value, as seen in the cylindrical geometry BR=1.5 and BR=2.0 cases. The tripod geometry at BR=2.0 shows the highest effectiveness of all cases. It should be noted that for a given mass flow, the tripod geometry will have double the blowing ratio of the cylindrical hole case due to the reduced number of inlets to the hole sets.

6.6.3 Overall averaged results

An alternate scaling parameter for secondary gases of different densities operating in the high blowing ratio regime is modified momentum flux ratio.

$$I^* = \frac{BR^2}{DR * AR^2} \tag{6.5}$$

Outlet to inlet area ratio (AR) is 1 for the cylindrical holes and 3 for the tripod holes.

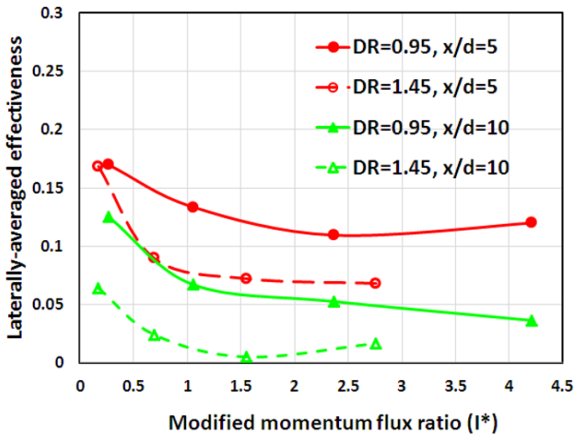

Figure 6.14: LATERALLY AVERAGED EFFECTIVENESS AS A FUNCTION OF I* FOR CY HOLES, SUCTION SIDE

Figure 6.14 shows the effect of I* on the effectiveness for cylindrical holes on the suction side of the blade. The data shows a general trend of decreasing effectiveness with increased I*, indicating that low I*, and hence lower blowing ratios, are desirable for this geometry. There is a significant difference between the results for low density coolant and high density coolant, with the high density coolant providing lower effectiveness at higher momentum flux ratios. Although, it is expected that the density ratio effect on the data would correlate with the momentum flux ratio as shown in several previous flat plate papers, the current data does not match the trend. It is not clear whether it is the effect of the hole location or

the relatively shallow angle of the streamwise angle on the high curvature region.

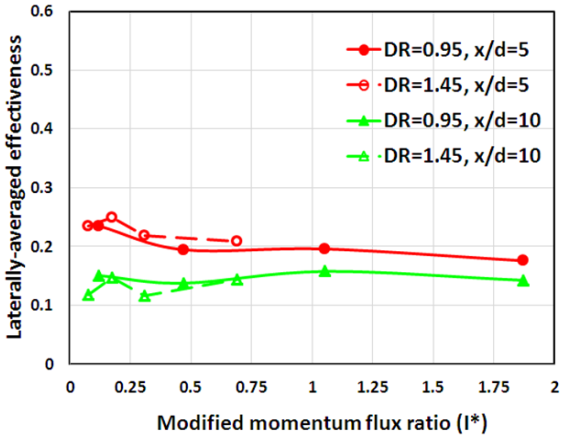

Figure 6.15: LATERALLY AVERAGED EFFECTIVENESS AS A FUNCTION OF I* FOR TRIPOD HOLES, SUCTION SIDE

Figure 6.15 shows the effect of I* on the effectiveness for tripod holes on the suction side of the blade. The data shows a steady effectiveness regardless of I*, allowing for a wider range of blowing ratios to be used without loss of performance. The density ratio has little effect on the performance of this geometry, as both tested coolant densities showed similar results. I* is an effective scaling parameter for this set of test cases.

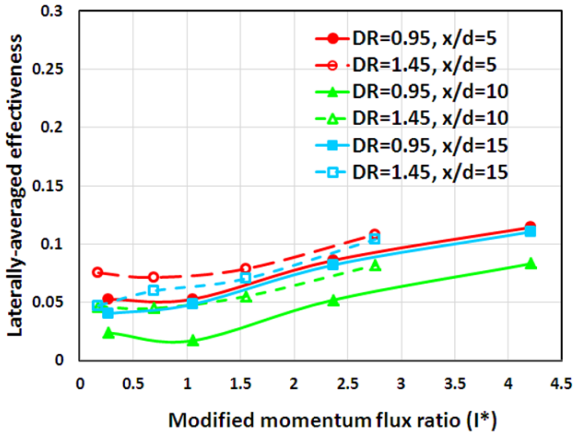

Figure 6.16: LATERALLY AVERAGED EFFECTIVENESS AS A FUNCTION OF I* FOR CY HOLES, PRESSURE SIDE

Figure 6.16 shows the effect of I* on the effectiveness for cylindrical holes on the pressure side of the blade. There is a general trend of increasing effectiveness as the momentum flux ratio increases, consistent across all density ratios and at all distances downstream from the hole. These results indicate that higher mass flow is desirable for cylindrical injection holes on the pressure surface of the vane, and that jet lift-off effects are mitigated by the combination of the pressure of the mainstream flow and the curvature of the pressure surface. I* is a better scaling parameter for these test cases than for the suction side cylindrical hole data.

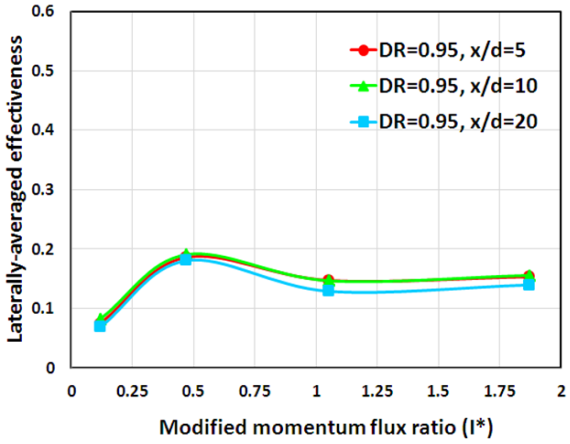

Figure 6.17: LATERALLY AVERAGED EFFECTIVENESS AS A FUNCTION OF I* FOR TRIPOD HOLES, PRESSURE SIDE

Figure 6.17 shows effectiveness at its highest near I*=0.5, with the lowest values for I*¡0.25. Effectiveness at I*¿1 is steady at a value between the minimum and peak values. I* is predicted to be a useful scaling parameter for these test cases based on the predictive power of I* for the AV suction side holes, as well as I* being reasonably predictive for the cylindrical pressure side holes.

The effectiveness values are, with the exception of the lowest flow case, higher than those achieved for the cylindrical holes geometry. The lowest flow tripod case has a higher effectiveness than all but the very highest flow cylindrical cases. In the most extreme example, near

I*=0.5, the tripod case shows a 250% increase in effectiveness over the cylindrical case. The tripod geometry shows clear advantages over the cylindrical geometry at any comparable I* value.

6.6.4 Aerodynamic loss measurements

All aerodynamic testing was conducted with unheated secondary gas flowing from both the suction and pressure sides of the vane.

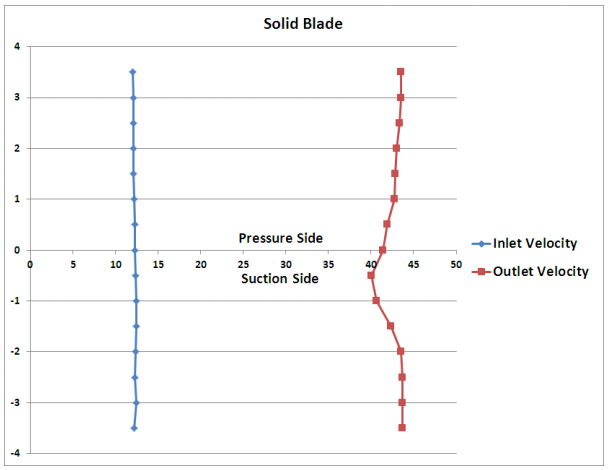

Figure 6.18: SOLID BLADE AERODYNAMIC PERFORMANCE

Figure 6.18 shows the inlet and exit velocity profiles of the flow with a solid blade, which serves as the baseline aerodynamic performance. The exit profile clearly captures the wake effect velocity deficit downstream of the vane. The deficit is clearly on the suction side of the passage due to migration of the secondary flow vortices towards the lower pressure side.

Figure 6.19 shows the inlet and exit velocity profiles of a blade with cylindrical injection holes on both the suction and pressure sides of the blades, at blowing ratios of 0, 0.5, 1.0, 1.5 and 2.0. The velocity profile is very similar to the solid blade case at low blowing ratios of 0 and 0.5, and beyond the 0.5 blowing ratio case the velocity profile is significantly altered.

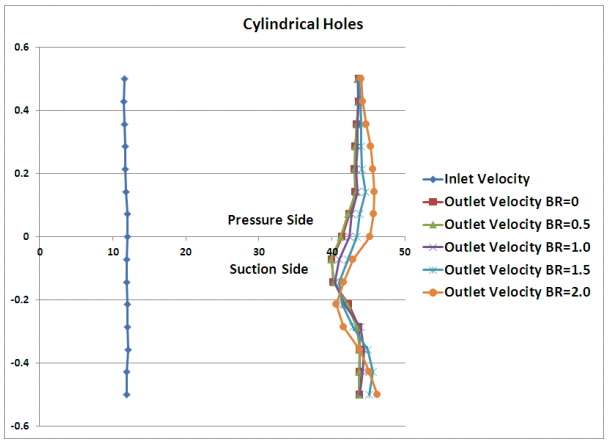

Figure 6.19: CYLINDRICAL INJECTION HOLE AERODYNAMIC PERFORMANCE

This result shows that injecting coolant with cylindrical holes carries an aerodynamic penalty once you go above the very minimum flow. It also appears that the increased coolant ejection is causing the wake to migrate towards the passage center from the suction side.

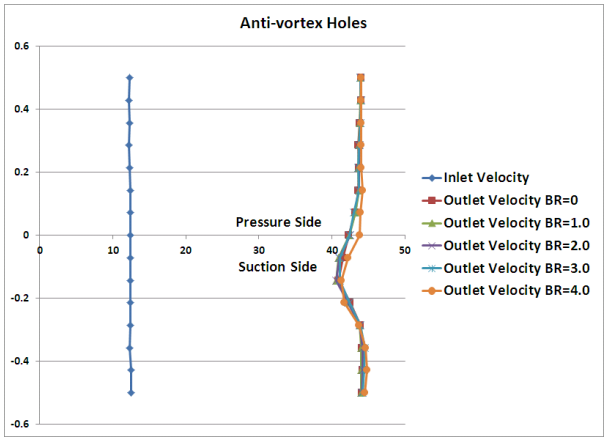

Figure 6.20: TRIPOD INJECTION HOLE AERODYNAMIC PERFORMANCE

Figure 6.20 shows the inlet and exit velocity profiles of a blade with tripod injection holes on both the suction and pressure sides of the blades, at blowing ratios of 0, 1.0, 2.0, 3.0 and 4.0. For this geometry, the velocity profile is essentially unaffected until the highest tested blowing ratio of 4.0. This result shows that injecting coolant with tripod holes has a greatly reduced aerodynamic penalty compared to the cylindrical hole injection even at comparable

flow rates.

6.7 Conclusions

The key feature of this study is the comparison of tripod holes to cylindrical holes in a realistic vane cascade with the GE E^3 profile first stage vane. The tripod hole design features one coolant entrance for three holes. The two side holes bifurcate from the base of the main hole. This design spreads the flow over a wider area, reducing exit momentum, while also avoiding flow separation from the hole edges that can be an issue with flared holes. The design was tested on both pressure and suction surfaces and compared to a typical cylindrical hole at the same location. Both detailed surface film effectiveness measurements at different blowing rations and coolant densities and also overall aerodynamic penalty measurements are presented. Some highlights of the study are presented below.

1. Tripod hole design shows enhanced performance in comparison to standard cylindrical holes in improving cooling effectiveness with reduced coolant mass flows.

2. The pressure surface injection shows a trend of increasing effectiveness with increasing blowing ratio for cylindrical holes, and a peak effectiveness at BR=2.0 for tripod holes.

3. The suction surface injection shows a trend of decreasing effectiveness with increased blowing ratio for the cylindrical geometry, while the tripod geometry exhibits lower variation in effectiveness between blowing ratios.

4. Jet lift-off is mitigated on the pressure side by the higher pressure of the mainstream flow and the vane curving into the flow, but is still present at the highest tested blowing ratios for the cylindrical holes; the tripod holes show no jet lift-off effect at the blowing ratios tested on the pressure side.

5. Jet lift-off is exacerbated on the suction side by the low pressure of the mainstream flow and the vane curving away from the flow for cylindrical holes.

6. Modified momentum flux ratio is shown to be an effective correlation between coolant gases of different densities and different geometries.

7. Pressure side tripod holes show similar effectiveness immediately downstream of the hole exit compared to cylindrical holes but show a higher effectiveness in the region beyond 5 diameters downstream.

8. Suction side tripod holes show a higher effectiveness at all locations and all blowing ratios examined in this study.

9. Tripod holes have a significantly reduced effect on the aerodynamic performance on the vane in comparison to the cylindrical design based on inlet and exit velocity profile comparisons.

7. Exploration of the Effect of Breakout Angle on Tripod Holes

The cascade testing proved that the tripod hole is viable for use on curved surfaces. The next step in the investigation is to test the effect of changing the breakout angle of the side holes, as well as adding a comparison to a typical shaped hole design. These tests were conducted on the flat plate test rig previously described, using the steady-state IR technique with room temperature mainstream flow and heated secondary flow. Results are presented in the form of adiabatic wall effectiveness.

7.1 Hole Geometries

This portion of the study utilizes four geometries as shown in Figure 7.1. The first geometry (Fig. 7.1a) is a simple cylindrical hole design with a diameter of 6.35mm and axis inclined at 30° from the surface in the streamwise direction. The hole length-to-diameter ratio (l/d) is 7.5 and the pitch-to-diameter ratio (p/d) is 3. There are a total of 9 holes on the plate. Figure 7.1b shows a standard shaped hole of diameter 6.35mm with 10 flare and layback and axis inclined at 30° from the surface in the streamwise direction. The hole length-to-diameter ratio (l/d) is 7.5 and the pitch-to-diameter ratio (p/d) is 3. There are a total of 9 holes on the plate. Figure 7.1c shows a tripod hole unit in which the main or central hole is identical to the first geometry, but has an additional hole on either side that branch out at 15° angle and are connected together at the inlet such that the metering area at the entrance of the secondary flow is circular. All three holes are inclined at 30° angle from the surface. The l/d ratio of the center and side holes is 7.5 and 7.7, respectively. The p/d ratio between

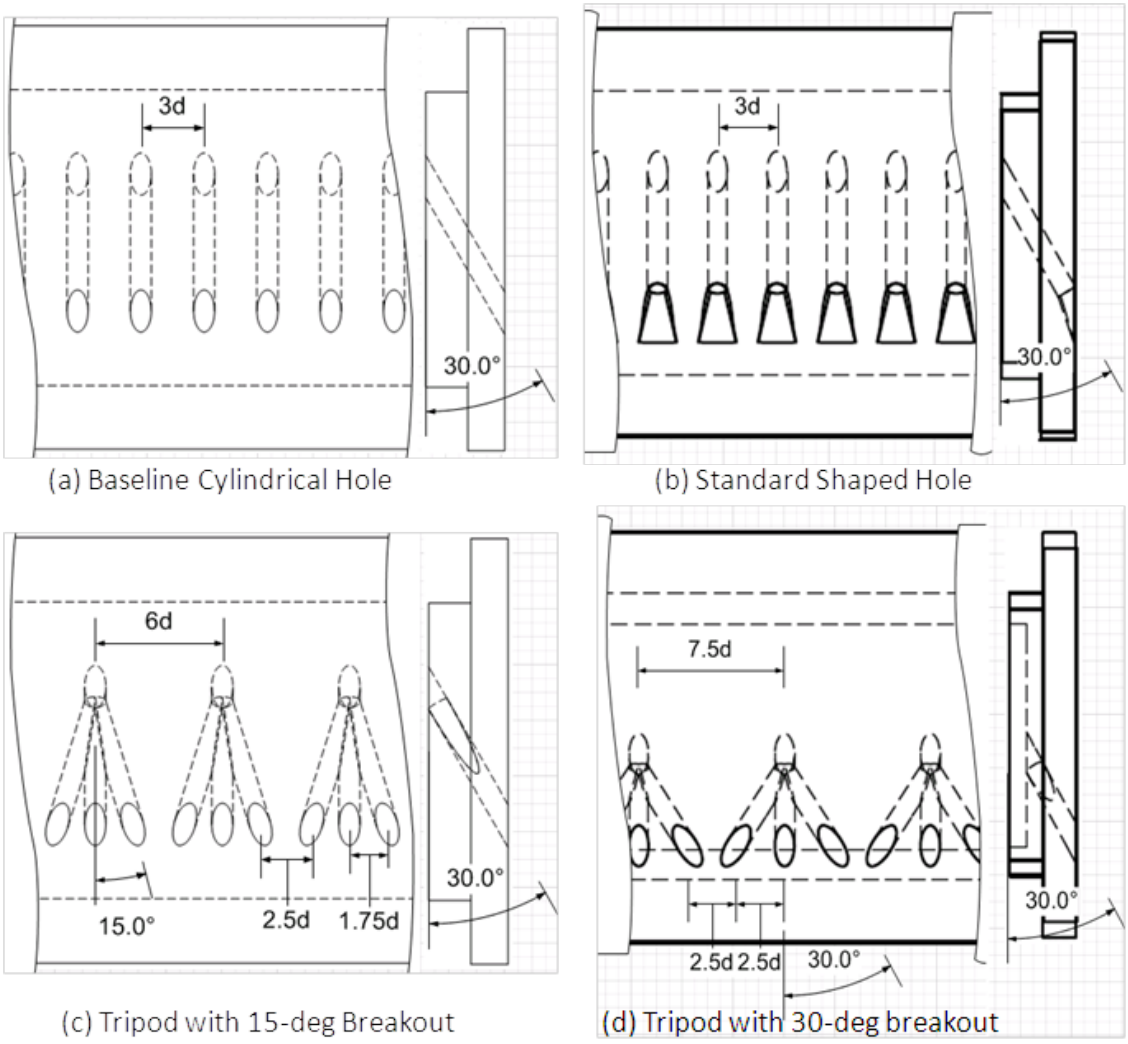

Figure 7.1: INJECTION HOLE DESIGNS FOR COMPARISON

the main holes is 6, between the center and side holes is 1.75, and between the side holes of adjacent units is 2.5. There are a total of 5 sets of tripod 15° holes on the plate. Figure 7.1d shows a tripod hole unit in which the main or the central hole is identical to the first geometry but has an additional CY hole on either side that branch out at 30° angle and connected together at the inlet such that the metering area at the entrance of the secondary flow is circular. All three holes are inclined at 30° angle from the surface. The l/d ratio of the center and the side holes is 4.0 and 4.3, respectively. The p/d ratio between the main

holes is 7.5, between the center and the side hole is 2.5, and between the side holes of the adjacent tripod unit is 2.5. There are a total of 5 sets of tripod holes on the plate. Because of the ease with which complex geometries can be built in quick time at a fraction of the machining cost, the geometries were grown with the rapid prototyping technique.

7.2 Test Conditions

As shown in Table 7.1, a total of 28 experiments were performed to study the effects of breakout angle on adiabatic film-cooling effectiveness. From Table 7.1, it is important to note that the tripod 15° (TR15) holes use 50% of the coolant used by the cylindrical holes for the same blow ratio, and the tripod 30° (TR30) holes use 40% of the coolant used by the cylindrical holes for the same blowing ratio due to reduced number of inlet points for the tripod holes. Due to the design of the holes, the 5 TR15 holes cover as much of the surface of the plate as 10 cylindrical holes would and the 5 TR30 holes cover as much of the surface of the plate as 13 cylindrical holes would. The metering location for the holes is the inlet side of the holes which is the same in area per hole for all geometries. For all geometries to push similar mass flow, the tripod holes will operate at double the blowing ratio of the shaped holes.

The blowing ratio is defined as ratio of the coolant to mainstream mass flux at the hole inlet.

$$BR = \frac{(\rho V)_{sg}}{(\rho V)_{\infty}} \tag{7.1}$$

where V_{∞} is the mainstream air velocity at the test section inlet averaged over the entire

Table 7.1: SUMMARY OF BREAKOUT ANGLE EXPERIMENTAL CONDITIONS

Exp	Hole	BR	DR	I	$\dot{m}(kg/s)$
1	CY	0.5	0.95	0.263	0.0013
2	CY	1.0	0.95	1.053	0.0027
3	CY	1.5	0.95	2.368	0.0040
4	CY	2.0	0.95	4.211	0.0054
5	CY	0.5	1.45	0.172	0.0013
6	CY	1.0	1.45	0.690	0.0027
7	CY	1.5	1.45	1.552	0.0040
8	SH	0.5	0.95	0.263	0.0013
9	SH	1.0	0.95	1.053	0.0027
10	SH	1.5	0.95	2.368	0.0040
11	SH	2.0	0.95	4.211	0.0054
12	SH	0.5	1.45	0.172	0.0013
13	SH	1.0	1.45	0.690	0.0027
14	SH	1.5	1.45	1.552	0.0040
15	TR15	1.0	0.95	1.053	0.0015
16	TR15	2.0	0.95	4.211	0.0030
17	TR15	3.0	0.95	9.474	0.0045
18	TR15	4.0	0.95	16.842	0.0060
19	TR15	1.0	1.45	0.689	0.0015
20	TR15	2.0	1.45	2.759	0.0030
21	TR15	3.0	1.45	6.207	0.0045
22	TR30	1.0	0.95	1.053	0.0015
23	TR30	2.0	0.95	4.211	0.0030
24	TR30	3.0	0.95	9.474	0.0045
25	TR30	4.0	0.95	16.842	0.0060
26	TR30	1.0	1.45	0.689	0.0015
27	TR30	2.0	1.45	2.759	0.0030
28	TR30	3.0	1.45	6.207	0.0045

span. The mass flow rate for a given blowing ratio is given by:

$$\dot{m} = \sum_{i=1}^{n} BR(\rho V)_\infty a_i \tag{7.2}$$

and DR is found by applying the ideal gas law

$$DR = \frac{\rho_{sg}}{\rho_\infty} = \frac{(RT)_{sg}}{(RT)_\infty} \tag{7.3}$$

7.3 Experimental Uncertainty

Uncertainties were estimated based on the procedure described by Coleman and Steele [35]. The mainstream velocity was kept constant within ±1.3%. Uncertainties in setting the blowing ratios were ±3%. Uncertainties in the correction factor are estimated to be ±2.5%. Based on accuracy of ±0.5°C for thermocouple measurements and accuracy of ±1°C for IR measurements, the uncertainty in effectiveness amounted to ±5.0% for η=0.5 and ±10.0% for η=0.15.

7.4 Results

7.4.1 Effect of hole geometry

Figure 7.2 shows the film effectiveness contours for the four studied geometries with air as the coolant gas. Each plot covers a downstream distance of approximately 30d starting from the hole leading edge. The left most column shows the effectiveness measured downstream of a row of cylindrical holes. Well-defined peaks downstream of the hole centerline and valleys in

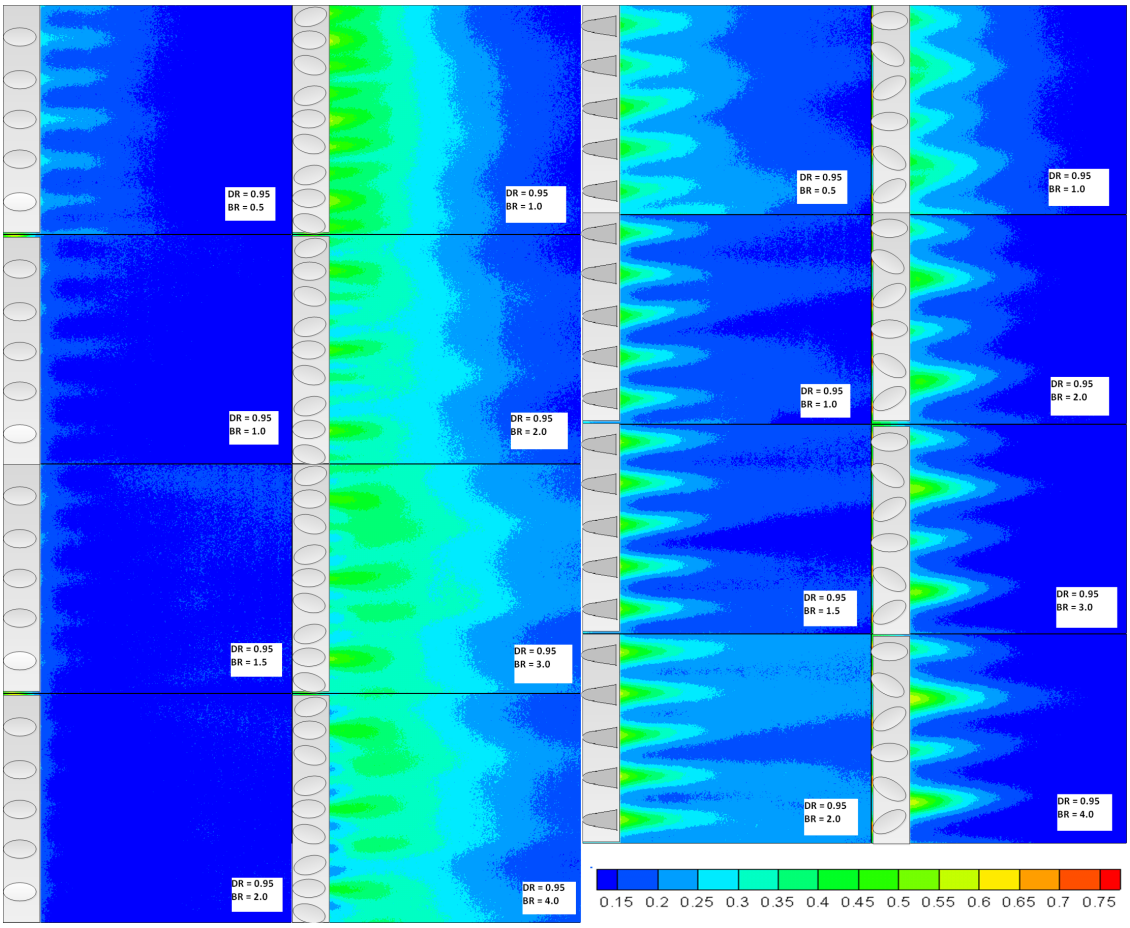

Figure 7.2: EFFECTIVENESS CONTOURS WITH AIR INJECTION

between are observed close to the holes, especially at low BRs. The lateral variations smear out at large distances downstream owing to diminished jet strength. As BR is increased, the peaks grow smaller and smaller, and at the highest BR, there are no discernible peaks and valleys. This data shows the expected reduction of film cooling effectiveness with increasing blowing ratio that is typical of the cylindrical design, and is typically attributed to the jet momentum being high enough to cause the coolant flow to separate from the plate surface.

The second column from the left is a similar plot for the TR15 holes with three TR15 units shown in each plot. The rationale behind using a 3-hole geometry is twofold one is to expand the exit area with the intention of lowering the jet momentum and thereby delay

lift-off, much like that of a shaped hole concept, and second, to create identical vortices from the side holes to invalidate the main kidney vortex and thereby reduce vortex- induced entrainment effect. The dramatic improvement in effectiveness in the immediate vicinity of the TR15 holes confirms the working of this theory even with minor modifications in hole size and spacing. The jets merge downstream still maintaining good coverage for a significant distance. At high BRs of 3.0 and 4.0, regions of high effectiveness (colored yellow) appear between TR15 units not seen in smaller BRs. The BR at which these secondary TR15 pairs start to develop is a function of the divergence angle and the spacing between the side holes. There is also a minor amount of flow separation being observed at the highest blowing ratio, indicated by the region of low effectiveness between the holes.

The second column from the right shows the effectiveness measured downstream of a row of shaped (SH) holes. Well-defined peaks downstream of the hole centerline and valleys in between are observed at all BRs. The lateral variations decrease as you go further downstream for all cases. The data for the shaped hole demonstrates the resistance to flow separation that is one of the primary advantages of the shaped hole, allowing for higher blowing ratios without sacrificing performance.

The right most column is a similar plot for the TR30 holes with two hole sets unit shown in each plot. The side holes of each set show a significant interaction with the adjoining hole set at all blowing ratios, creating an area of peak effectiveness in the region. There are again peaks in the effectiveness that persist a similar distance downstream as compared to the shaped holes. The data does not show any regions of low effectiveness near the holes that would indicate a region of jet lift-off.

Figure 7.3 compares the laterally averaged effectiveness with air as coolant for the lowest mass flow case of all studied geometries. The TR15 geometry shows a clear advantage over the other studied geometries, with the cylindrical geometry shows the poorest performance,

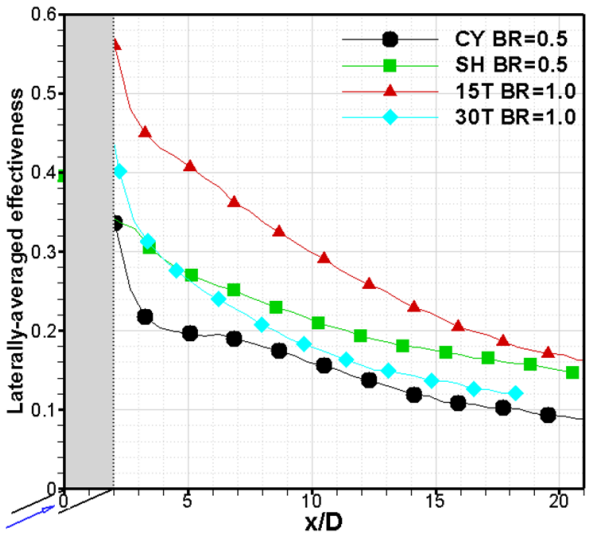

Figure 7.3: LATERALLY AVERAGED EFFECTIVENESS WITH AIR INJECTION, LOWEST MASS FLOW

as expected. The TR30 geometry and the shaped hole geometry show similar levels of effectiveness, with the TR30 design having the advantage of covering more spanwise distance with the same mass flow of coolant.

Figure 7.4 compares the laterally averaged effectiveness with air as coolant for the highest mass flow case of all studied geometries. The TR15 geometry shows a dip in effectiveness immediately downstream of the hole exits corresponding to the low effectiveness region in the contour plot. This dip is attributed to small regions of jet lift-off near the hole exits, and the flow is demonstrating behaviour consistent with re-attachment once a distance of 3 hole diameters is reached. The TR15 geometry still displays an advantage over the other studied geometries, though it would be worth investigating hole shaping to reduce the jet lift-off. The TR30 geometry shows lower effectiveness than the shaped hole geometry, while remaining generally superior to the cylindrical hole geometry. It should also be noted again that the TR30 geometry uses significantly less coolant than the other three studied designs.

Figure 7.5 compares the laterally averaged effectiveness with air as coolant for the BR = 1.0

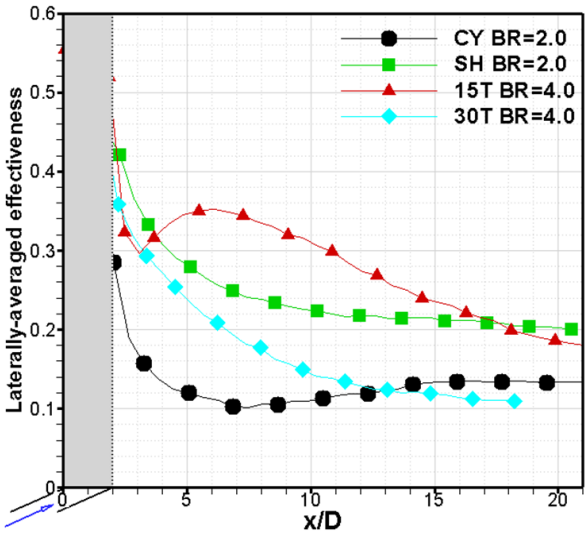

Figure 7.4: LATERALLY AVERAGED EFFECTIVENESS WITH AIR INJECTION, HIGHEST MASS FLOW

case of all studied geometries. The TR15 hole shows the highest effectiveness of all studied geometries, with the performance of the shaped hole and the TR30 hole effectively tying for second place. With the cylindrical hole case taken as the baseline with a mass flow of 1.0, the shaped hole has a mass flow of 1.0, the TR15 hole has a mass flow of 0.49 and the TR30 hole has a mass flow of 0.38.

Figure 7.6 compares the laterally averaged effectiveness with air as coolant for the BR = 2.0 case of all studied geometries. The TR15 hole shows the highest effectiveness of all studied geometries out to 15 hole diameters downstream, with the performance of the shaped hole being equal to the TR15 below 3 hole diameters downstream, and superior at greater than 15 hole diameters downstream. The TR30 design provides lower effectiveness than the TR30 and shaped holes throughout the test region. With the cylindrical hole case taken as the baseline with a mass flow of 1.0, the shaped hole has a mass flow of 1.0, the TR15 hole has a mass flow of 0.49 and the TR30 hole has a mass flow of 0.38.

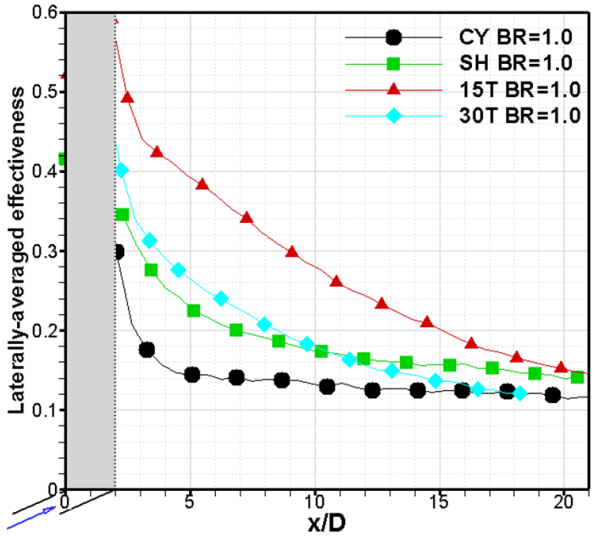

Figure 7.5: LATERALLY AVERAGED EFFECTIVENESS WITH AIR INJECTION, BR=1.0

7.4.2 Effect of density ratio

To determine the effect of DR variation on film cooling, some tests were performed using CO_2 as the secondary gas. A combination of molecular weight and temperature difference between CO_2 and the mainstream air produced a density ratio of 1.45 for this study. Figure 7.7 presents the laterally averaged effectiveness for all tested cases for all studied geometries.

Figure 7.7a presents data for the CY holes. In the range, x/d¡13, the heavier gas shows higher effectiveness at all BR except at BR=1.5 where the level is about the same. In the range, x/d¿13, the heavier gas performs better at BR=0.5, is head to head with the lighter gas at BR=1.0, and performs poorer than the lighter gas at BR=1.5.

Figure 7.7b presents data for the TR15 holes. In the near hole region, x/d¡5, the intermediate BRs of 1.5 and 2.0 display high film effectiveness with the heavier gas. At BR=3.0, the heavier gas is not as effective as the lighter gas as seen from the low effectiveness values in that region. Beyond x/d=5, the heavier gas fares poorly in comparison to the lighter fluid

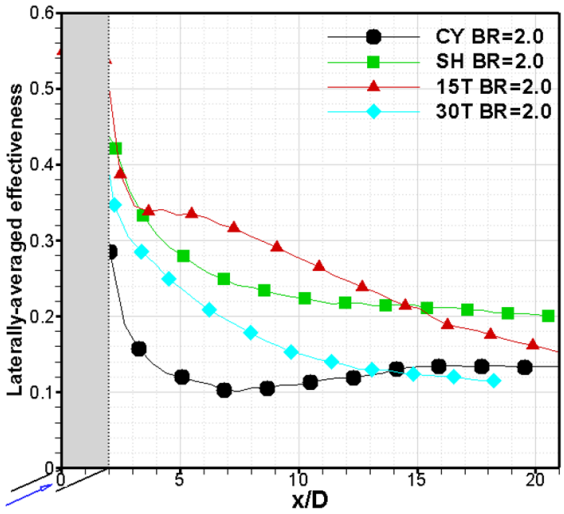

Figure 7.6: LATERALLY AVERAGED EFFECTIVENESS WITH AIR INJECTION, BR=2.0

irrespective of BR.

Figure 7.7c presents data for the SH holes. At every studied blowing ratio the shaped hole design shows lower effectiveness with a higher density coolant, though the difference is greatest at the lowest blowing ratio.

Figure 7.7d presents data for the TR30 holes. The data shows a reduction in effectiveness with the higher density coolant, though to a lesser degree than for the shaped hole design. Once again the TR30 hole design shows the most robust response to changing conditions in the test.

7.4.3 Effect of blowing ratio

A better understanding of the film cooling phenomena can be obtained by cross plotting some of the data to show the influence of BR. Figure 7.8 shows laterally-averaged effectiveness distributions at three different downstream positions for the studied hole geometries. The

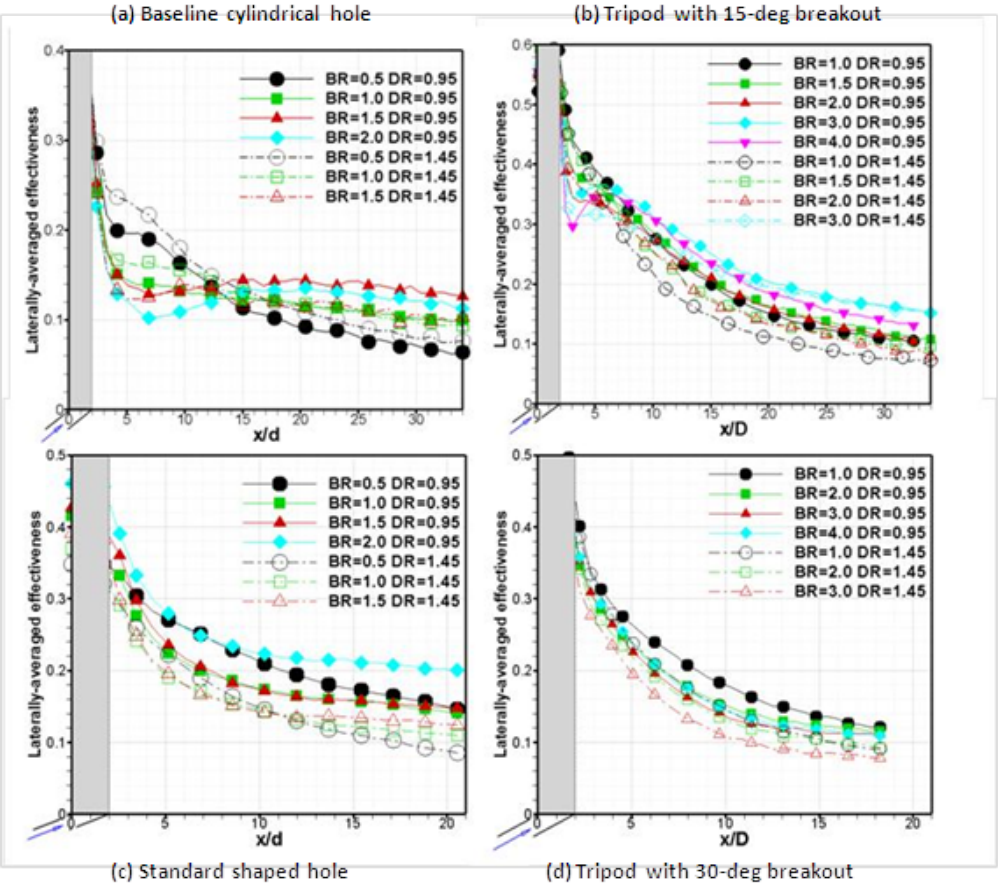

Figure 7.7: EFFECT OF DENSITY RATIO ON LATERALLY AVERAGED EFFECTIVENESS

TR15 holes show a consistently higher effectiveness regardless of blowing ratio, and both of the tripod hole designs show little variation due to blowing ratio. The cylindrical hole design has the poorest performance as well as the most sensitivity to changes in blowing ratio, while the SH holes perform well but do display sensitivity to changes in the blowing ratio.

7.4.4 Scaling parameter

Generally, momentum flux ratio (I) and not BR is considered as a better scaling parameter for secondary gases of different densities operating in the high BR regime. A further gener-

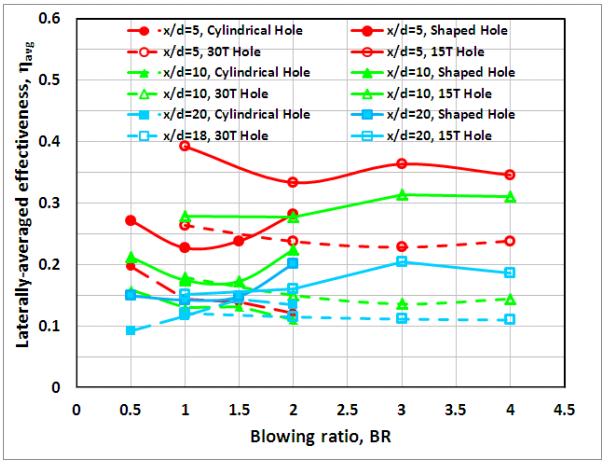

Figure 7.8: LATERALLY AVERAGED EFFECTIVENESS AS A FUNCTION OF BR

alization is possible by introducing a parameter AR (exit-to-inlet hole area ratio) to account for the different hole shape at the exit. This parameter, I*, is defined as the momentum flux ratio normalized by the exit-to-inlet hole area ratio squared.

$$I^* = \frac{BR^2}{AR^2 * DR} \tag{7.4}$$

Since tripod holes work on a similar principle of expanded exit, it is worthwhile to draw a plot of effectiveness as a function of I*. For the tripod holes, the value of AR is 3.0 whereas for the shaped holes it is 2.55 and for the cylindrical holes it is 1.0.

Figure 7.9 shows the laterally averaged effectiveness as a function of I* for the four hole designs. The data shows that I* is a good scaling parameter, as the values for the two density ratios align nicely. For the case of shaped holes, the two different fluids are seen to correlate well at the three downstream positions considered. It appears that the momentum flux ratio combines the effect of blowing ratio and density ratio into one parameter and provides basis to use as a correlating parameter.

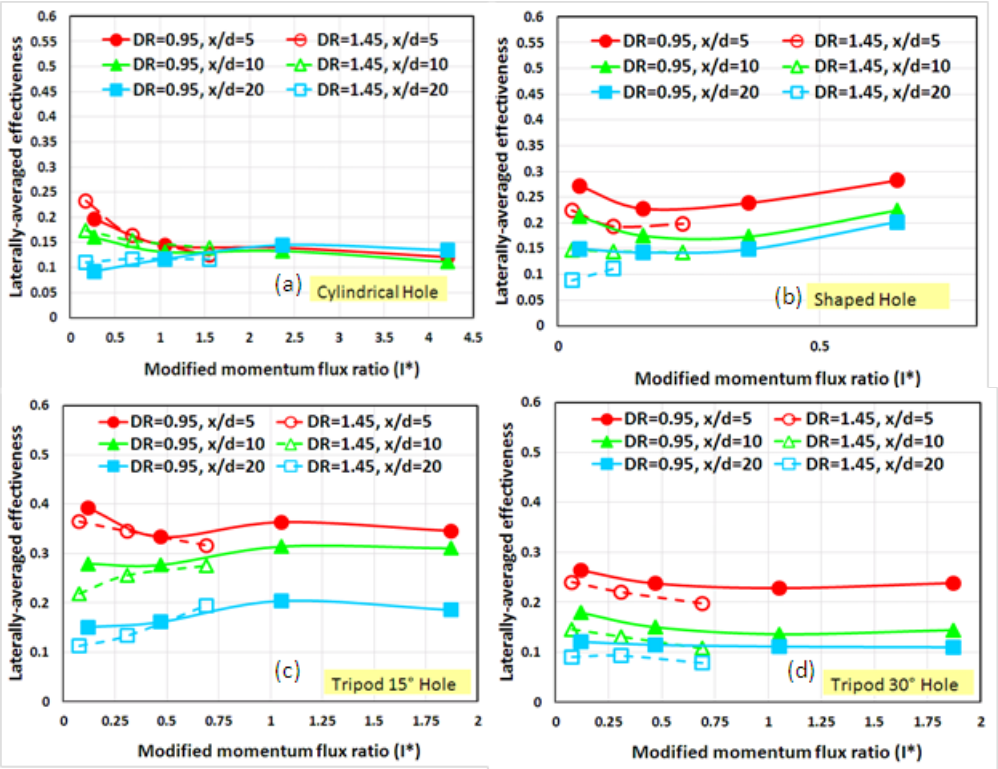

Figure 7.9: EFFECT OF MODIFIED MOMENTUM FLUX RATIO FILM EFFECTIVENESS FOR ALL FOUR GEOMETRIES

7.5 Conclusions

The key feature of this study is the addition of a modern shaped hole design and a tripod 30° hole design to previous work done on a flat plate. The tripod hole design features one coolant entrance for three holes. The two side holes bifurcate from the base of the main hole. This design spreads the flow over a wider area, reducing exit momentum, while also avoiding flow separation from the hole edges that can be an issue with flared holes. Detailed surface film effectiveness measurements at different blowing ratios, as well as coolant densities and laterally averaged effectiveness values are presented. Some highlights of the study are presented below.

1. TR15 hole design shows the best effectiveness out of the four studied designs.

2. TR30 hole design shows the least variation in effectiveness when blowing ratio is varied.

3. TR30 hole design shows the least variation in performance when using a higher density coolant.

4. CY hole design shows a tendency towards jet lift-off higher than BR = 0.5, and the TR15 design shows small amounts of jet lift-off at BR = 4.0.

5. Modified momentum flux ratio is shown to be an effective correlation between coolant gases of different densities and different geometries.

6. TR30 hole design is able to provide slightly reduced effectiveness compared to the SH hole design while using significantly less coolant due to higher hole spacing.

7. TR15 hole design is seen as the most worth of further study, particularly regarding shaping the exits of the tripod hole to explore the possible benefits of that arrangement, especially regarding the minor jet lift-off seen at BR = 4.0.

8. Exploration of the Effect of Hole Exit Shaping on Tripod Holes

The breakout angle testing showed that the tripod hole with 30° breakout angle is viable, but confers no benefit in effectiveness levels when compared to the tripod hole with 15° breakout angle. The focus from this point forward remains on the tripod hole with 15° breakout angle and how it may be further improved. The next step in the investigation is to test the effect of shaping the exits to the tripod holes, and also make use of the newly acquired capability to perform transient tests on the flat plate rig. These tests were conducted on the flat plate test rig previously described, using the hybrid transient and steady-state IR technique with heated mainstream flow and room temperature secondary flow. Results are presented in the form of adiabatic wall effectiveness, heat transfer coefficient and heat flux ratio.

8.1 Hole Geometries

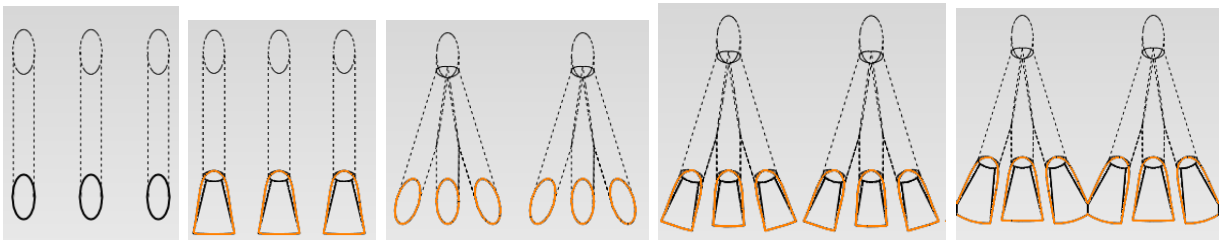

(a) CY (b) SH (c) TR15 (d) TR15SH5 (e) TR15SH10

Figure 8.1: HOLE GEOMETRIES

Five different geometries were used during the experiments as shown in Fig. 8.1. The first geometry is a simple CY hole of diameter 6.35mm and axis inclined at 30° from the surface in the streamwise direction. The hole length-to-diameter ratio (l/d) is 7.5 and the pitch-to-

diameter ratio (p/d) is 3. There are a total of 13 holes on the plate. The second geometry implements shaping on the hole exits of the cylindrical design, with flare and layback angles of 10°. The third geometry is a 3-hole unit (tripod) in which the main or the central hole is identical to the first geometry but has an additional CY holes on either side that branch out at 15° angle and are connected together at the inlet such that the metering area at the entrance of the secondary flow is circular. All three holes are inclined at 30° angle from the surface. The l/d ratio of the center and the side holes is 7.5 and 7.7, respectively. The p/d ratio between the main holes is 6d, between the center and the side hole is 1.75d, and between the side holes of the adjacent tripod unit is 2.5d. There are a total of 7 sets of tripod holes on the plate. The design is akin to removing alternate holes in the CY design and adding two angled holes to each of the remaining holes. The fourth geometry implements shaping on the hole exits of the tripod design, with flare and layback angles of 5°, while the fifth geometry uses flare and layback angles of 10°. Because of the ease with which complex geometries can be built in quick time at a fraction of the machining cost, the geometries were grown with the rapid prototyping technique.

8.2 Test Conditions

As shown in Table 8.1, a total of 20 experiments were performed to study the effects of blowing ratio (BR) and hole design on adiabatic film-cooling effectiveness. BR is defined as

$$BR = \frac{(\rho V)_{sg}}{(\rho V)_{\infty}} \tag{8.1}$$

where V_∞ is the mainstream air velocity at the test section inlet averaged over the entire span. The mass flow rate for a given blowing ratio is given by:

$$\dot{m} = \sum_{i=1}^{n} BR(\rho V)_\infty a_i \tag{8.2}$$

Notice that the mass flow rate required with tripod holes is only about half that of cylindrical holes for any given blowing ratio.

Table 8.1: LIST OF TEST CONDITIONS

Exp	Hole	BR	$\dot{m}(kg/s)$
1	CY	0.5	0.0013
2	CY	1.0	0.0026
3	CY	1.5	0.0039
4	CY	2.0	0.0052
5	SH	0.5	0.0013
6	SH	1.0	0.0026
7	SH	1.5	0.0039
8	SH	2.0	0.0052
9	TR15	1.0	0.0014
10	TR15	2.0	0.0028
11	TR15	3.0	0.0042
12	TR15	4.0	0.0056
13	TR15SH5	1.0	0.0014
14	TR15SH5	2.0	0.0028
15	TR15SH5	3.0	0.0042
16	TR15SH5	4.0	0.0056
17	TR15SH10	1.0	0.0014
18	TR15SH10	2.0	0.0028
19	TR15SH10	3.0	0.0042
20	TR15SH10	4.0	0.0056

Experimental Uncertainty

Uncertainties were estimated based on the procedure described by Coleman and Steele [35]. The mainstream velocity was kept constant within ±1.3%. Uncertainties in setting the blowing ratio was ±3%. Based on an accuracy of ±0.5°C for the thermocouple measurement and an accuracy of ±1°C for IR measurement, the uncertainty in adiabatic effectiveness amounted to ±0.5% for η=0.5 and ±1.0% for η=0.15. Based on the uncertainty of the effectiveness calculation and the accuracy of the experimental measurements, the uncertainty for heat transfer coefficient is ±15.0%.

8.3 Effectiveness and Heat Transfer Coefficient Measurement

8.3.1 Film-cooling Effectiveness

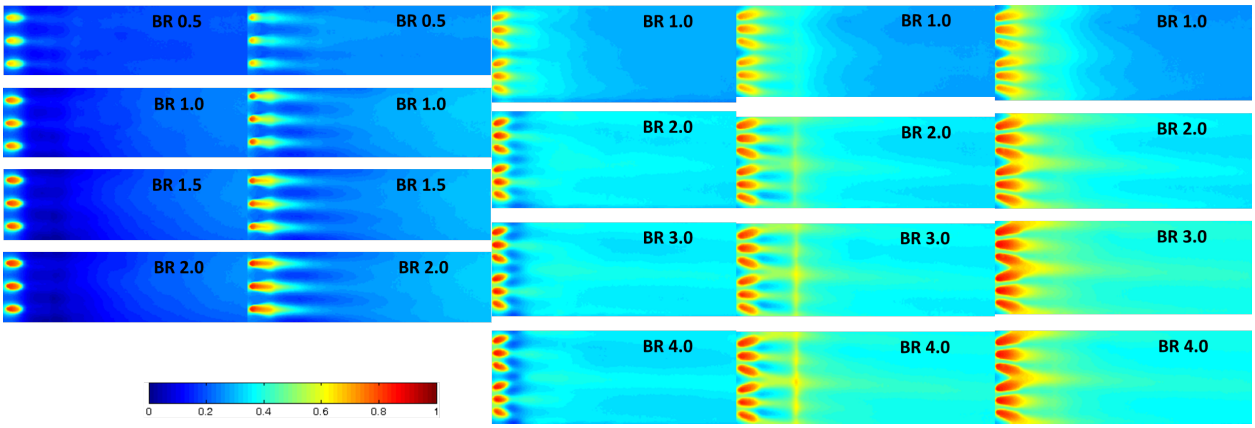

Figure 8.2: FILM COOLING EFFECTIVENESS CONTOURS

Figure 8.2 shows, from left to right, the film effectiveness contours for CY, SH, TR15,

TR15SH5 and TR15SH10; the BRs are presented with lowest at the top of the figure and highest at the bottom. Each plot covers a downstream distance of approximately 30d starting from the hole leading edge. The effectiveness downstream of the CY holes is uniformly low, with streaks of moderately higher effectiveness visible in line with the holes. The SH holes show a marked improvement over the CY holes, though they retain the streaks of higher effectiveness with areas of lower effectiveness between the holes. The TR15 holes provide more even coverage than the previous two designs, with small gaps in coverage between the holes immediately downstream of the exits. There are also streaks of higher effectiveness in between the hole sets where the jets from the angled holes meet. Overall the TR15 holes provide consistent coverage at all but the lowest tested BR. The TR15SH5 holes improve on the performance of the TR15 holes by reducing the coverage gaps at the hole exits as well as increasing the peak values of the jets themselves. The TR15SH10 holes improve in these areas even further, going so far as to eliminate the regions of low effectiveness between the holes. Additionally, all three of the tripod 15° designs have their worst performance at the lowest BR, with the three higher tested BRs showing little variation in their levels of coverage.

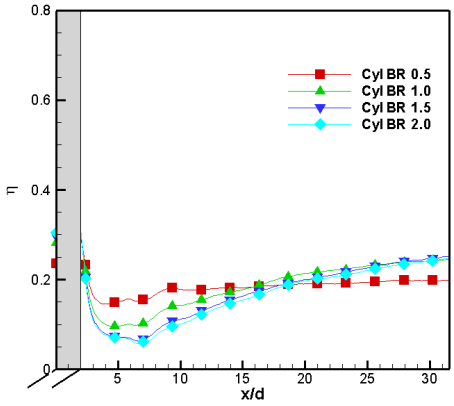

(a) CYLINDRICAL

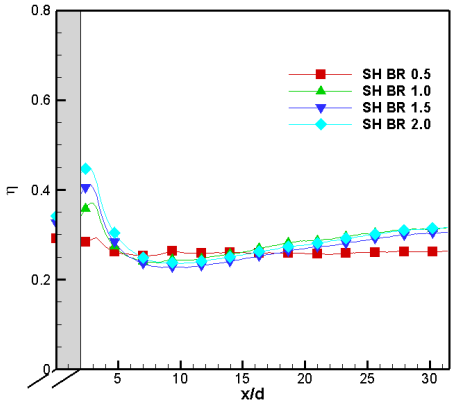

(b) SHAPED 10°

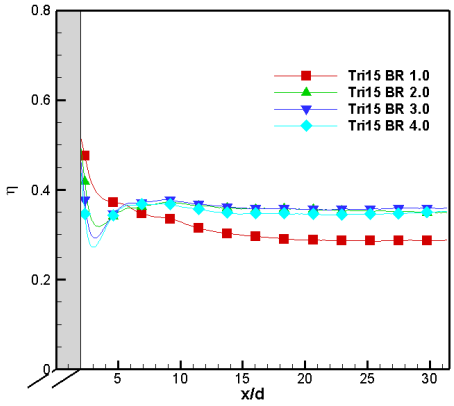

(c) TRIPOD 15°

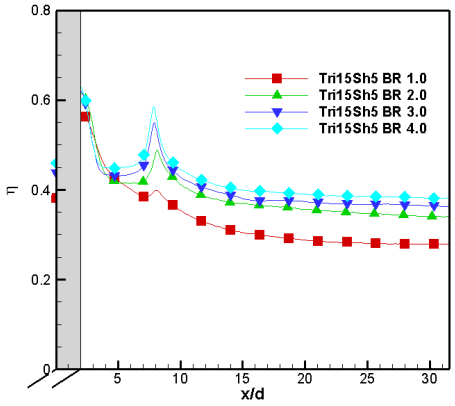

(d) TRIPOD 15° SHAPED 5°

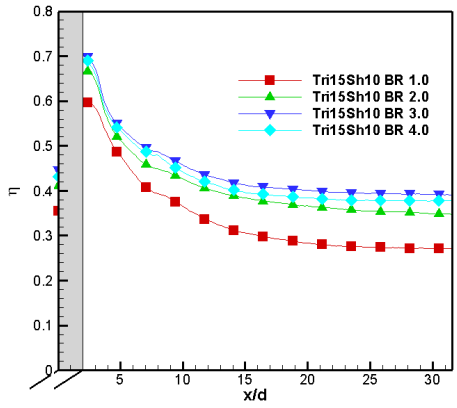

(e) TRIPOD 15° SHAPED 10°

Figure 8.3: LATERALLY AVERAGED EFFECTIVENESS

Figure 8.3 shows the laterally averaged effectiveness for the tested configurations. The cylindrical design shows the lowest effectiveness levels, with its highest effectiveness at the lowest tested BR. The SH design shows improvement in comparison to the cylindrical design at all BRs and distances downstream, while also showing performance improvement with increasing BR. The TR15 design improves upon the performance of the SH design, and shows consistent performance at BRs above the minimum tested. The TR15SH5 design increases the improvement of the TR15 design, especially in the near-hole region. The TR15SH10 design shows the best effectiveness of all the tested designs, again with little variation in effectiveness between the three highest tested BRs.

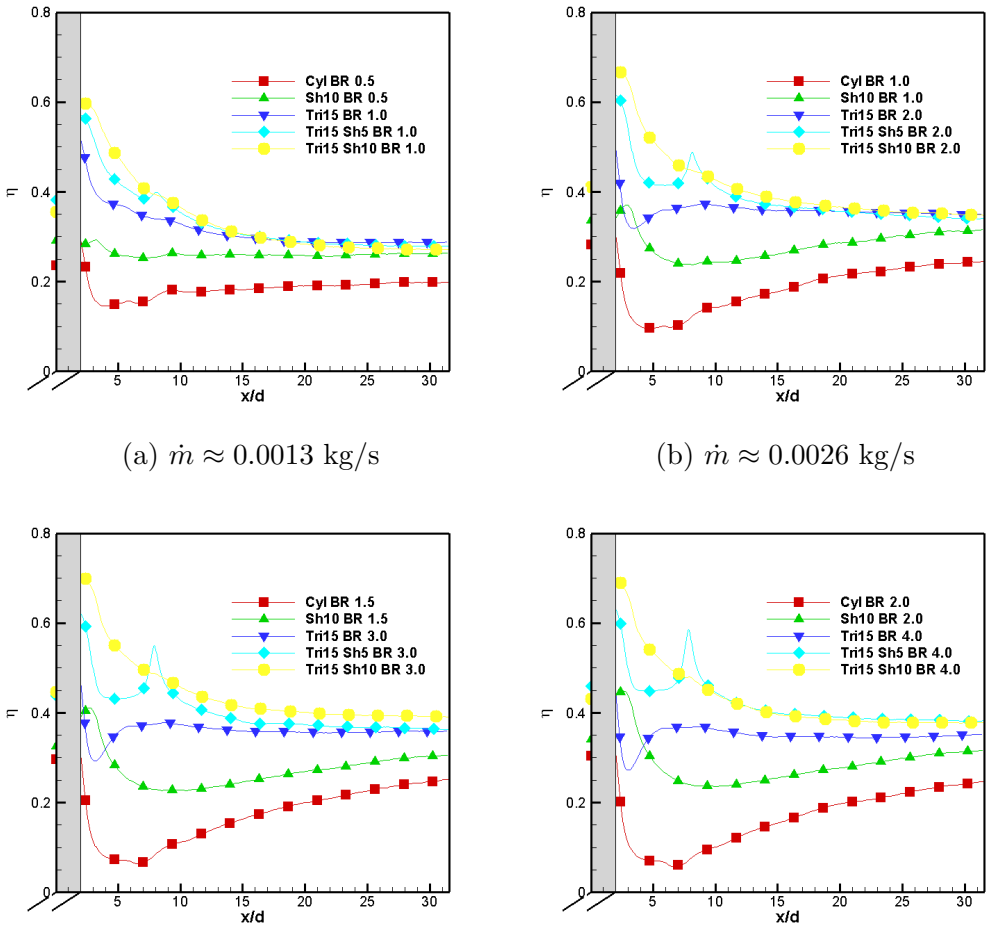

(a) $\dot{m} \approx 0.0013$ kg/s

(b) $\dot{m} \approx 0.0026$ kg/s

(c) $\dot{m} \approx 0.0039$ kg/s

(d) $\dot{m} \approx 0.0052$ kg/s

Figure 8.4: LATERALLY AVERAGED EFFECTIVENESS AT EQUAL MASS FLOW

Figure 8.4 shows the laterally averaged effectiveness at each tested mass flow rate, allowing for direct comparison between hole designs. The CY design shows the lowest performance in every comparison, as expected. The two shaped tripod holes consistently perform very well at every mass flow rate and at all downstream distances, with the TR15SH10 performing better in the near-hole region than the TR15SH5. The three tripod designs all have similar effectiveness levels 15d and further downstream. The SH design has some advantages over the TR15 design in the immediate downstream region at higher flow rates, but is clearly

inferior to all of the tripod designs beyond 5d downstream distance.

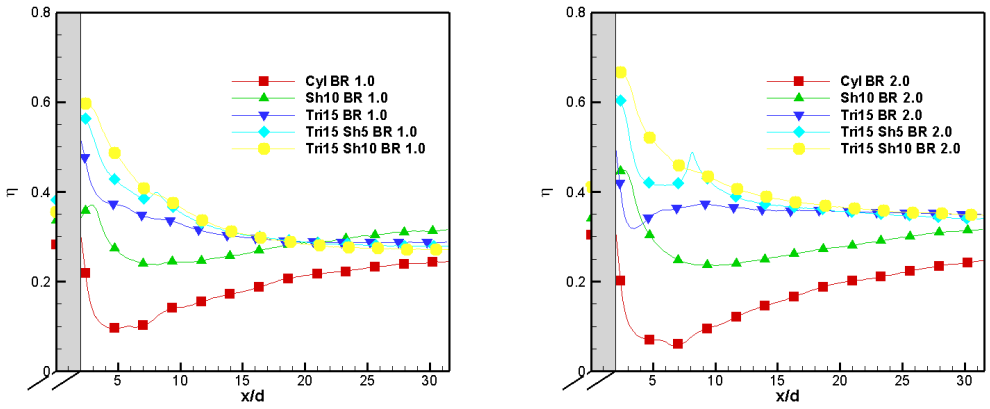

(a) BR=1.0 (b) BR=2.0

Figure 8.5: LATERALLY AVERAGED EFFECTIVENESS AT EQUAL BR

Figure 8.5 shows the laterally averaged effectiveness at each tested blowing ratio, allowing for further direct comparison between hole designs. When comparing these sets of data, it is important to remember that the mass flow rate for the tripod designs is approximately half the mass flow rate of the cylindrical and shaped designs. In the BR 1.0 case, the data shows that the tripod holes are providing improved effectiveness over the shaped hole up to 15d downstream distance, with effectiveness beyond that being quite similar. The BR 2.0 case shows a clear advantage for the shaped tripod holes up to 25d downstream distance, with the unshaped tripod hole being superior to the shaped cylindrical hole between 5d and 25d downstream distance.

8.3.2 Heat Transfer Coefficient

Figure 8.6 shows the laterally averaged heat transfer coefficient for the tested configurations. The TR15 design shows the lowest h levels, with values increasing with BR. The TR15SH10 design shows the highest h levels of all of the designs, with the TR15SH5 design having the

second highest h levels. For all tested designs, the lowest tested BR has the lowest h levels.

For a more direct comparison, we refer to Fig. 8.7, which shows the laterally averaged heat transfer coefficient at each tested mass flow rate. Comparing the data in this manner shows that the designs have a clearly defined order, with the TR15 design always having the lowest h values, followed by the CY design, then the SH design, the TR15SH5 design and the TR15SH10 design consistently having the highest h values. The exception to this trend is the TR15 design immediately downstream of the hole exit having higher h values than the CY and SH designs at high BR.

Figure 8.8 allows for a comparison between equal BRs. At BR 1.0 the h values for the TR15SH10 design are similar to the CY and SH designs to a distance approximately 8 hole diameters downstream, and the TR15SH5 design has similar h values to the SH design beyond approximately 12 hole diameters downstream. The case at BR 2.0 shows the TR15SH5 design to have slightly elevated h values when compared to the SH design, while the TR15SH10 design has the highest h value. The TR15 design has very low h values for both cases.

8.3.3 Heat Flux Ratio

The heat flux ratio is an indication of the reduction in heat flux obtained by introducing film cooling over a surface. This ratio may be defined as:

$$\frac{q''}{q''_0} = \frac{h}{h_0}\left(1 - \frac{\eta}{\phi}\right) \tag{8.3}$$

where ϕ is the overall cooling effectiveness and ranges from 0.5 to 0.7. For this study a value of 0.6 is chosen. Figure 8.9 shows the calculated heat flux ratio for each case at every tested mass flow rate. The CY design shows the highest heat flux ratio, causing a slight increase when compared to no coolant injection at all blowing ratios. The SH design has a

modest improvement over the no coolant injection case, while the three tripod designs all show significant reduction in the heat flux ratio, particularly at higher mass flow rates.

8.4 Conclusions

The key feature of this study is comparing the tripod designs, with and without shaping, to the more traditional style cylindrical and shaped film-cooling holes. The tripod holes all share the same 15° breakout angle, with the only difference being the shaping applied to the hole exits, from 0° to 5° to 10°. Highlights of the study are presented below:

1. The tripod designs all show higher effectiveness levels than the cylindrical and shaped designs.
2. The TR15 design has regions of low effectiveness just downstream of the hole exits.
3. Adding shaping to the TR15 design eliminates the regions of low effectiveness, with the 10° shaping proving most effective at elevating the effectiveness in the immediate downstream region.
4. The cylindrical design has the worst performance, in both effectiveness and h, of all the designs.
5. The TR15SH5 design has the highest peak h values of all the tested designs near the hole exit.
6. The TR15 design has the lowest h values of all the tested designs.
7. When comparing at equal BR, which by definition results in $\approx 50\%$ less coolant usage for the tripod holes, the tripod hole designs clearly outperform both the cylindrical and shaped 10° holes.

8. The tripod designs, both with and without shaping, show a net reduction in the heat flux ratio and a significant advantage over the shaped design.

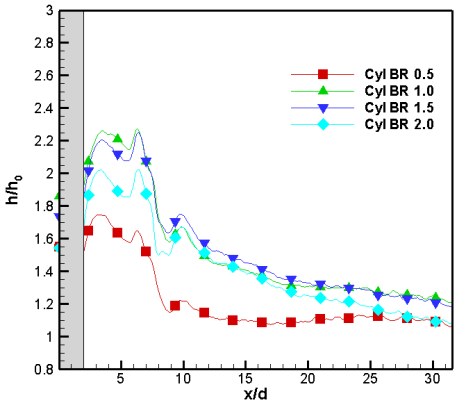

(a) CYLINDRICAL

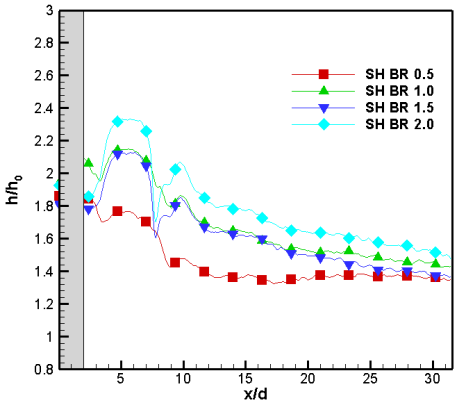

(b) SHAPED 10°

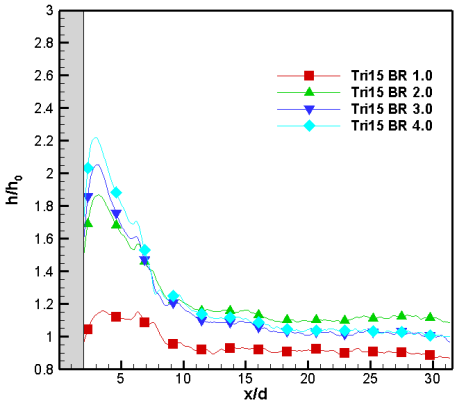

(c) TRIPOD 15°

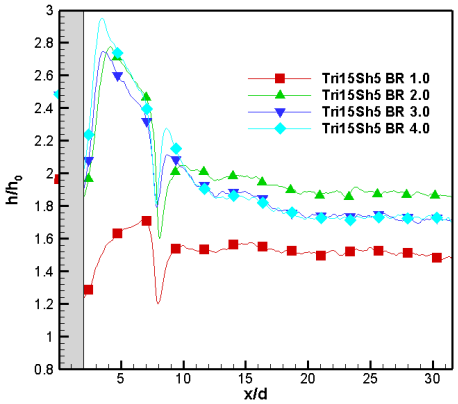

(d) TRIPOD 15° SHAPED 5°

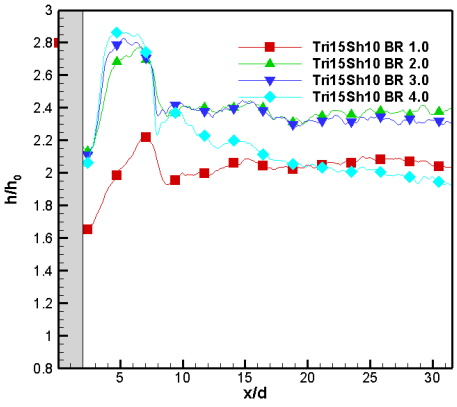

(e) TRIPOD 15° SHAPED 10°

Figure 8.6: LATERALLY AVERAGED HEAT TRANSFER COEFFICIENT

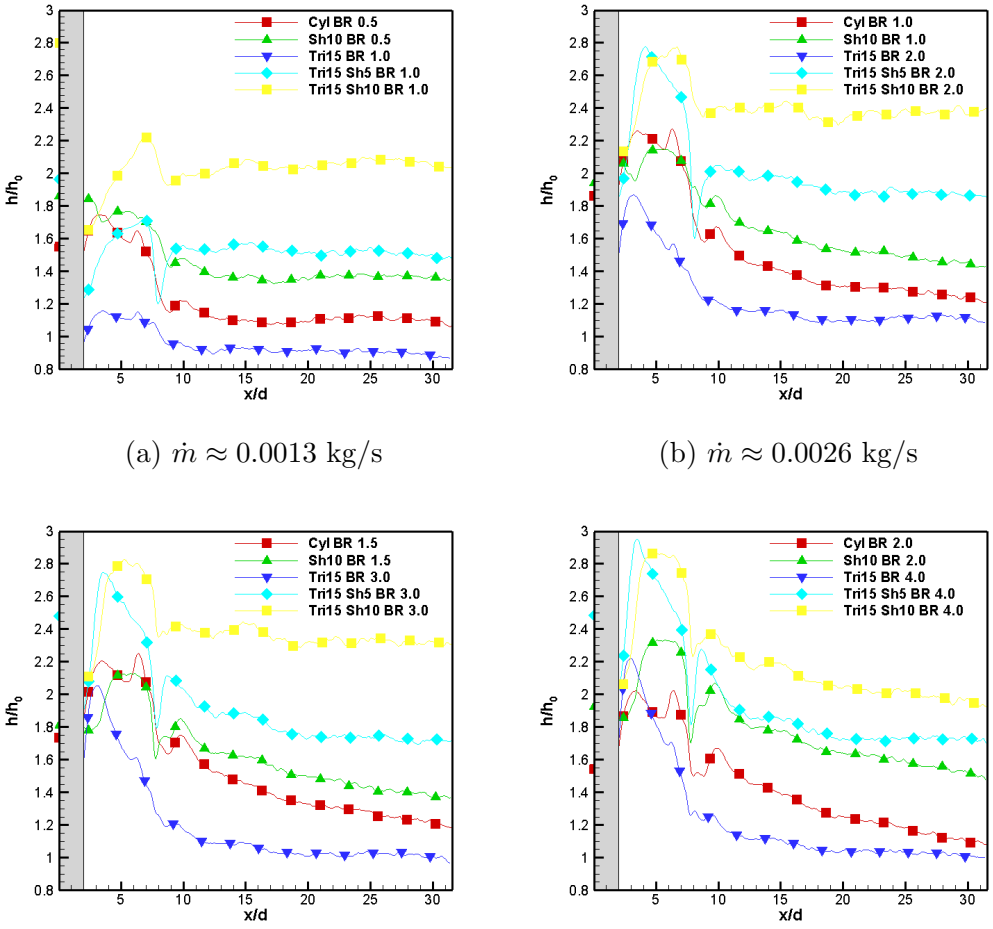

(a) $\dot{m} \approx 0.0013$ kg/s

(b) $\dot{m} \approx 0.0026$ kg/s

(c) $\dot{m} \approx 0.0039$ kg/s

(d) $\dot{m} \approx 0.0052$ kg/s

Figure 8.7: LATERALLY AVERAGED HEAT TRANSFER COEFFICIENT AT EQUAL MASS FLOW

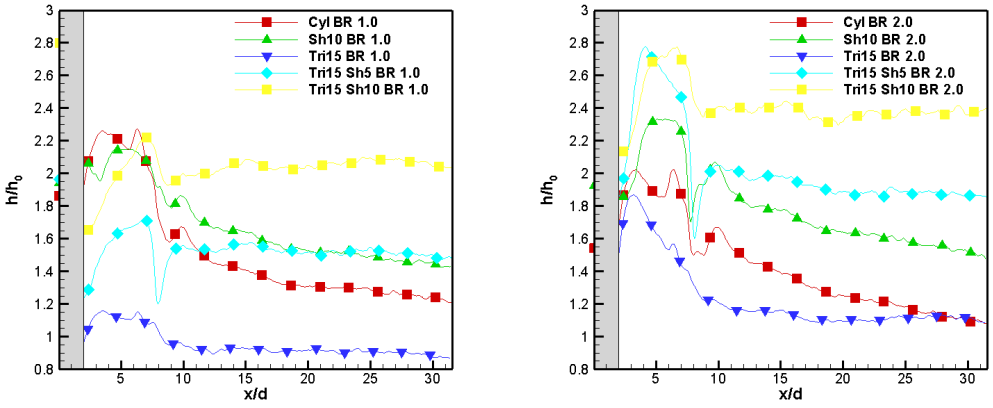

(a) BR=1.0 (b) BR=2.0

Figure 8.8: LATERALLY AVERAGED HEAT TRANSFER COEFFICIENT AT EQUAL BR

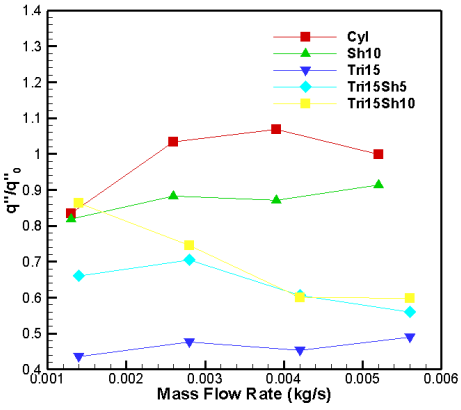

Figure 8.9: HEAT FLUX RATIO

9. Internal Cooling Experiments

The internal cooling experiments are the first work that I completed, and served as my introduction to gas turbing blade cooling. Internal cooling is widely used in the turbine section of an engine, both in the rotating blades and stationary vanes. Internal cooling has the advantage of not impacting the aerodynamics of the blades and vanes, as well as not mixing cooler air into the mainstream and reducing the power output of the engine. The internal passages are often serpentine in nature, having radially outward and radially inward sections. To improve the heat transfer of the passage, there may also be turbulators such as ribs or dimples. This research focuses on the effect of different rib configurations on the heat transfer of the internal walls of a three pass serpentine channel and a leading edge channel. These tests were conducted on the three pass test rig previously described, using the transient liquid crystal thermography technique with heated mainstream flow. Results are presented in the form of Nusselt number.

9.1 Test Section

The test geometry for this study is derived from the mid-span section of an actual cooled turbine first stage rotor blade. Figure 9.1a shows the cross-section of the blade. The given channel geometry includes one leading edge channel with its own coolant feed from the base of the channel and a three pass channel where the flow enters the channel adjacent to the leading edge channel and passes through two 180° turns before being ejected through a row of holes at the trailing edge. The leading edge channel coolant is ejected through two rows of showerhead film holes at the leading edge of the airfoil. Figure 9.1b shows the simplified geometry obtained by adding sharp corners to the channels to provide ease of fabrication

and testing. The leading edge and trailing edge channels were approximated by triangular channels. A rectangular channel approximates the first pass channel of the triple pass and a trapezoidal channel approximates the second pass. The channel dimensions are shown in Table 9.1. The hydraulic diameters are also shown for each channel. The inlet channel Reynolds number is fixed to the specified design condition. The channel length is extruded for the same channel size simulating a 2-dimensional channel with a length of 12 cm.

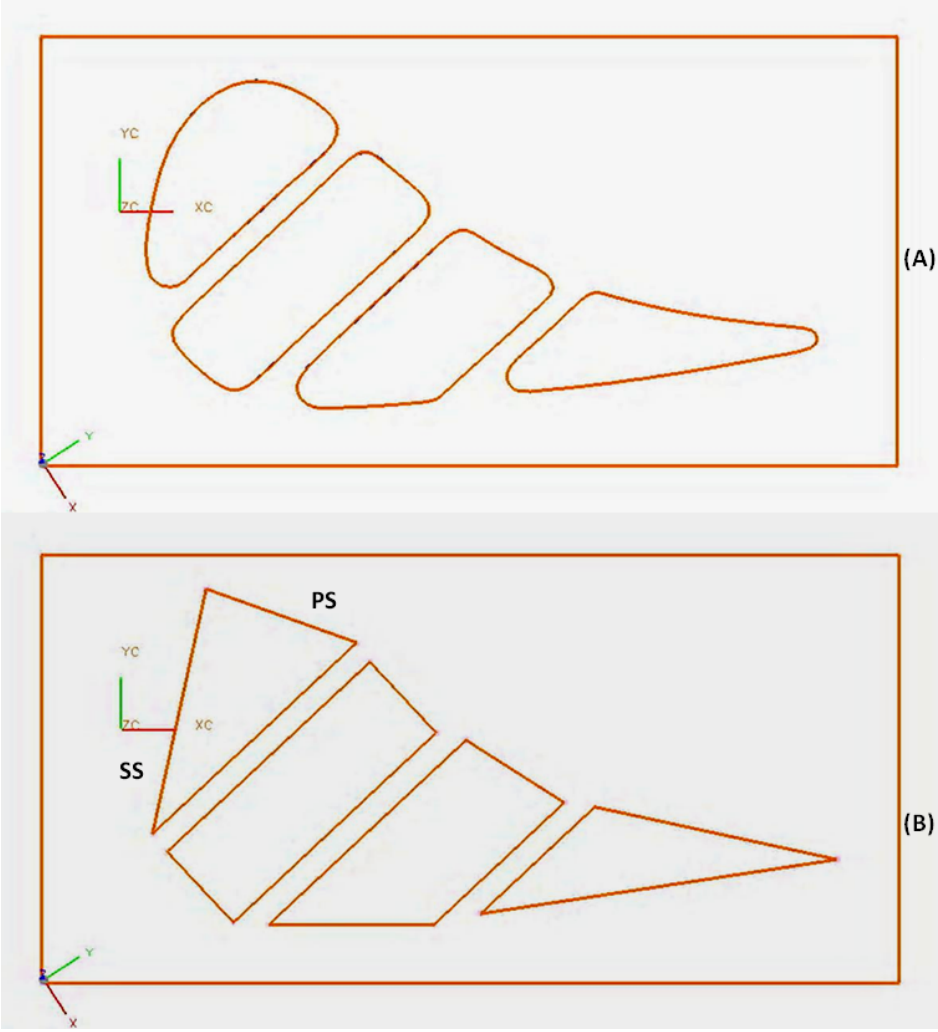

Figure 9.1: TEST SECTION GEOMETRY

Figure 9.2a shows the leading edge channel geometry with indicated flow paths and also the leading edge rows of holes and one dust hole. The flow enters at the hub of the channel and

Table 9.1: LIST OF TEST CONFIGURATIONS

Case	Channel	Geometry	Rib Configuration	P/e	e/D_h	Channel Dimensions (mm)
1	LE Channel	Triangular	Smooth	0	0	3.5289, 3.3163, 2.035
2	LE Channel	Triangular	(A)	8.8	0.082	3.5289, 3.3163, 2.035
3	First Pass	Rectangular	Smooth	0	0	3.502, 1.203, 3.502, 1.203
4	First Pass	Rectangular	(B) & (D)	8.8	0.066	3.502, 1.203, 3.502, 1.203
5	First Pass	Rectangular	(C) & (D)	8.8	0.066	3.502, 1.203, 3.502, 1.203
6	First Pass	Rectangular	(C)	8.8	0.066	3.502, 1.203, 3.502, 1.203
7	Second Pass	Trapezoidal	Smooth	0	0	1.469, 3.404, 2.081, 2.25
8	Second Pass	Trapezoidal	(B) & (D)	8.8	0.066	1.469, 3.404, 2.081, 2.25
9	Second Pass	Trapezoidal	(C) & (D)	8.8	0.066	1.469, 3.404, 2.081, 2.25
10	Second Pass	Trapezoidal	(C)	8.8	0.066	1.469, 3.404, 2.081, 2.25
11	Third Pass	Triangular	Smooth	0	0	3.125, 1.971, 4.545
12	Third Pass	Triangular	(B) & (D)	8.8	0.066	3.125, 1.971, 4.545
13	Third Pass	Triangular	(C) & (D)	8.8	0.066	3.125, 1.971, 4.545
14	Third Pass	Triangular	(C)	8.8	0.066	3.125, 1.971, 4.545

ejects out through the film holes and dust hole at the tip. Figure 9.2b shows the two views of the triple pass channel geometry. The top figure shows the pressure side view and the bottom figure shows the suction side view of the three pass channel. The flow enters the first pass at the hub and flow towards the tip. Some coolant is ejected through a dust hole at the tip. The flow then turns 180° into the second pass and travel from tip to hub and then turns 180° into the third pass flowing from hub to tip. Most of the coolant is ejected through a row of holes on the trailing edge and some coolant is ejected through two dust holes at the tip. Dust holes are typically provided to clean out the dust that might collect at 180° bends. Usually, a small amount of flow is ejected out of the dust hole.

Figure 9.3 shows the rib configurations for each wall. For the leading channel, the rib configuration was rib angles at 70° to the incoming flow and is shown in (A) configuration. The rib pitch and height are given in Table 1. For the triple pass, two rib configurations (B) and (C) are studied for the pressure side and suction side surfaces. The configuration

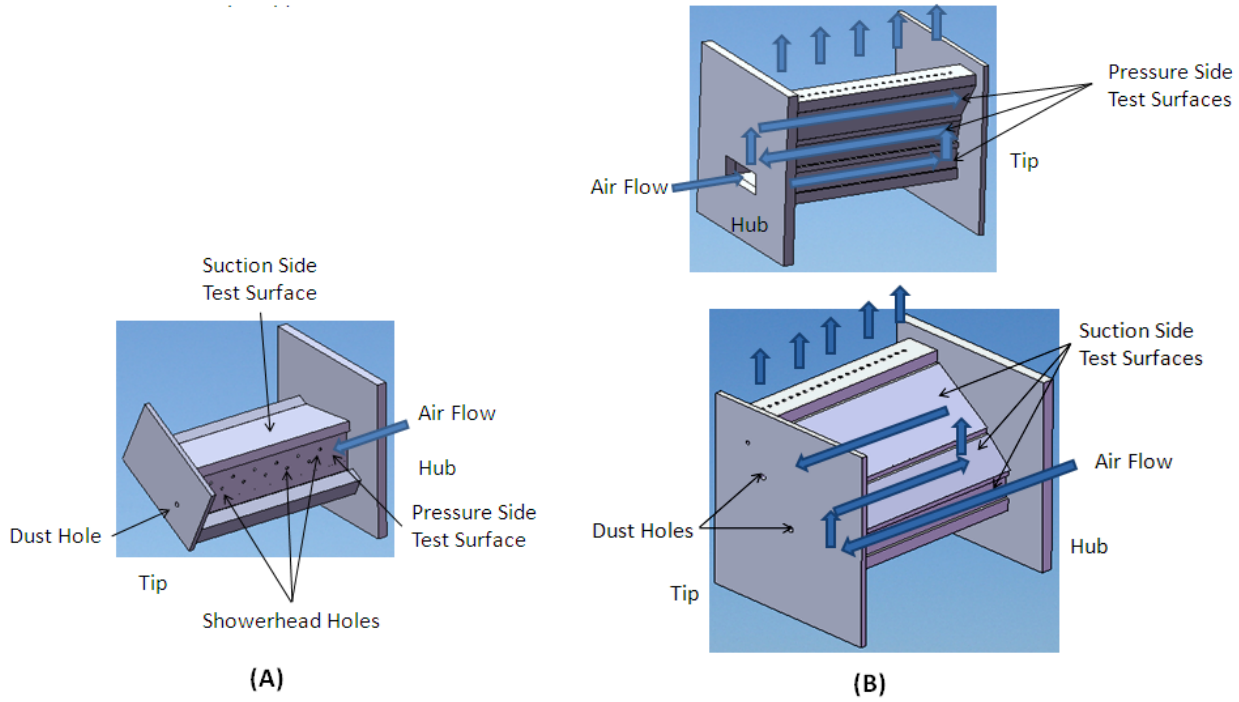

Figure 9.2: TEST FIXTURE GEOMETRY

(D) with the split 90° ribs is only for the divider walls. For the leading edge channel, only smooth and one ribbed configuration (A) are studied. For the triple pass channel, smooth, Configuration (B) and (D) together, Configuration (C) by itself, and Configuration (C) and (D) together are studied. All these configurations are listed in Table 9.1. The divider wall thickness is 3.18 mm. The heated flow is on both sides of the divider walls ensuring no heat loss through the divider walls.

Table 9.1 presents all the test cases that were run on the overall test geometry. Details on the various rib configurations including angle, rib pitch to height ratio (P/e) and the rib height to channel hydraulic diameter ratio (e/D_h). The channel dimensions are also presented for each of the four channels. The rib pitch to height is similar for all channels at 8.8. The rib height to channel hydraulic diameter is 0.082 for the leading edge channel and 0.066 for the triple pass channel. Also, it is important to note that the ribs used in the current study

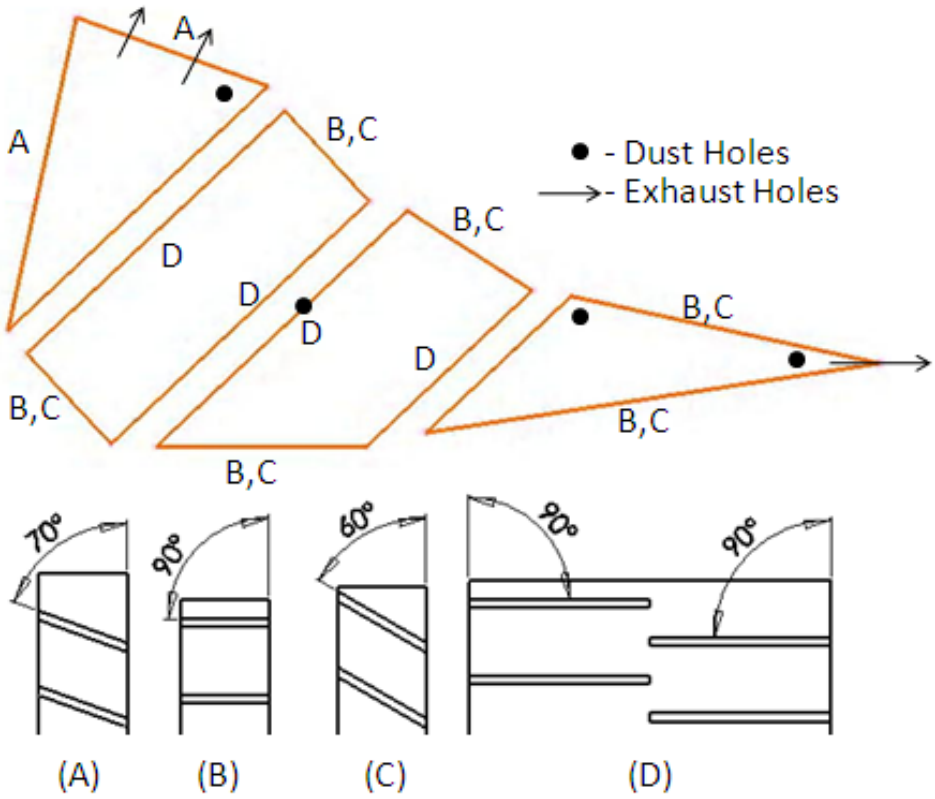

Figure 9.3: RIB ARRANGEMENTS STUDIED

are rounded edges similar to engine geometry whereas the correlations for designers were developed from measurements on square edged ribs.

9.2 Results and Discussions

9.2.1 Detailed Heat Transfer Distributions

Detailed heat transfer distributions were measured for a nominal channel entrance Reynolds number of 11,000 for the leading edge channel and a channel entrance Reynolds number of 25,500 for the triple pass with different rib channel configurations. Leading channel experiments were run independently as the leading edge channel and the triple pass do not

share the same entrance plenum.

Figure 9.4 presents detailed heat transfer (Nusselt number) distributions for different surfaces of the internal cooling channels for a leading channel with Configuration (A) ribs and a triple pass channel with Configuration (C) ribs and Configuration (D) ribs on the divider walls. The divider walls were not considered for the heat transfer measurement due to logistical difficulties. The arrows next to each contour plot show the direction of the flow with hub and tip markings for each end of the channel length. The leading edge triangular channel shows much higher heat transfer coefficients on the pressure side of the channel where the coolant ejection holes compared to the suction side surface. This is expected as the coolant will migrate towards the film holes thus reducing the coolant near the suction side wall. The hole locations are clearly seen with small circles in the channel middle. Also, the heat transfer is higher around the holes due to acceleration of the coolant towards the ejection hole. This has been observed by Ekkad et al. [36] in their study of ejection holes in between ribbed surfaces.

From the triple pass results, we can see that the secondary flows are clearly induced by the rib angles on all surfaces. The inlet flow into the first pass clearly produces significantly higher Nusselt numbers due to inlet effects. As the flow moves upward from the hub to the tip of first pass, Nusselt numbers decrease along the surface. Near the tip, the flow turns 180° from a rectangular channel into a trapezoidal channel. Again, Nusselt numbers are significantly higher as the flow negotiates the turn and expands into the second pass. The Nusselt numbers decreases as the flow moves from tip to hub for this pass. Interestingly, pressure side Nusselt numbers do not significantly decreases as seen for the suction side. In the third pass, the flow turns 180° into a narrow triangular channel with hole exits at one of the vertices (which is the trailing edge). The coolant negotiates the turn and immediately moves towards the trailing edge ejection holes resulting in high Nusselt numbers along the

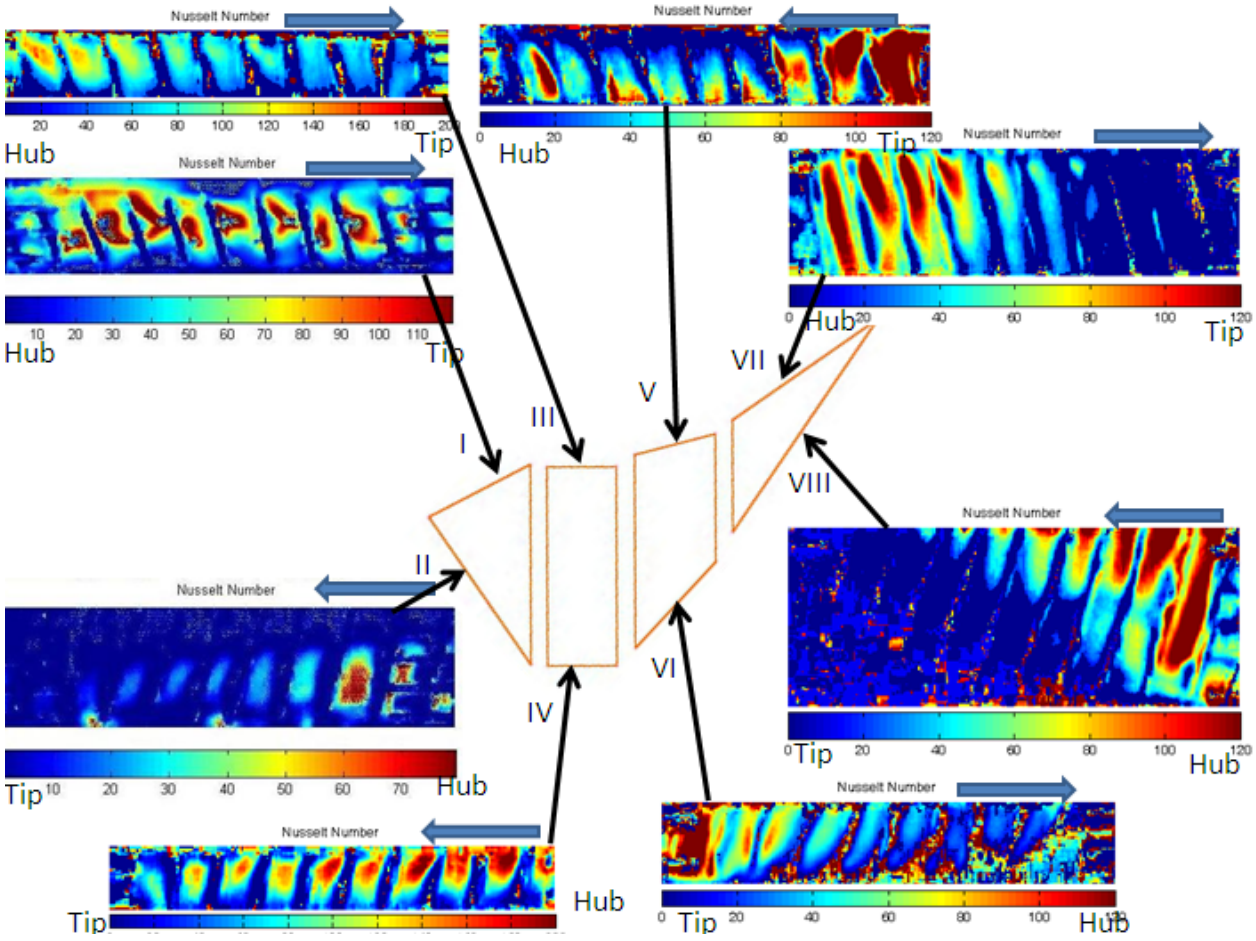

Figure 9.4: DETAILED HEAT TRANSFER (NU) DISTRIBUTIONS FOR ALL CHANNELS WITH CONFIGURATION (C)

hub region of the pass and very little heat transfer enhancement at the tip region due to depleted coolant mass.

9.2.2 Spanwise Averaged Nusselt Numbers

Figure 9.5 presents the spanwise averaged Nusselt numbers for the leading edge channel for both pressure and suction surfaces. The Nusselt numbers are compared for a smooth channel versus a ribbed channel with Configuration (A) (Case 1 Vs. Case 2). The top figure shows the pressure side Nusselt numbers and the bottom figure shows the suction side Nusselt numbers

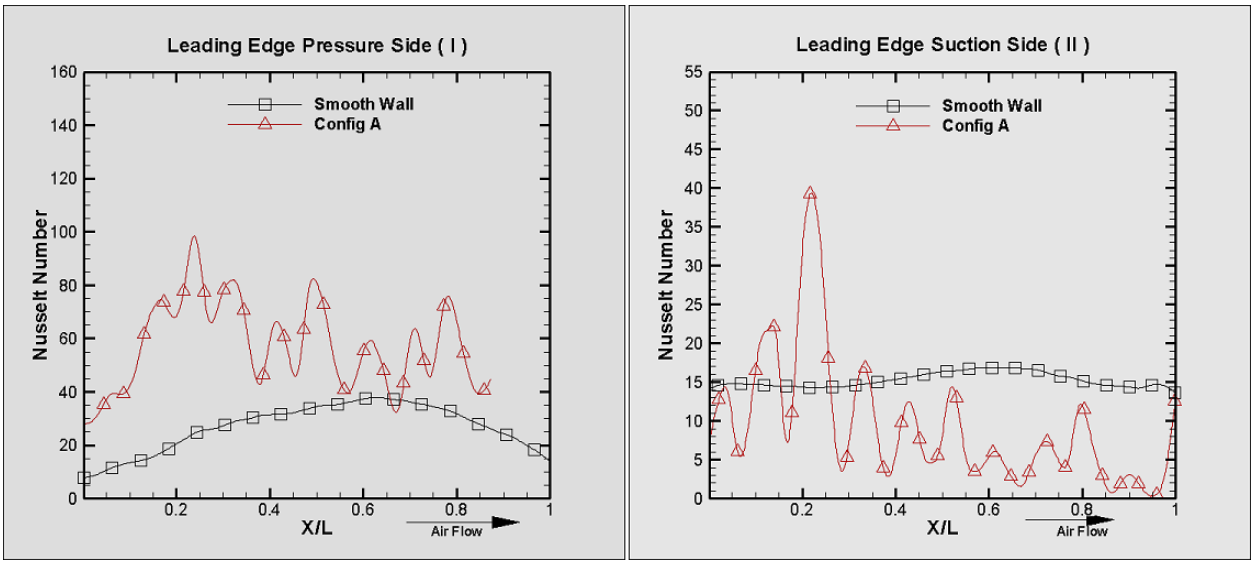

Figure 9.5: SPANWISE AVERAGED NUSSELT NUMBER FOR THE LEADING EDGE CHANNEL

as the flow enters from the hub. The axial distance is normalized by channel length. The pressure side surface shows significant enhancement over the smooth surface with almost 4 times enhancement at the entrance and about 1.5 times in the middle of the channel. It is to be noted that the flow is exiting through the holes on the leading edge and thus reducing the local Reynolds numbers in the channel. The coolant flow distribution for the smooth and ribbed walls may also be different along the passage as the presence of ribs can cause significant change in flow structure along the wall. On the suction surface, there is a degradation in heat transfer for the ribbed channel compared to the smooth channel. There is some enhancement in the near entrance region due to entrance effects and rib blockage. Once the flow enters the channel, the coolant migrates towards the pressure side wall as the film holes are along the pressure surface. This results in significant reduction in coolant flow along the suction surface. It is difficult to comprehend why the suction surface ribbed surface shows lower Nusselt numbers than the smooth surface. The only possible explanation for this is that more coolant migration occurs in the ribbed channel than for the smooth surface.

The detailed results clearly show the complex behavior of the coolant flow and the associated heat transfer distributions. The simplified channels geometries that are used in correlations cannot accurately predict the local behavior of the coolant and the Nusselt number distributions. However, the correlations can provide an overall average value which may be similar to averaged results from local measured heat transfer as seen in this study. However, the local cooling effectiveness may help determine failure locations and indicate lack of cooling in certain regions and may need to be addressed in design modifications.

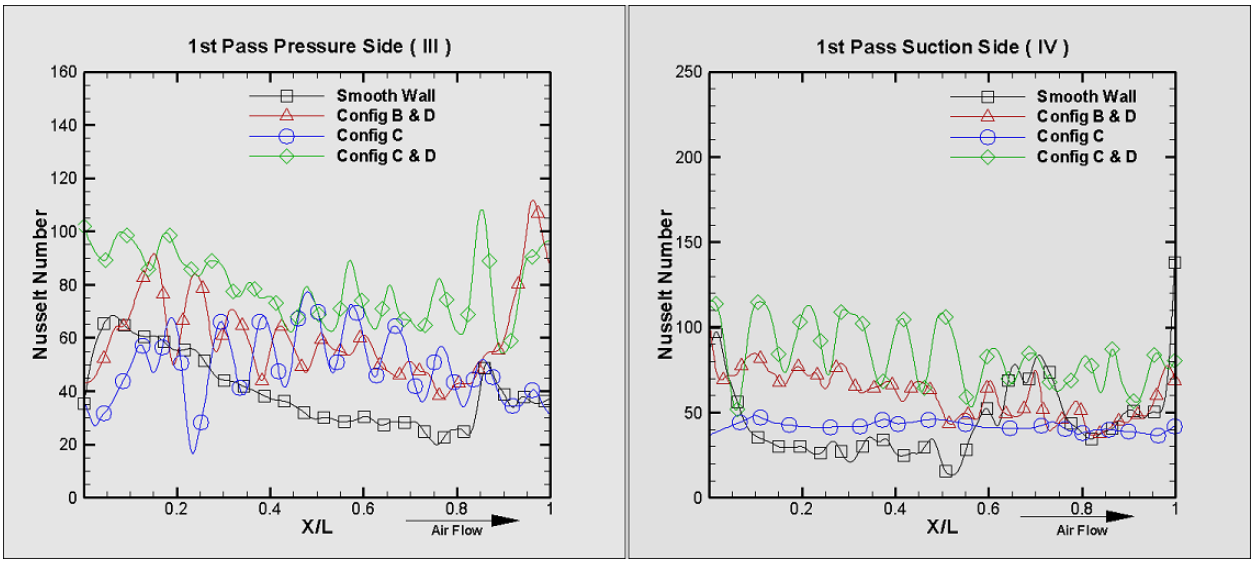

Figure 9.6: SPANWISE AVERAGED NUSSELT NUMBER FOR THE FIRST PASS OF THE SERPENTINE CHANNEL

Figure 9.6 presents the spanwise averaged Nusselt numbers for the first pass of the triple pass channel. Both pressure side and suction side surface Nusselt numbers are compared for cases 3-6 at channel inlet Reynolds number of 25,500. The pressure side surface with the angled rib and ribs on the divider wall (Conf. C) show the highest Nusselt number over the entire length of the channel. As expected, the smooth channel shows higher heat transfer at the entrance and decreases with increasing length and increases as the flow approaches the turn region at the end of the pass. The suction side surface also shows that Configuration

(C+D) is the highest with Configuration (B+D) being slightly lower. Interestingly, when the ribs are not placed on the divider wall as in Configuration (C) only, the suction surface shows very low Nusselt numbers. The suction smooth surface behaves similar to the pressure smooth surface but has lower overall Nusselt numbers.

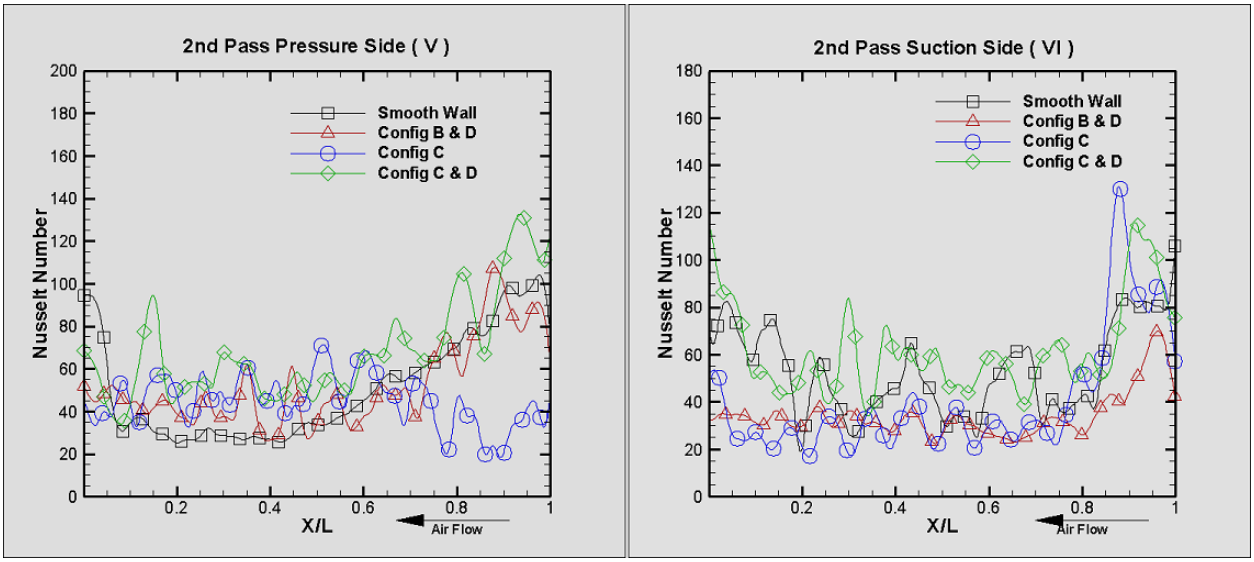

Figure 9.7: SPANWISE AVERAGED NUSSELT NUMBER FOR THE SECOND PASS OF THE SERPENTINE CHANNEL

Figure 9.7 presents the spanwise averaged Nusselt numbers for the second pass of the triple pass channel comparing cases 7-10. In this case, the flow direction is reversed with entrance at X/L=1. Significant enhancement is seen immediately after the 180° turn into the second pass. For the pressure side, all the four cases show similar levels of Nusselt number with the surface with angled ribs but no ribs on divider walls showing slightly lower values at the entrance region. Figure 9.7 also shows that the suction side heat transfer is significantly higher for the angled ribs with ribbed divider walls as in the case of the first pass pressure side. This may be because the flow is radially inward in this passage and may reflect similar behavior as the radially outward pressure side. The Configuration (B+D) ribbed channel shows lower Nusselt numbers than the other rib configurations.

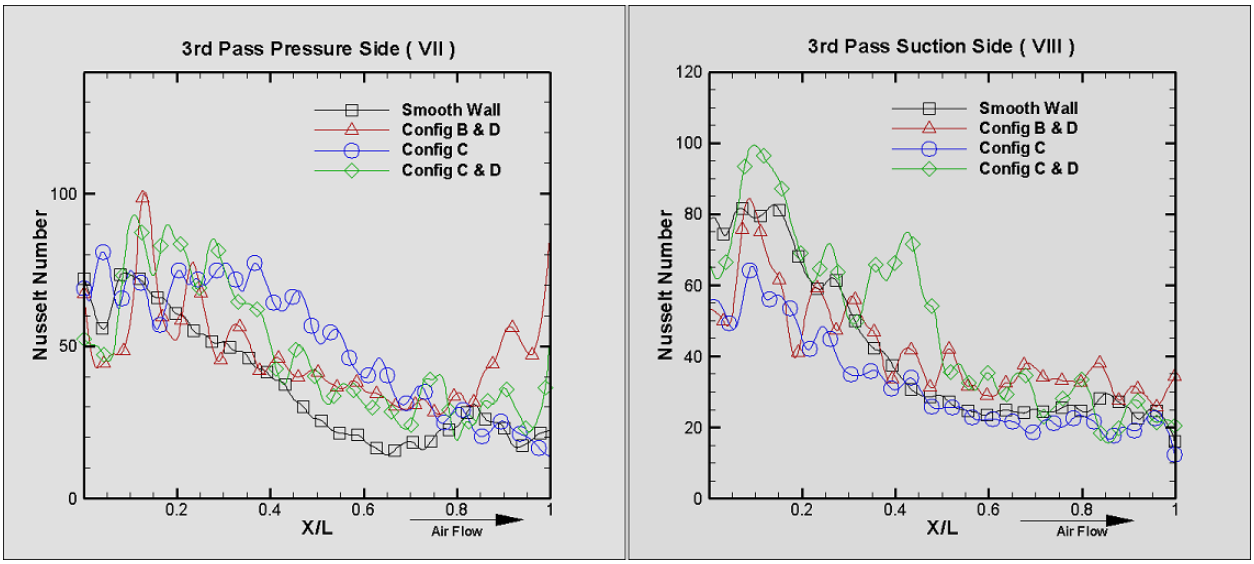

Figure 9.8: SPANWISE AVERAGED NUSSELT NUMBER FOR THE THIRD PASS OF THE SERPENTINE CHANNEL

Figure 9.8 presents the spanwise averaged Nusselt numbers for the third pass or trailing edge channel for cases 11-14. This is basically a very high aspect ratio triangular channel with exits at one of the corners which is the trailing edge of the blade. For the pressure side, the rib configuration (C) shows slightly higher Nusselt numbers in the middle of the channel. The Nusselt numbers are all high at the entrance of the pass right after the 180° turn and then decreasing as the flow laterally leaves the channel. The smooth channel shows the lowest Nusselt numbers. For the suction surface, all the four geometries show similar levels with the smooth wall being slightly higher than the Configuration (C) only. In this case, the ribs direct the flow from the hub towards the trailing edge ejection holes causing lower heat transfer regions near the tip of the channel. Figure 9.4 shows the 2-D distributions for this geometry.

Table 9.2: COMPARISON OF NUSSELT NUMBERS FROM EXPERIMENTAL DATA TO CORRELATION PREDICTIONS

	Smooth	90° Ribs	60° Ribs
First Pass (Experiment)	42.5	60.64	82
First Pass (Correlations)	69	92	125
Difference (Corr/Exp)	1.62	1.52	1.52

9.2.3 Comparisons with Correlations

Nusselt numbers and pressure drop were computed using correlations provided by Han [26] for rectangular ribbed channels. The smooth channel Nusselt number was computed using the Dittus-Boelter correlation for smooth round pipe. Table 9.2 provides the comparison for first pass of the triple pass channel as it is rectangular. There is no correlation available for a trapezoidal channel or a triangular channel. Results are only compared for the first pass rectangular channel. Since the correlations use fully developed flow conditions, the experiment does not produce ideal conditions. Directly applying the correlation to the experimental rib configuration and channel geometry produces much higher predicted Nusselt numbers for the channel. There is a 50–60% lower measured Nusselt number than the predicted value. There are many reasons:

1. Flow is not fully developed in the experiment because entrance length is small
2. Ribs are rounded compared to sharp edged in the correlation causing lower enhancement
3. Flow is not expanded uniformly due to sudden expansion to simulate engine type entrance conditions
4. Exit conditions are different as the flow turns into the second pass in the experiment

9.2.4 Pressure Drop Results

The test section was instrumented with static pressure taps at the entrance of first pass, in the turn region between first pass and second pass and the turn region between the second pass and third pass. Pressure was also measured at the inlet of the leading edge channel. Results show the total pressure is lowest for the smooth channel with 90° ribbed channel showing the highest overall pressure drop. Table 9.3 provides the overall area averaged Nusselt numbers for each surface of the triple pass and the static pressure at the three measuring stations. Results show that the overall averaged heat transfer is lowest for the smooth surface and so is the overall pressure required to drive the flow through the smooth channels. Majority of the pressure drop occurs across the third pass for all the geometries with a value of around 4.5 kPa. Results show the heat transfer enhancement for the channels with angled ribs and divider wall ribs is significant with only a minor rise in overall pressure drop.

Table 9.3: OVERALL NUSSELT NUMBERS AND GAGE PRESSURE ACROSS THE TRIPLE PASS CHANNEL

Measured Average Nusselt Number				
Configuration	Smooth Wall	B+D	C	C+D
1st Pass Pressure Side	41.15	60.64	50.52	79.7
1st Pass Suction Side	44.21	60.65	42.47	83.37
2nd Pass Pressure Side	51.45	53.25	56.2	68.54
2nd Pass Suction Side	58.79	34.24	40.4	61.88
3rd Pass Pressure Side	37.16	46.94	40	48.84
3rd Pass Suction Side	41.69	52.09	35	48.96
Pressure Data (kPa)				
Configuration	Smooth Wall	B+D	C	C+D
1st Pass Entrance	4.995	5.342	5.1	5.205
1st Turn Region	4.8575	5.0125	4.93	5.0425
2nd Turn Region	4.46	4.5075	4.48	4.5

9.3 Conclusions

Detailed heat transfer distributions are presented for a realistic turbine blade cooling circuit at engine representative Reynolds numbers. Different rib configurations have been studied to determine the effect on heat transfer and pressure drop. The results show 50–100% enhancement in heat transfer compared to smooth surface. The detailed distributions clearly show the effect of coolant migration in these more complicated shaped channels with ribs and film cooling ejection holes. Entrance conditions are not smoothed and are similar to realistic channels resulting in strong entrance effects on channel heat transfer. The results from the current study were compared with correlation based predictions for the first pass rectangular channel for ribs and smooth surfaces. The correlation over-predicts the Nusselt number compared to the experimentally obtained Nusselt numbers. These results provide insight into using correlations developed for simplified geometries and idealistic flow conditions to predicting heat transfer for more realistic geometries. There is a need for more detailed studies on comparing predicted heat transfer results from correlations and actual measurements on realistic channels. With the current technique, it may also be easier to evaluate complete blade circuits for actual Nusselt numbers and operating conditions. These numbers can then be scaled up to engine conditions and used in design analysis.

10. Research Conclusions

This dissertation follows the evolution of the tripod hole concept, from the simplest design of three holes of equal diameter that diverge from a common entrance at a 15° breakout angle through the addition of shaped exits to the tripod hole concept, with several design alterations in between. The initial flat plate testing demonstrated a significant performance increase with the tripod holes with 15° breakout angle when compared to baseline cylindrical and modern shaped holes. The testing on the vane cascade showed that the tripod design is a moderate improvement on the pressure side of the blade, and a significant improvement on the suction side. The improvement on the suction side is attributed both to the spreading of the jets providing better coverage in between the ejection holes, as well as the spreading of the jets reducing the streamwise momentum of the injected fluid and thus reducing the tendency of the jet to separate from the surface. Changing the breakout angle to 30° resulted in a design that uses even less coolant than the 15° breakout angle, but pays for this advantage in a reduction in film cooling effectiveness. The addition of shaping to the tripod design increases the film cooling effectiveness even further, with the 10° shaping providing a larger benefit than the 5° shaping. These modifications also result in a higher heat transfer coefficient than the other designs, which is offset by the reduction in the local air temperature above the surface. The overall heat flux ratio for the tripod designs is lower than for the cylindrical and shaped designs, with the unshaped tripod design having the lowest heat flux ratio of the tested designs. The addition of shaping to the tripod design shows clear advantages in film cooling effectiveness levels and evenness of coverage, preventing the formation of regions of low effectiveness between injection holes, which can be seen on the tripod design without shaping. For these reasons it is recommended that future experimentation include cases with shaping on the tripod holes, and that these designs be included in the stress analysis. Future experimentation should also include transient testing on the vane cascade rig, now that a

sufficiently powerful DC power supply is available.

The tripod designs show great promise in improving film cooling coverage while reducing the coolant used. Replacing a single row of cylindrical or shaped injection holes with tripod holes results in an effectiveness improvement of ≈40% while reducing the coolant used by ≈50%, at the cost of having to drill 50% more holes. The film coverage from the tripod holes is strong enough to allow the possibility of replacing a double row of staggered holes with a single row of tripod holes, which would result in similar levels of cooling while reducing coolant usage ≈75% and reducing the number of holes to be drilled by 25%. The tripod design is also of interest in the suction side throat region, where the improved downstream coverage can help protect the trailing edge of the blade more than a traditional design. The final advantage of the tripod design is the relative insensitivity to blowing ratio, allowing for greater flexibility for turbine blade designers. This design has strong potential to improve the performance of gas turbine engines.

Nomenclature

BR	blowing ratio
D_h	hydraulic diameter
L	length of channel
Nu	Nusselt number
P	rib to rib spacing or pitch
R	gas constant
Re	Reynolds number
T	temperature, °C
V	velocity, m/s
d	hole diameter
h	heat transfer coefficient, W/m^2K
k	thermal conductivity
l	hole length
n	number of holes on the inlet side of the test plate
p	hole pitch
t	time, s
x	axial distance from hole leading edge
α	thermal diffusivity
η	adiabatic film-cooling effectiveness
ρ	fluid density

Subscripts

avg	average
c	coolant
f	film
g	engine gas
$main$	mainstream air with no secondary gas injection
mix	mixture of mainstream air and secondary gas
sg	secondary gas
w	wall
∞	mainstream air

Bibliography

[1] Goldstein, R. J., Eckert, E. R. G., and Burggraf, F., 1973. "Effects of Hole Geometry and Density on Three-Dimensional Film Cooling". *Int. J. Heat Mass Transfer,* ***17***, pp. 595–607.

[2] Pederson, D. R., Eckert, E. R. G., and Goldstein, R. J., 1977. "Film Cooling with Large Density Differences Between Mainstream and the Secondary Fluid Measured by the Heat–Mass Transfer Analogy". *Int. J. Heat Mass Transfer,* ***99***, pp. 620–627.

[3] Sinha, A. K., Bogard, D. G., and Crawford, M. E., 1991. "Film–Cooling Effectiveness Downstream of a Single Row of Holes with Variable Density Ratio". *Journal of Turbomachinery,* ***113***, pp. 442–449.

[4] Ligrani, P. M., Wigle, J. M., Ciriello, S., and Jackson, S. W., 1994. "Film–Cooling from Holes with Compound Angle Orientation. Part I: Results Downstream of Two Staggered Row of Holes with 3D Spanwise Spacing". *Journal of Heat Transfer,* ***116***, pp. 341–352.

[5] Schmidt, D. L., Sen, B., and Bogard, D. G., 1994. "Film Cooling with Compound Angle Holes: Adiabatic Effectiveness". In Proceedings of IGTI Turbo Expo 1994, no. 94-GT-312.

[6] Leylek, J. H., and Zerkle, R. D., 1994. "Discrete–Jet Film Cooling: A Comparison of Computational Results with Experiments". *Journal of Turbomachinery,* ***116***, pp. 358–368.

[7] Haven, B. A., Yamagata, D. K., Kurosaka, M., Yamawaki, S., and Maya, T., 1997. "Anti-Kidney Pair of Vortices in Shaped Holes and Their Influence on Film Cooling Effectiveness". In Proceedings of ASME Turbo Expo 1997, no. 97-GT-45.

[8] Gritsch, M., Schulz, A., and Wittig, S., 1997. "Adiabatic Wall Effectiveness Measurements of Film–Cooling Holes with Expanded Exits". In Proceedings of IGTI Turbo Expo 1997, no. 97-GT-164.

[9] Bunker, R. S., 2005. "A Review of Shaped Hole Turbine Film–Cooling Technology". *Journal of Heat Transfer,* ***127***, pp. 441–453.

[10] Shih, T. I. P., Lin, Y. L., Chyu, M. K., and Gogineni, S., 1999. "Computations of Film Cooling from Holes with Struts". In Proceedings of IGTI Turbo Expo 1999, no. 99-GT-282.

[11] Papell, S. S., 1984. "Vortex Generating Flow Passage Design for Increased Film–Cooling Effectiveness and Surface Coverage". In Presented at the 22nd Natl. Heat Transfer Conf.

[12] Zaman, K. B. M. Q., and Foss, J. K., 1997. "The Effects of Vortex Generators on a Jet in Crossflow". *Physics of Fluids,* ***9***, pp. 106–114.

[13] Bunker, R. S., 2002. "Film Cooling Effectiveness Due to Discrete Holes within a Transverse Surface Slot". In Proceedings of IGTI Turbo Expo 2002, no. GT-2002-30178.

[14] Lu, Y., Faucheaux, D., and Ekkad, S. V., 2005. "Film Cooling Measurements for Novel Hole Configurations". In Proceedings of IGTI Turbo Expo 2005, no. HT200572396.

[15] Kusterer, K., Bohn, D., Sugimoto, T., and Tanaka, R., 2007. "Double–Jet Ejection of Cooling Air for Improved Film Cooling". *Journal of Turbomachinery*, April, pp. 809–815.

[16] Liu, J. S., Malak, M. F., Tapia, L. A., Crites, D. C., Ramachandran, D., Srinivasan, B., Muthiah, G., and Venkataramanan, J., 2010. "Enhanced Film Cooling Effectiveness with New Shaped Holes". In Proceedings of IGTI Turbo Expo 2010, no. GT-2010-22774.

[17] Baheri, S., Tabrizi, S. P. A., and Jubran, B. A., 2001. "Film Cooling Effectiveness from Trenched Shaped and Compound Holes". *International Journal of Heat and Mass Transfer,* ***44***(8), April, pp. 989–998.

[18] Zuniga, A., and Kapat, J., 2009. "Effect of Increasing Pitch-to-Diameter Ratio on the Film Cooling Effectiveness of Shaped and Cylindrical Holes Embedded in Trenches". In Proceedings of Turbo Expo 2009, no. GT2009-60080.

[19] Lu, Y., Dhungel, A., Ekkad, S. V., and Bunker, R. S., 2009. "Effect of Trench Width and Depth on Film Cooling from Cylindrical Holes Embedded in Trenches". *Journal of Turbomachinery,* ***131***(1), p. 011003.

[20] Drost, U., Bolcs, A., and Hoffs, A., 1997. "Utilization of the Transient Liquid Crystal Technique for Film Cooling Effectiveness and Heat Transfer Investigations on a Flat Plate and a Turbine Airfoil". In Proceedings of Turbo Expo 1997, no. IGTI026-1997.

[21] Ghorab, M. G., and Hassan, I. G., 2010. "An Experimental Investigation of a New Hybrid Film Cooling Scheme". *International Journal of Heat and Mass Transfer*, pp. 4994–5007.

[22] Liu, C., Zhu, H., Bai, J., and Xu, D., 2010. "Film Cooling Performance of Converging-slot Hole Rows on a Gas Turbine Blade". *International Journal of Heat and Mass Transfer*, pp. 5232–5241.

[23] Heidmann, J. D., and Ekkad, S. V., 2008. "A Novel Antivortex Turbine Film–Cooling Hole Concept". *Journal of Turbomachinery,* ***130***(3), July.

[24] Dhungel, S., Phillips, A., Ekkad, S. V., and Heidmann, J. D., 2009. "Experimental Investigation of a Novel Anti–Vortex Film Cooling Hole Design". *Journal of Turbomachinery,* ***131***, April.

[25] Han, J. C., 1984. "Heat Transfer and Friction in Channels with Two Opposite Rib-Roughened Walls". *ASME Journal of Heat Transfer,* ***106***, Nov., pp. 774–781.

[26] Han, J. C., 1988. "Heat Transfer and Friction Characteristics in Rectangular Channels with Rib Turbulators". *ASME Journal of Heat Transfer,* ***110***, May, pp. 321–328.

[27] Han, J. C., Zhang, Y. M., and Lee, C. P., 1991. "Augmented Heat Transfer in Square Channels with Parallel, Crossed, and V-Shaped Ribs". *ASME Journal of Heat Transfer,* ***113***, Oct., pp. 590–596.

[28] Zhang, Y. M., Gu, W. Z., and Han, J. C., 1994. "Augmented Heat Transfer in Triangular Ducts with Full and Partial Ribbed Walls". *AIAA Journal of Thermophysics and Heat Transfer,* ***8***, July, pp. 574–579.

[29] Taslim, M. E., Li, T., and Spring, S. D., 1997. "Measurements of Heat Transfer Coefficients and Friction Factors in Rib-Roughened Channels Simulating Leading Edge Cavities of a Modern Turbine Blade". *ASME Journal of Turbomachinery,* ***119***, Oct., pp. 601–609.

[30] Ekkad, S. V., and Han, J. C., 1997. "Detailed Heat Transfer Distributions in Two-Pass Square Channels with Rib Turbulators". *International Journal of Heat and Mass Transfer,* ***40***(11), pp. 2525–2537.

[31] Han, J. C., Dutta, S., and Ekkad, S. V., 2001. *Gas Turbine Heat Transfer and Cooling Technology.* Taylor & Francis, New York, New York.

[32] Poser, R., Von Wolfersdorf, J., Lutum, E., and Semmler, K., 2008. "Performing Heat Transfer Experiments in Blade Cooling Circuits Using a Transient Technique with Thermochromic Liquid Crystals". In Proceedings of ASME Turbo Expo 2008, no. GT2008-50364.

[33] Incropera, F. P., DeWitt, D. P., Bergman, T. L., and Lavine, A. S., 2007. *Fundamentals of Heat and Mass Transfer*, sixth ed. John Wiley & Sons, Inc., ch. 5.

[34] Bejan, A., 2004. *Convection Heat Transfer*, third ed. John Wiley & Sons, Inc., ch. 2,7.

[35] Coleman, H. W., and Steele, W. G., 1989. *Experimentation and Uncertainty Analysis for Engineers*. John Wiley & Sons, New York, ch. 3, 4.

[36] Ekkad, S. V., and Han, J. C., 2000. "A Transient Liquid Crystal Thermography Technique for Gas Turbine Heat Transfer Measurements". *Measurement Science & Technology, Special Edition on Gas Turbine Measurements,* ***11***, July, pp. 957–968.